

Adaptive two-scale models for processes with evolution of microstructures

Von der Fakultät für Mathematik und Physik der Universität Stuttgart
zur Erlangung der Würde eines Doktors der
Naturwissenschaften (Dr. rer. nat.) genehmigte Abhandlung

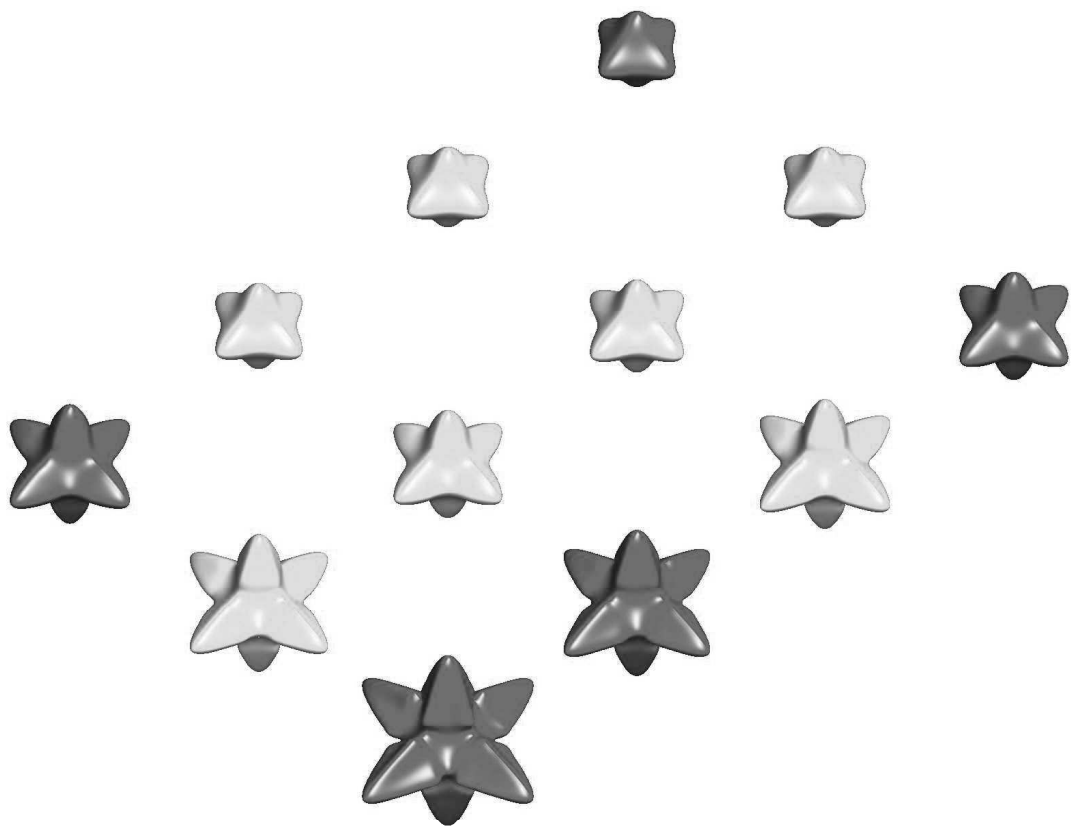
Vorgelegt von
Magnus Redeker
aus Herford

Hauptberichter:	Prof. Dr. Christian Rohde
Mitberichter:	Prof. Dr. I. Sorin Pop Prof. Dr. Kunibert G. Siebert
Tag der mündlichen Prüfung:	26. 06. 2014

Institut für Angewandte Analysis und Numerische Simulation der Universität Stuttgart

2014

D 93



Dendritic solids resulting from an adaptive numerical solution of a two-scale model for solidification. The corresponding temperature field increases monotonically from the lower left to the upper right. The adaptive algorithm computed only the solids highlighted in dark-gray. The remaining solids are interpolated between computed solids. More details are presented in Section 3.

Contents

Abstract & Zusammenfassung	7
1 Introduction	9
2 A two-scale phase-field model for solidification	15
2.1 The microscopic phase-field model	15
2.2 The two-scale phase-field model	18
2.3 Further analysis of the two-scale model's microscopic problem	21
3 A fast and accurate adaptive solution strategy for two-scale models with continuous inter-scale dependencies	27
3.1 Introduction	27
3.2 The considered two-scale model	28
3.3 The adaptive solution strategy	31
3.4 Numerical results	37
3.5 Conclusion and outlook	48
Acknowledgment	50
4 A POD-EIM reduced two-scale model for crystal growth	51
4.1 Introduction	51
4.2 The detailed two-scale model	52
4.3 The reduced two-scale model	55
4.4 Numerical results	60
4.5 Conclusion and outlook	72
Acknowledgment	72
5 Upscaling of a tri-phase phase-field model for precipitation in porous media	75
5.1 Introduction	75
5.2 The pore-scale model	76
5.3 Upscaling	95
5.4 Numerical results	100
5.5 Conclusion and outlook	108
Acknowledgment	108
6 Conclusion and outlook	109
Acknowledgment	111
References	113

Abstract

In this dissertation two combinable numerical solution schemes are developed that – either in combination or on their own – allow for an efficient numerical solution of two-scale models that describe physical processes with changing microstructures via the combination of partial differential equations on a macro- and a microscopic length-scale.

Furthermore, a two-scale phase-field model is established, that describes in a porous medium a pore-scale precipitation and a Darcy-scale diffusion process of in a fluid dissolved particles. One of the developed solution schemes is used in order to solve this model efficiently in a large time-space-cylinder. Numerical results show the interdependence of the pore-scale precipitation and the Darcy-scale diffusion process.

Zusammenfassung

In dieser Dissertation werden zwei effiziente numerische Lösungsverfahren für zweiskalige Modelle entwickelt. Durch die Kombination von partiellen Differentialgleichungen auf einer makro- und einer mikroskopischen Längenskala beschreiben die dabei betrachteten Modelle physikalische Prozesse bei denen die sich Mikrostruktur im Laufe der Zeit ändert. Da die beiden Verfahren konsistent zueinander sind, garantiert ihre Kombination eine weitere Effizienzsteigerung.

Des Weiteren wird ein zweiskaliges Phasenfeldmodell entwickelt, welches in einem porösen Medium auf der Mikroskala einen Ablagerungsprozess von in einem Fluid gelösten Partikeln und auf der Darcyskala deren Diffusion beschreibt. Zur effizienten numerischen Lösung in einem großen Raum-Zeit-Zylinder wird eines der beiden entwickelten Verfahren verwendet. Numerische Resultate belegen die gegenseitige Abhängigkeit des Ablagerungs- und des Diffusionsprozesses der gelösten Partikel.

1 Introduction

Many technically relevant processes exhibit a priori unknown microstructures that evolve in time. Important examples are solidification processes with dendritic or eutectic microstructures [16, 43], flow in porous media with changing pore geometry as a consequence of elastoplastic deformations and deposition or desorption of matter, and microstructures in epitaxial growth of thin solid layers [24]. Due to huge differences in relevant length and possibly also time scales, it is usually not feasible to simulate such processes by a direct numerical discretization of a full model. A much more promising approach is the usage of homogenization or averaging techniques, that were originally developed with the aim to find purely macroscopic models with suitable constitutive laws that model the properties of the microstructure [15, 32, 34]. The application of those methods to processes with evolution of a priori unknown microstructures typically leads to full two- or multi-scale models that combine differential equations on the smallest scales with homogenized differential equations on the macroscopic scales [19]. Both scales are coupled: the macroscopic fields influence the evolution of the microstructures, and the microscopic fields enter to the homogenized equations via averaged coefficients. A direct discretization of such a two-scale model requires, besides the solution of the macroscopic problem, typically the solution of a full microscopic cell problem for every node of a macroscopic numerical grid. This leads to a huge numerical complexity and limits the application to problems with comparatively small macroscopic grids.

In this thesis two efficient numerical solution schemes for two-scale models are developed. As mentioned before, it is the sheer number of the microscopic problems that makes a direct numerical solution of the two-scale model demanding. Therefore, in order to accelerate the computation, both developed schemes accelerate the solution of the microscopic problems. The first one minimizes adaptively the number of the microscopic problems that are solved. On contrary, the second one minimizes their complexity. Consequently, the two schemes are consistent with one another. Numerical results for a sample two-scale model show the efficiency of both solution schemes. Both schemes accelerate the solution significantly and, in addition, they largely preserve the accuracy of a direct discretization. Since they are consistent with one another, it is perfectly possible to combine them in order to gain a further increase of efficiency.

The considered sample two-scale model describes a solidification process in a binary mixture with strong heat and weak solute diffusion. The model consists of a macroscopic homogenized heat equation for the macroscopic temperature and for each point of the macroscopic grid of a microscopic problem. The microscopic problems describe the evolution of the microscopic concentration of one part of the mixture as well as the evolution of the microscopic phase-field that describes the solidification process. Unlike sharp-interface models, phase-field models do not distinguish sharply between the two phases liquid and solid. In fact the phase-field varies smoothly from its liquid to its solid value within a small phase transition region. A brief introduction into phase-field modeling and the method of homogenization is presented in Section 2. The evolution of the temperature in a macroscopic node influences continuously the solidification process in the microscopic problem of the same macroscopic node: the smaller the temperature the faster the increase of the solid. Vice versa, the latent heat that is released during solidification in the microscopic problem in a macroscopic node influences continuously the evolution of the temperature

in the same macroscopic node: the more latent heat is released the higher the increase of the temperature.

The adaptive solution strategy established in Section 3 – the first of the two in this thesis developed solution schemes – is applicable to every two-scale model on condition that the variables on the different scales depend continuously on each other. Exploiting this condition, the key to an efficient solution is the reuse of already computed microscopic solutions as approximation to the solutions of other microscopic problems. Provided that two microscopic problems are influenced by similar macroscopic fields, the solution of the one problem is, due to the solutions' continuous dependence on the influencing macroscopic fields, a good approximation to the solution of the other problem.

Fundamental to this strategy is the distinction between similar and unsimilar macroscopic fields. Considering the sample problem, a metric is developed that measures the distance of temperature evolutions. By definition, two temperature evolutions are similar provided that their distance is not larger than a certain tolerance. The scheme subdivides the set of macroscopic nodes into active and inactive nodes. Whereas the microscopic problems in active macroscopic nodes are solved, the microscopic data in inactive nodes is not computed but approximated by the microscopic data of active nodes with similar temperature evolutions. The set of active macroscopic nodes is updated adaptively: it is coarsened if possible and refined if necessary. Initially only one macroscopic node is active. Inactive nodes are added successively to the set until to every inactive node at least one active node exists with a similar temperature evolution. On contrary, active nodes are removed successively from the set until the temperature evolutions of all active nodes are unsimilar.

The adaptive update of the set of active nodes assures an efficient numerical solution of the two-scale model. The coarsening accelerates the solution. Due to refinement the solution maintains its level of accuracy in comparison to a direct discretization. The smaller the tolerance the higher the accuracy and the more nodes are active. Numerical results indeed show that, in comparison to a direct discretization, the adaptive strategy is very efficient. It enables to accelerate the solution tremendously and at the same time to largely maintain the accuracy.

A reduction of the number of the microscopic problems that are solved yields a reduction of the required memory resources. This is of importance especially in three space dimensions. Section 3 presents an adaptive solution to a discrete two-scale problem in three space dimensions. The macroscopic numerical grid consists of 24,000 nodes. Furthermore, the microscopic grid consists of 216,000,000 nodes. Without regard to the fact that to solve in each step of time 24,000 microscopic problems each with 216,000,000 degrees of freedom takes what feels like an eternity, in order to store the 24,000 solutions gigantic memory capacities are required. Therefore, this problem is in principle not solvable by a direct discretization. However, the adaptive strategy allows to solve it.

Whereas the adaptive strategy reduces the number of the microscopic problems that are solved in course of a simulation, the second in Section 4 developed solution scheme reduces the complexity of the microscopic problems. The sample two-scale model poses several challenges for model reduction: parameter dependency via the macroscopic temperature, high dimensionality, the coupling of the concentration and the phase-field, time-dependency and non-linearities in the partial differential equations describing the evolution of the concentration and the phase-field.

These challenges are addressed by a combination of the following approaches. Firstly, the high dimensionality of the microscopic model is addressed by a Proper Orthogonal Decomposition (POD) strategy [35, 58], i.e. a snapshot-based generation of a low-dimensional approximation space and projection of the detailed microscopic model to this subspace. Different POD spaces for the different field variables are generated resulting in coupled reduced models. Secondly, the non-linearity and the parameter-dependency are addressed by the Empirical Interpolation Method [2], which enables to efficiently evaluate local parametric discretization operators as in [14, 18]. Thirdly, the high solution complexity is addressed by a partitioning of the reduced models. This means, that not only one set of bases is generated, but several sets of reduced bases for different solution regimes. During the simulation a switching between these sub-models is realized by an orthogonal projection. Since the usual partitioning criteria turn out to be inapt for the sample problem, the criterion used is a problem-specific one. It is obtained via a feature extraction of the present reduced solution.

To use a problem-specific feature extraction in order to partition the solution space is a new conceptual contribution. For the considered sample problem, it is the volume of the solids. Since the preferred growth directions of the solids are prescribed by parameters, which as well as the initial conditions are the same in all microscopic problems, solids with similar volumes are also of similar shape. The main principle of the partitioning strategy is in the offline phase to subdivide the set of snapshots into subsets with respect to the volume and to construct from each subset one basis set. In the online phase a reduced solution is searched for in the span of a certain basis set if the volume of the solid (of the reduced solution of the previous time-step) is an element of the interval of the volumes that are covered by this basis set.

The established reduced two-scale model consists of a detailed macroscopic problem for the temperature and of reduced microscopic problems for the concentration and the phase-field. It comprises a full offline-online decomposition for the reduced microscopic problems. In the offline phase, the reduced bases, the projection operators for basis change, and further quantities are precomputed. This phase is accepted to be costly, but only performed once. The online phase of the reduced microscopic model is of low order complexity – completely independent of the detailed microscopic discretization's complexity – and allows the reduced scheme to be used rapidly and multiply, i.e. for all macroscopic nodes and all steps in time. Numerical results show the efficiency of the reduction scheme. While the accuracy of the detailed solution is largely maintained, the computation time is reduced significantly.

Both developed schemes allow for an efficient numerical solution of the sample two-scale problem. However, their approaches are completely different. The one reduces the number of the microscopic problems. On contrary, the other one reduces their complexity. Consequently, the efficiency for the sample problem is further increasable by a combination of the schemes. What distinguishes them is their applicability to other two-scale problems. Since the reduced two-scale model is developed from snapshots of the sample problem, its solution qualifies only for an approximation to the sample problem's detailed solution. For example, it does not approximate the solution of a two-scale model for precipitation in porous media. In order to approximate this detailed problem's solution, the reduced model has to be developed from snapshots of the detailed problem's solution. That is in order to adapt to a new problem, a new reduced model must be build in a new offline phase. On the

contrary, the adaptive strategy is directly applicable to every two-scale model on condition that the variables on the different scales depend continuously on each other. What simply has to be adjusted is the metric that compares the evolution of the macroscopic fields and possibly the tolerance that limits the distance of similar evolutions.

Unlike the first two topics, which are primarily dealing with the development of numerical algorithms, the third topic of this thesis in Section 5 is devoted to the modeling and simulation of a physical process. The process of interest is precipitation in a porous medium whose pore-space is occupied by three substances: water, oil and a solid. The motivating background is the observation that the pore-space of a porous medium is usually occupied by many different substances like water, oil, air, Some substances can contain dissolved particles, others not. For example salt can dissolve in water but not in air or oil. Therefore, if a crystalline solid of salt is surrounded by water on the one side and oil on the other, then salt-particles can only dissolve in the water. Thus, in contact with water the solid can recede, but nothing happens when it is in contact with oil. The reverse reaction is also possible: dissolved particles in the water can precipitate on the solid or on the grain – the boundary of the pore-space. The concentration of particles is constantly equal to zero in the oil and to one in the solid. On contrary, due to precipitation, dissolution and transport, it is variable in the water.

The combination of several modern modeling techniques results in an upscaled model that allows for an efficient numerical solution. Firstly, a pore-scale phase-field model is developed. The model describes the evolution of three phase-fields and the evolution of the concentration of the dissolved particles in the water. Besides by precipitation and dissolution, the evolution of the concentration is also influenced by diffusion. Motivated by the Diffuse Domain Approximation method introduced in [44], each phase-field is treated as a smooth approximation to the characteristic function – in the sharp-interface sense – of one of the three substances involved: water, oil and solid. Within a small phase-transition region a phase-field varies smoothly from 1 inside a region occupied by one of the substances to 0 inside the regions occupied by the two other substances. A formal asymptotic analysis shows that the solution of the phase-field model approximates in the limit, that is for the width $\xi > 0$ of the phase-transition regions tending to zero, the solution of a suitable sharp-interface model. Secondly, considering a situation with periodically distributed grains and solids with a period of scale $\epsilon > 0$, the application of a formal periodic homogenization technique to the pore-scale model yields in the limit for $\epsilon \rightarrow 0$ a two-scale model. It is a suitable approximation to the original problem if the dissolved particles in the water diffuse on the Darcy-scale. It consists of a macroscopic homogenized diffusion equation for the concentration of particles in the water, and, for each point of the macroscopic domain, of local cell problems for the evolution of the three phases. The variables on the different scales are continuously interdependent: the growth of the microscopic solid is influenced by the macroscopic concentration of the dissolved particles in the water, and vice versa the change of the pore structure influences the evolution of the concentration. Thirdly, based on the adaptive solution strategy developed in Section 3, exploiting these continuous inter-scale dependencies, an adaptive scheme is developed that allows for an efficient numerical solution.

In summary, a novel efficiently solvable model is established that describes Darcy-scale diffusion and pore-scale precipitation in porous media with three phases occupying the pore-space. Numerical results of the upscaled problem demonstrate the interdependence

of the evolution of the three phases and the evolution of the concentration of the dissolved particles in the water. The higher the concentration the faster the solid grows. The larger the volume fraction of the water on the pore-space volume, the stronger the Darcy-scale diffusion of the dissolved particles.

What the three topics of this thesis have in common is that all of them deal with two-scale models. Two of them are devoted to the development of numerical strategies aiming for efficient solutions. The third one discusses a physical process that is fundamental to e.g. prognosis models for soil salinization.

The outline of this thesis is the following. Section 2 provides a brief introduction into phase-field modeling and homogenization. Furthermore, it presents an estimate for the difference of microscopic solutions of the sample problem, that hints at a suitable metric in order to measure the distance of the macroscopic temperature evolutions. The main results of this thesis are presented in the Sections 3 - 5. Section 3 presents the adaptive solution strategy for two-scale models, Section 4 the reduced two-scale model for solidification in a binary mixture, and finally Section 5 is devoted to the modeling and simulation of the described precipitation process in porous media. Every section comprises a short introduction such that it is understandable independently of the other ones.

Section 3 results from joint work with Christof Eck, which is published by *J. Comp. Phys.*, [49]. Section 4 results from joint work with Bernard Haasdonk, which is published as preprint [50] and accepted for publication by *Adv. Comput. Math.*. Section 5 results from joint work with I. Sorin Pop and Christian Rohde.

2 A two-scale phase-field model for solidification

Throughout this thesis two-scale phase-field models are considered. The Sections 3 and 4 use two-scale phase-field models for solidification as showcases in order to validate the developed numerical solution schemes. Section 5 develops a two-scale phase-field model for precipitation in a porous medium, where it firstly develops a pore-scale phase-field model that approximates a suitable sharp-interface limit, and thereafter it applies a homogenization technique to the pore-scale model that results in an upscaled two-scale phase-field model. However, since such a detailed construction and description is presented for the first time in Section 5 and there is no background material presented in the Sections 3 and 4, this section provides a brief introduction into phase-field modeling and into the theory of homogenization. It is based on [20, 21, 22] considering a phase-field model for solidification in a binary mixture with evolution of equiaxed dendritic solids. Details on solidification and dendritic growth can be found in e.g. [16, 43]

2.1 The microscopic phase-field model

The transformation of a thermodynamic system from one phase of matter to another is called phase transition. A transition from liquid to solid is called solidification, and vice versa melting. In a simple setting of no undercooling, the material is liquid if its temperature is above the equilibrium melting point $T_M \in \mathbb{R}$, and solid if the temperature is below. During solidification latent heat $L > 0$ is released, and absorbed in the process of melting. The process of lowering a material's temperature below its melting point is called undercooling if the material does not become solid, but instead stays liquid. Undercooling occurs for example if no seed is available around which a solid can grow.

In case of a mixture, the equilibrium melting point $T_M = T_M(c) \in \mathbb{R}$ depends on the composition of the material and on the melting points of the pure components. Typically, the composition is described by concentrations $c = (c_1, \dots, c_n) \in [0, 1]^n$, $\sum_{i=1}^n c_i = 1$, where n is the number of the components. The composition of the mixture usually differs at the solid-liquid interface, that is in liquid it is $c_\ell \in [0, 1]^n$ and in solid $c_s \in [0, 1]^n$. The difference $c_\ell - c_s$ is called miscibility gap.

Dendritic solids, or simply dendrites, result from instabilities in the liquid-solid interface. Such an instability may be driven by heat or solute diffusion. Equiaxed dendrites typically result from heat diffusion, and it is usually solute diffusion that causes the evolution of columnar dendrites. The symmetrical shape is caused by the crystal structure of the solid material. Figure 2.1 sketches both types of dendrites.

An equiaxed dendritic crystal evolves from a small solid kernel in an undercooled melt. The latent heat that is released during the solidification has to be transported away from the interface through the liquid phase. This is only possible if the temperature in the liquid surrounding the solid is smaller than in the solid itself. Consequently, if a small perturbation in the interface occurs, caused by the crystal structure for instance, then the forefront of the perturbation is surrounded by a colder liquid than the rest of the solid. The steeper the temperature gradient, the faster the latent heat released is carried away. Consequently, the forefront advances rapidly and evolves into a dendritic finger, whereas the remainder of the interface advances only slowly.

Sharp-interface (SI) and phase-field (PF) models are two well-known model classes that

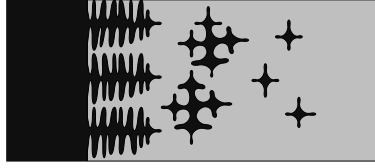


Figure 2.1: Columnar (on the left) and equiaxed dendritic structures, [22].

are widely used in literature in order to model phase transitions and solidification processes. See for example [9, 12, 13]. SI models distinguish sharply between the phases and use hypersurfaces to model the interfaces, [57]. Dealing with hypersurfaces is, however, demanding from the analytical point of view, because singularities may occur if for example two interfaces collide, as well as from the numerical point of view, since the computational mesh must track the interface.

Unlike SI models, PF models do not distinguish sharply between the phases. In fact it is assumed that a transition from one phase to another is smooth. Such a transition takes place in a typically very thin phase transition region of order $\xi > 0$. It is assumed, that inside this region the material is in an intermediate state between the two pure phases. An order parameter ϕ – the phase-field – describes the transition. It varies smoothly from its liquid value -1 to its solid value 1 . The evolution of ϕ is modeled by a partial differential equation. Usually it is possible to justify a phase-field approach by an asymptotic expansion that shows that the solution of the PF model converges to the solution of a suitable SI model if the width of the phase transition regions tends to zero. Therefore, the phase-field is interpretable as smooth approximation to the phase-indicator functions in a sharp-interface setting as depicted in Figure 2.2. Such an asymptotic expansion is carried out e.g. in [10] but also in Section 5 of this thesis. The justification can also be made more rigorous as e.g. shown in [11].

The remainder of this subsection presents a phase-field model for solidification in a binary mixture and specifies the conditions that must be met such that the model is well-posed, [21, 22]. Initially, the notation of various types of function spaces is fixed. Let $M \subset \mathbb{R}^N$ be an open domain with sufficiently smooth boundary and let \overline{M} denote its closure. The space $L_r(M)$ with $r \in [1, \infty]$ contains all Lebesgue-measurable functions $f : M \rightarrow \mathbb{R}$ such that $|f|^r$ is (Lebesgue-)integrable if $r < \infty$, or whose essential supremum exists if $r = \infty$. $C^\alpha(M)$ denotes the space of all functions $f : \overline{M} \rightarrow \mathbb{R}$ which have continuous derivatives in \overline{M} up to order $\alpha \in \mathbb{N}$. It is distinguished between the space C^α containing the functions with continuous derivatives of order α , and the set $C^{\alpha-1,1}$ of functions with Lipschitz-derivatives of order $\alpha - 1$. The space $W_r^\alpha(M)$ denotes the Sobolev space for an integer α or the Sobolev-Slobodeckii space for a non-integer α which contains all functions whose derivatives up to order α belong to $L_r(M)$. For $r = 2$ this space is also denoted by $H^\alpha(M) = W_2^\alpha(M)$. The spaces with vanishing traces (for sufficiently big α) are denoted by $\dot{C}^\alpha(M)$, $\dot{W}_r^\alpha(M)$ and $\dot{H}^\alpha(M)$. Their dual spaces are $W_r^{-\alpha}(M) = \left(\dot{W}_{r/(r-1)}^\alpha(M)\right)^*$, and the corresponding space $H^{-\alpha}(M)$. The anisotropic generalizations of these spaces for a time-space cylinder $I \times M$ with an interval I are denoted by $C^{\alpha,\beta}(I \times M)$, $W_r^{\alpha,\beta}(I \times M)$ and $H^{\alpha,\beta}(I \times M)$. The first index α indicates the regularity with respect to the time and the second index β that with respect to the spatial derivatives. In case of $\alpha = \beta$ only one index is present.

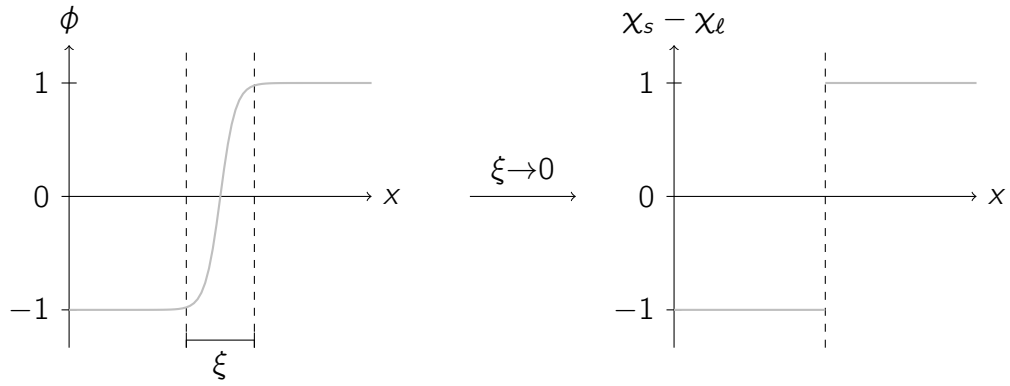


Figure 2.2: Behavior of the phase-field ϕ in a cross-section through the diffuse interface between liquid and solid: ϕ varies smoothly from -1 in liquid to 1 in solid. For the width $\xi > 0$ of the phase-transition region tending to zero the phase-field ϕ converges to the function $\chi_s - \chi_l$, where χ_s denotes the characteristic function of the region occupied by the solid in a sharp-interface setting, and χ_l the characteristic function of the region occupied by the liquid.

The following assumptions shall hold in the remainder of this section.

Assumption 2.1. Suppose $\Omega \subset \mathbb{R}^N$ is a domain of dimension $N \in \{2, 3\}$ with Lipschitz boundary $\Gamma = \partial\Omega$ with outer-normal n_r , and $J(\mathcal{T})$ is a time-interval $J(\mathcal{T}) = [0, \mathcal{T}]$ with $\mathcal{T} > 0$. Let $T, T_1, T_2, c, c_1, c_2, \phi, \phi_1, \phi_2 : J(\mathcal{T}) \times \Omega \rightarrow \mathbb{R}$ and $X, X_1, X_2 : J(\mathcal{T}) \times \Omega \rightarrow \mathbb{R}^N$. Suppose the tensors $K = K(\phi), D_1 = D_1(\phi) \in C^{0,1}(\mathbb{R}; \mathbb{R}^{N,N})$ are symmetric, elliptic and bounded, where

$$k_0|z|^2 \leq z^T K z \leq k_1|z|^2 \text{ and } d_0|z|^2 \leq z^T D_1 z \leq d_1|z|^2 \text{ for all } z \in \mathbb{R}^N \quad (2.1)$$

with constants $0 < k_0 \leq k_1$ and $0 < d_0 \leq d_1$ that are independent of ϕ . Suppose $D_2 = D_2(c, \phi) \in C^{0,1}(\mathbb{R}^2; \mathbb{R}^{N,N})$ is Lipschitz and bounded with constants that are independent of (c, ϕ) , and $D_2(c, \phi) = 0$ for $c \notin [0, 1]$. Let $T_r \in H^1(J(\mathcal{T}) \times \Omega)$, $T_0 \in W_r^{1,2}(J(\mathcal{T}) \times \Omega)$ with an $r > 1 + \frac{N}{2}$, $c_0 \in W_{s_1}^{2-2/s_1}(\Omega)$ with $1 + \frac{N}{2} < s_1 < 3$, $s_1 \leq r$, $c_0 \in [0, 1]$, $\phi_0 \in W_{s_2}^{2-2/s_2}(\Omega)$ with $s_2 > N + 2$, and $\nabla \phi_0 \cdot n_r = 0$ on Γ . Suppose $q : \mathbb{R}^N \times \mathbb{R}^3 \rightarrow \mathbb{R}$ is measurable and satisfies the growth-condition

$$|q(X, T, c, \phi)| \leq C_0(1 + |T| + |c|) \quad (2.2)$$

with a constant $C_0 > 0$ that is independent of (X, T, c, ϕ) , and that q is Lipschitz in the sense

$$\begin{aligned} & |q(X_1, T_1, c_1, \phi_1) - q(X_2, T_2, c_2, \phi_2)| \\ & \leq C_1(|T_1 - T_2| + |c_1 - c_2| + |\phi_1 - \phi_2|) + C_2(1 + |T_1| + |c_1|)|X_1 - X_2| \end{aligned} \quad (2.3)$$

with constants $C_1, C_2 > 0$ that are independent of $(X_1, X_2, T_1, T_2, c_1, c_2, \phi_1, \phi_2)$. Suppose $L, \alpha, \xi > 0$ are positive constants and $p(\phi) = \frac{1}{2}(1 - \phi^2)^2$.

Let $T = T(t, x)$ denote the temperature, $c = c(t, x)$ the concentration of one component of the binary mixture and $\phi = \phi(t, x)$ the phase-field. The following phase-field model models a solidification process in a binary mixture.

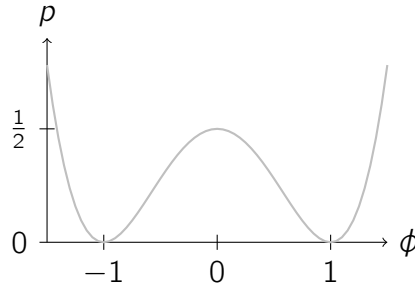


Figure 2.3: Double-well potential $p(\phi) = \frac{1}{2}(1 - \phi^2)^2$.

Problem 2.2. Given $T_\Gamma : J(\mathcal{T}) \times \Gamma \rightarrow \mathbb{R}$ and $T_0, c_0, u_0 : \Omega \rightarrow \mathbb{R}$, find functions $T = T(t, x)$, $c = c(t, x)$ and $\phi = \phi(t, x)$ that satisfy

$$\begin{aligned}
 \partial_t T + \frac{1}{2} \partial_t \phi - \nabla \cdot (K(\phi) \nabla T) &= 0 && \text{in } J(\mathcal{T}) \times \Omega \\
 \partial_t c - \nabla \cdot (D_1(\phi) \nabla c) - \nabla \cdot (D_2(c, \phi) \nabla \phi) &= 0 && \text{in } J(\mathcal{T}) \times \Omega \\
 \alpha \xi^2 \partial_t \phi - \xi^2 \Delta \phi + p'(\phi) + q(\nabla \phi, T, c, \phi) &= 0 && \text{in } J(\mathcal{T}) \times \Omega \\
 T &= T_\Gamma && \text{on } J(\mathcal{T}) \times \Gamma, \\
 -(D_1(\phi) \nabla c + D_2(c, \phi) \nabla \phi) \cdot n_\Gamma &= 0 && \text{on } J(\mathcal{T}) \times \Gamma, \\
 -\nabla \phi \cdot n_\Gamma &= 0 && \text{on } J(\mathcal{T}) \times \Gamma, \\
 T(0, x) &= T_0(x) && \text{in } \Omega, \\
 c(0, x) &= c_0(x) && \text{in } \Omega, \\
 \phi(0, x) &= \phi_0(x) && \text{in } \Omega.
 \end{aligned} \tag{2.4}$$

The parameter $L > 0$ describes the latent heat that is released during the phase transition from liquid to solid. $K = (K_{ij}(\phi))_{i,j=1}^N$ the heat conductivity and $D_1 = (D_{1,ij}(\phi))_{i,j=1}^N$ the solute diffusivity. The term $\nabla \cdot (D_2(c, \phi) \nabla \phi)$ generates transition layers in the concentration field from transition layers in the phase-field and thereby realizes the miscibility gap. The function p is a double-well potential which is minimal in liquid and solid, see Figure 2.3. The Laplacian of ϕ enforces the smooth transition from liquid to solid. The width of the phase transition regions is proportional to the parameter $\xi > 0$. Their actual width is determined by a competition between $-\xi^2 \Delta \phi$ and $p'(\phi)$. $\alpha > 0$ is a time relaxation parameter. The function q describes the deviation from the equilibrium melting point and triggers the dendritic growth.

Theorem 2.3. Let the Assumption 2.1 hold true. Then a unique weak solution (T, c, ϕ) to the Problem 2.2 exists. It satisfies $T \in W_r^{1,2}(J(\mathcal{T}) \times \Omega)$, $c \in W_{s_1}^{1,2}(J(\mathcal{T}) \times \Omega)$ and $\phi \in W_{s_2}^{1,2}(J(\mathcal{T}) \times \Omega)$.

Proof. Section 3.1 in [22]. □

2.2 The two-scale phase-field model

The Problem 2.2 is able to describe the evolution of an arbitrary number of equiaxed dendrites within a solidification process in a binary mixture. However, from the numerical point of view the number of dendrites that can be computed is limited. This is due to the fact,

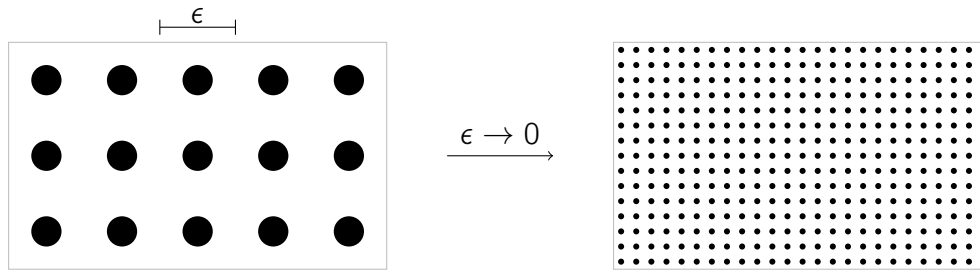


Figure 2.4: Homogenization for $\epsilon \rightarrow 0$.

that the phase transition regions need to be resolved by a very fine computational mesh. Therefore, an increasing number of dendrites comes along with an increasing number of unknowns. Even a fast computer allows only the simulation of a few crystals within an acceptable computation time. In particular this holds true in a three dimensional spatial setting.

A much more promising approach, allowing in the end the simulation of more than only a few crystals, is to identify and separate different length scales in the process. This is done by a formal asymptotic expansion with respect to the scale $\epsilon > 0$ of the dendrites. Considered is a sequence of problems with periodically distributed dendrites of varying scale ϵ and a limit problem for $\epsilon \rightarrow 0$ is constructed, see Figure 2.4. The heterogeneous material is replaced by a homogeneous fictitious one, whose global characteristics are a good approximation of the heterogeneous ones, [15]. Therefore, the limit problem for $\epsilon \rightarrow 0$ is used as an approximation to the original problem for situations with small but non-vanishing scale ϵ .

This subsection provides a brief introduction into the theory of homogenization and very briefly recapitulates the formal asymptotic expansion of the model in Problem 2.2 that was presented in [21]. The interested reader is referred to [15, 32, 34] for more details on homogenization.

Homogenization deals with problems involving different length scales. An example is heat conduction in a fine binary mixture whose two components conduct the heat differently fast. The heterogeneous material is replaced by a fictitious homogeneous material whose macroscopic characteristics are a good approximation of the original ones. For that purpose, a family of problems is considered which depend on a scale parameter $\epsilon > 0$, and the limit for $\epsilon \rightarrow 0$ of the solutions of the problems is studied. In many cases the solutions converge and their limit can be represented as a solution of a (different) homogenized problem. The theory aims at the construction of this homogenized problem, which is used as approximation to the original heterogeneous problem for situations with small but non-vanishing scale ϵ .

An initially periodic microstructure is generated by

$$T_0^{(\epsilon)}(x) = T_0^{(0)}\left(x, \frac{x}{\epsilon}\right), \quad c_0^{(\epsilon)}(x) = c_0^{(0)}\left(x, \frac{x}{\epsilon}\right), \quad \phi_0^{(\epsilon)}(x) = \phi_0^{(0)}\left(x, \frac{x}{\epsilon}\right) \quad \text{in } \Omega \quad (2.5)$$

with functions $T_0^{(0)}, c_0^{(0)}, \phi_0^{(0)} \in C^0(\Omega; C_{\#}^0(Y))$. The subscript $\#$ in the notation of a function space indicates that its elements satisfy periodic boundary conditions with respect to $y \in Y$. The Figure 2.5 sketches the discrete situation. The domain Y is a unit cell, that is Y is a bounded, simply connected Lipschitz domain satisfying the property that the whole space \mathbb{R}^N can be represented as a union of shifted copies of the closure \bar{Y} with

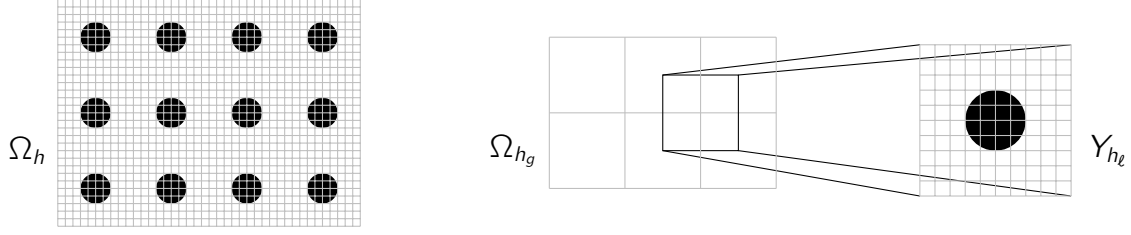


Figure 2.5: The pure microscopic grid Ω_h and the two-scale grid $\Omega_{h_g} \times Y_{h_g}$.

vanishing intersection of their interiors. For simplicity it is assumed that $Y = [0, 1]^N$. The set $C_{\#}^0(Y)$ contains all periodic continuous functions in \mathbb{R}^N with the periodicity cell Y .

Let $(T_\epsilon, c_\epsilon, \phi_\epsilon) = (T_\epsilon, c_\epsilon, \phi_\epsilon)(t, x)$ be the solution to Problem 2.2 on scale $\epsilon > 0$ with the above initial data. Since a limit problem shall be constructed, the existence of an asymptotic expansion of the solution is assumed,

$$\begin{aligned} T_\epsilon(t, x) &= \sum_{i=0}^{\infty} \epsilon^i T_i(t, x, \frac{x}{\epsilon}), \\ c_\epsilon(t, x) &= \sum_{i=0}^{\infty} \epsilon^i c_i(t, x, \frac{x}{\epsilon}), \\ \phi_\epsilon(t, x) &= \sum_{i=0}^{\infty} \epsilon^i \phi_i(t, x, \frac{x}{\epsilon}), \end{aligned} \quad (2.6)$$

with Y -periodic functions $T_i, c_i, \phi_i : J(\mathcal{T}) \times \Omega \times Y \rightarrow \mathbb{R}$ for $i = 0, 1, \dots$. The existence of the asymptotic expansion is not guaranteed. However, the assumption is justified in [21]. The gradient of a function $x \mapsto u(x, \frac{x}{\epsilon})$ is given by

$$\nabla u(x, \frac{x}{\epsilon}) = \nabla_x u(x, \frac{x}{\epsilon}) + \frac{1}{\epsilon} \nabla_y u(x, \frac{x}{\epsilon}), \quad (2.7)$$

where ∇_x resp. ∇_y denotes the gradient with respect to the first resp. the second variable of u .

In order to obtain a well-defined asymptotic limit problem some of the parameters are scaled in dependence of ϵ ,

$$\xi = \epsilon \xi_0, \quad \alpha = \epsilon^{-2} \alpha_0, \quad D_1 = \epsilon^2 D_1^{(0)}, \quad D_2 = \epsilon^2 D_2^{(0)}. \quad (2.8)$$

The size of a dendrite is proportional to ϵ , consequently the width of the phase transition regions must be proportional to ϵ . The relaxation parameter α is scaled such that the total factor $\alpha \xi$ remains constant in the third evolution equation of Problem 2.2. Since it is typical of binary mixtures that heat diffuses rapidly but solute only slowly, only the solute diffusivities are scaled by ϵ^2 .

The asymptotic expansion (2.6), the formal relation (2.7), the scaling of the parameters (2.8) and Taylor expansions for the functions depending on the solution $(T_\epsilon, c_\epsilon, \phi_\epsilon)$ with expansion point (T_0, c_0, ϕ_0) are employed in (2.4), the coefficients of the different powers of the scale ϵ are compared and the limit problem is constructed. Finally a two-scale model is obtained that is suitable for material with fast heat and slow solute diffusion. The temperature is assumed to be essentially constant on the microscopic scale, whereas solute transport is neglected on the macroscopic scale. The model consists of a homogenized macroscopic heat equation for the temperature and for each point of the macroscopic domain of a microscopic cell problem for the concentration and the phase-field.

The macroscopic homogenized heat equation for the macroscopic temperature $T = T(t, x)$ reads

$$\partial_t T + \frac{1}{2} \partial_t \bar{\phi}^Y - \nabla_x (K^*(\phi) \nabla_x T) = 0 \text{ in } J(\mathcal{T}) \times \Omega. \quad (2.9)$$

The averaged phase-field

$$\overline{\phi(t, x)}^Y = \frac{1}{|Y|} \int_Y \phi(t, x, y) dy \quad (2.10)$$

depends on the solution of the local microscopic cell problem. The effective heat conductivity K^* depends also on the local phase field, that is

$$K_{ij}^*(\phi(t, x, y)) = \frac{1}{|Y|} \int_Y \sum_{k=1}^N K_{ik}(\phi(t, x, y)) (\delta_{jk} + \partial_{y_k} H_j(\phi(t, x, y))) dy \quad (2.11)$$

with the unique solutions H_j of the cell problems

$$-\nabla_y \cdot (K(\phi) \nabla_y H_j) = e_j \cdot \nabla_y K(\phi) \text{ in } J(\mathcal{T}) \times \Omega \times Y \text{ for } j = 1, \dots, N \quad (2.12)$$

with periodic boundary conditions on ∂Y and the constraint $\int_Y H_j dy = 0$. The macroscopic equation is supplemented by a Dirichlet boundary condition and an initial temperature $T(0, x) = T_0(x)$ for all $x \in \Omega$.

The microscopic cell problems for the microscopic concentration $c = c(t, x, y)$ and the microscopic phase-field $\phi = \phi(t, x, y)$ describe the liquid-solid phase transition in the binary mixture,

$$\begin{aligned} \partial_t c - \nabla_y \cdot (D_1(\phi) \nabla_y c) - \nabla_y \cdot (D_2(c, \phi) \nabla_y \phi) &= 0 \text{ in } J(\mathcal{T}) \times \Omega \times Y, \\ \alpha \xi^2 \partial_t \phi - \xi^2 \Delta_y \phi + p'(\phi) + q(\nabla \phi, T, c, \phi) &= 0 \quad \text{in } J(\mathcal{T}) \times \Omega \times Y. \end{aligned} \quad (2.13)$$

It is completed by periodic boundary conditions on ∂Y and the prescribed initial data $c(0, x, y) = c_0(x, y)$ and $\phi(0, x, y) = \phi_0(x, y)$ for all $(x, y) \in \Omega \times Y$.

Article [20] proves that if the Assumption 2.1 is met then a unique weak solution to the two-scale problem (2.9)-(2.13) exists. The interested reader is referred to [21] for details on the construction of this model and to Section 5 carrying out in detail the construction of a two-scale model for precipitation in porous media.

Obviously, the assumption of periodically distributed dendrites is highly unrealistic from the physical point of view. From the numerical point of view it is, however, at least very helpful. The dendrites in the two-scale model can be computed in parallel, due to the periodic boundary conditions in the microscopic problems, whereas they need to be computed simultaneously in the pure microscopic model. The simultaneity of the pure microscopic model limits the number of the dendrites that can be simulated to a very few. The number is still limited in the two-scale model, but its limit is much higher.

2.3 Further analysis of the two-scale model's microscopic problem

The adaptive solution strategy to be developed in Section 3 cracks the limitation of the number of the dendrites that can be computed by the discrete two-scale model. It solves only those microscopic problems (2.13) that are influenced by outstanding macroscopic temperature evolutions. The microscopic data of unsolved problems is approximated by the data of solved problems. This approach is based upon the observation that two microstructures develop similar features if they develop from similar initial states and if their evolution is influenced by similar temperature evolutions. This subsection shows that the $L_2(Y)$ -distance of two microscopic solutions of (2.13) at any point in time $t_0 \in J(\mathcal{T})$ is

bounded by a multiple of a weighted $L_\tau([0, t_0])$ -distance of the two influencing temperature evolutions.

Let $\langle \cdot, \cdot \rangle_Y$ denote the dual pairing in $H^1(Y)$. Furthermore, let $H_{\#}^1(Y)$ denote the closure of $C_{\#}^\infty(Y)$ for the H^1 -norm. Recall that the subscript $\#$ in the notation of a function space indicates that its elements satisfy periodic boundary conditions with respect to $y \in Y$. The microscopic problem (2.13) in $x \in \Omega$ has the following variational formulation.

Problem 2.4. Find functions $c = c(\cdot, x, \cdot)$, $\phi = \phi(\cdot, x, \cdot) \in H^{1/2,1}(J(\mathcal{T}) \times Y)$ that satisfy the initial conditions $c(0, x, y) = c_0(x, y)$ and $\phi(0, x, y) = \phi_0(x, y)$ such that for all test functions $v, w \in H_{\#}^1(J(\mathcal{T}) \times Y)$ the equations

$$\int_{J(\mathcal{T})} \langle \partial_t c, v \rangle_Y + \int_Y ((D_1(\phi) \nabla_y c + D_2(c, \phi) \nabla_y \phi) \cdot \nabla_y v) dy) dt = 0, \quad (2.14)$$

$$\begin{aligned} & \int_{J(\mathcal{T})} \langle \alpha \xi^2 \partial_t \phi, w \rangle_Y dt + \\ & + \int_{J(\mathcal{T}) \times Y} (\xi^2 \nabla_y \phi \cdot \nabla_y w + (p'(\phi) + q(\nabla \phi, T, c, \phi)) w) dy) dt = 0 \end{aligned} \quad (2.15)$$

hold.

Theorem 2.5. Let the Assumption 2.1 hold true. Assume $T^{(\ell)} \in L_s(J(\mathcal{T}))$, $c_0^{(\ell)}, \phi_0^{(\ell)} \in W_{s\#}^{2-2/s}(Y)$ for $\ell = 1, 2$ with $s > 1 + \frac{N}{2}$. Let $1 < \tau \leq s$, $\lambda \geq 0$ and $w_\lambda = w_\lambda(t) := e^{\lambda t}$. Then the two unique solutions $(c^{(1)}, \phi^{(1)})$ resp. $(c^{(2)}, \phi^{(2)})$ of the problems (2.14) and (2.15) with initial data $(c_0^{(1)}, \phi_0^{(1)})$ resp. $(c_0^{(2)}, \phi_0^{(2)})$ and temperature evolution $T^{(1)}$ resp. $T^{(2)}$ satisfy

$$\begin{aligned} & \sum_{u=c,\phi} \left(\|w_\lambda (u^{(1)} - u^{(2)})\|_{L_\infty(J(\mathcal{T}); L_2(Y))} + \|w_\lambda (u^{(1)} - u^{(2)})\|_{L_2(J(\mathcal{T}); H^1(Y))} \right) \\ & \leq C(\lambda) \left(\|w_\lambda (T^{(1)} - T^{(2)})\|_{L_\tau(J(\mathcal{T}))} + \sum_{u=c,\phi} \|u_0^{(1)} - u_0^{(2)}\|_{L_2(Y)} \right) \end{aligned} \quad (2.16)$$

with a constant $C(\lambda)$ depending exponentially on λ .

Proof. Lemma 3.2 in [20] proves that a unique solution (c, ϕ) to the problem (2.14) and (2.15) exists. It satisfies $c \in [0, 1]$ and $c, \phi \in W_s^{1,2}(J(\mathcal{T}) \times Y)$. The following proof follows the argumentation of a part of the proof of Lemma 3.2 in [20] that proves the validity of (2.16) for $\lambda = 0$ and $\tau = 2$.

Let $\kappa > 0$ be sufficiently large and χ_{t_0} be the indicator-function of the time-interval $J(t_0) = (0, t_0]$ for $t_0 \in J(\mathcal{T})$. For the first solution $(c^{(1)}, \phi^{(1)})$ take the test functions $v = \chi_{t_0} w_\lambda^2 (c^{(1)} - c^{(2)})$ in (2.14) and $w = \kappa \chi_{t_0} w_\lambda^2 (\phi^{(1)} - \phi^{(2)})$ in (2.15). For the second solution take $-v$ and $-w$. The four equations are summed up and processed in the following. Please note that w_λ and $\partial_t w_\lambda$ are of course elements of $L_\infty(J(t_0))$.

Define

$$\begin{aligned} \langle u, v \rangle_{t_0} &= \int_{J(t_0)} \langle u, v \rangle_Y dt, \\ (u, v)_{t_0} &= \int_{J(t_0) \times Y} u \cdot v dy dt, \\ \|\cdot\|_{r,s,t_0} &= \|\cdot\|_{L_r(J(t_0); L_s(Y))}, \end{aligned} \quad (2.17)$$

where $1 \leq r, s \leq \infty$.

For $u = c^{(1)} - c^{(2)}$ and $u_0 = c_0^{(1)} - c_0^{(2)}$ resp. $u = \phi^{(1)} - \phi^{(2)}$ and $u_0 = \phi_0^{(1)} - \phi_0^{(2)}$, there follows

$$\begin{aligned} & \langle \partial_t u, w_\lambda^2 u \rangle_{t_0} \\ &= \int_{J(t_0) \times Y} \partial_t \left(\frac{1}{2} u^2 w_\lambda^2 \right) - \frac{1}{2} u^2 \partial_t w_\lambda^2 \, dy \, dt \\ &= \frac{1}{2} \left(w_\lambda^2(t_0) \|u(t_0)\|_{L_2(Y)}^2 - \|u_0\|_{L_2(Y)}^2 \right) - \lambda \|w_\lambda u\|_{L_2(J(t_0) \times Y)}^2. \end{aligned} \quad (2.18)$$

Define $D_1^{(\ell)} = D_1(\phi^{(\ell)})$ and $D_2^{(\ell)} = D_2(c^{(\ell)}, \phi^{(\ell)})$ for $\ell = 1, 2$. Then

$$\begin{aligned} & D_1^{(1)} \nabla_y c^{(1)} - D_1^{(2)} \nabla_y c^{(2)} + D_2^{(1)} \nabla_y \phi^{(1)} - D_2^{(2)} \nabla_y \phi^{(2)} \\ &= D_1^{(1)} \nabla_y (c^{(1)} - c^{(2)}) + \left(D_1^{(1)} - D_1^{(2)} \right) \nabla_y c^{(2)} + \\ & \quad + D_2^{(1)} \nabla_y (\phi^{(1)} - \phi^{(2)}) + \left(D_2^{(1)} - D_2^{(2)} \right) \nabla_y \phi^{(2)}. \end{aligned} \quad (2.19)$$

The ellipticity (2.1) of D_1 yields

$$\begin{aligned} & \|w_\lambda \nabla_y (c^{(1)} - c^{(2)})\|_{L_2(J(t_0) \times Y)}^2 \\ & \leq C \left(D_1^{(1)} \nabla_y (c^{(1)} - c^{(2)}), \nabla_y (c^{(1)} - c^{(2)}) w_\lambda^2 \right)_{t_0}. \end{aligned} \quad (2.20)$$

D_2 is bounded, thus for an arbitrarily small $\eta > 0$ it follows

$$\begin{aligned} & \left| \left(D_2^{(1)} \nabla_y (\phi^{(1)} - \phi^{(2)}), \nabla_y (c^{(1)} - c^{(2)}) w_\lambda^2 \right)_{t_0} \right| \\ & \leq \eta \|w_\lambda \nabla_y (c^{(1)} - c^{(2)})\|_{2,2,t_0}^2 + C(\eta) \|w_\lambda \nabla_y (\phi^{(1)} - \phi^{(2)})\|_{2,2,t_0}^2. \end{aligned} \quad (2.21)$$

Due to the Lipschitz-properties of D_1 and D_2 , the absolute R of the integral on $J(t_0) \times Y$ of the remaining terms of (2.19) scalar multiplied by $\nabla_y (\phi^{(1)} - \phi^{(2)})$ is bounded by

$$\begin{aligned} R &= \left| \left(\left(D_1^{(1)} - D_1^{(2)} \right) \nabla_y c^{(2)} + \left(D_2^{(1)} - D_2^{(2)} \right) \nabla_y \phi^{(2)}, \nabla_y (c^{(1)} - c^{(2)}) w_\lambda^2 \right)_{t_0} \right| \\ & \leq \eta \|w_\lambda \nabla_y (c^{(1)} - c^{(2)})\|_{2,2,t_0}^2 + \\ & \quad + C(\eta) \|\nabla_y \phi^{(2)}\|_{\sigma,\sigma,t_0}^2 \|w_\lambda (c^{(1)} - c^{(2)})\|_{\rho_1,\rho_1,t_0}^2 + \\ & \quad + C(\eta) \left(\|\nabla_y c^{(2)}\|_{\sigma,\sigma,t_0}^2 + \|\nabla_y \phi^{(2)}\|_{\sigma,\sigma,t_0}^2 \right) \|w_\lambda (\phi^{(1)} - \phi^{(2)})\|_{\rho_1,\rho_1,t_0}^2 \end{aligned} \quad (2.22)$$

with $\frac{1}{\sigma} + \frac{1}{\rho_1} = \frac{1}{2}$. The index σ is calculated from the embedding $W_s^{1,2}(J(t_0) \times Y) \hookrightarrow L_\sigma(J(t_0); W_\sigma^1(Y))$, that is $\sigma = \frac{(N+2)s}{N+2-s}$ for $s < N+2$, $\sigma < \infty$ for $s = N+2$ and $\sigma = \infty$ for $s > N+2$, see chapter 18 in [4]. Due to $s > 1 + \frac{N}{2}$ it is $\sigma > N+2$ and $\rho_1 < 2 + \frac{4}{N}$. For $u = c^{(1)} - c^{(2)}$ resp. $\phi^{(1)} - \phi^{(2)}$ follows

$$\|w_\lambda u\|_{\rho_1,\rho_1,t_0} \leq C \|w_\lambda u\|_{\mu_2,2,t_0}^{\mu_1} \|w_\lambda u\|_{2,\rho_2,t_0}^{1-\mu_1} \quad (2.23)$$

with $\mu_1 = \frac{2(\rho_2 - \rho_1)}{\rho_1(\rho_2 - 2)}$ and $\mu_2 = \frac{4(\rho_2 - \rho_1)}{4\rho_2 - 4 - \rho_1\rho_2}$, see Theorem 6.4.5 in [3]. The parameter ρ_2 is chosen such that the embedding $H^1(Y) \hookrightarrow L_{\rho_2}(Y)$ holds, that is $\rho_2 < \infty$ for $N = 2$ and $\rho_2 \leq 6$ for $N = 3$, see again chapter 18 in [4]. Due to the restriction $2 < \rho_1 < 2 + \frac{4}{N}$ it is

always possible to find an appropriate ρ_2 such that $0 < \mu_1 < 1$ and $1 \leq \mu_2 < \infty$ are well defined. This yields

$$\|w_\lambda u\|_{\rho_1, \rho_1, t_0}^2 \leq \eta \|w_\lambda u\|_{L_2(J(t_0); H^1(Y))}^2 + C(\eta) \|w_\lambda u\|_{\mu_2, 2, t_0}^2 \quad (2.24)$$

with an arbitrarily small $\eta > 0$. Therefore R in (2.22) is bounded by

$$\begin{aligned} R \leq & \eta \|w_\lambda (c^{(1)} - c^{(2)})\|_{L_2(J(t_0); H^1(Y))}^2 + C(\eta) \|w_\lambda (c^{(1)} - c^{(2)})\|_{\mu_2, 2, t_0}^2 \\ & + C(\eta) \left(\|w_\lambda (\phi^{(1)} - \phi^{(2)})\|_{\mu_2, 2, t_0}^2 + \|w_\lambda (\phi^{(1)} - \phi^{(2)})\|_{L_2(J(t_0); H^1(Y))}^2 \right). \end{aligned} \quad (2.25)$$

The Lipschitz-condition (2.3) of q , $q^{(i)} = q(\nabla_y \phi^{(i)}, T^{(i)}, c^{(i)}, \phi^{(i)})$ for $i = 1, 2$,

$$\begin{aligned} 1 < \tau_1 \leq s, \quad \tau_2 &= \max\left(\frac{\tau_1}{\tau_1 - 1}, 2\right), \\ 2 < \tau_3 \leq s, \quad \tau_4 &= \frac{2\tau_3}{\tau_3 - 2}, \\ \tau_5 &= \max(\tau_2, \tau_4), \end{aligned} \quad (2.26)$$

and an arbitrary small $\eta > 0$ yield

$$\begin{aligned} & \left| (q^{(1)} - q^{(2)}, (\phi^{(1)} - \phi^{(2)}) w_\lambda^2)_{t_0} \right| \\ & \leq C_0 (|T^{(1)} - T^{(2)}| + |c^{(1)} - c^{(2)}| + |\phi^{(1)} - \phi^{(2)}|, |\phi^{(1)} - \phi^{(2)}| w_\lambda^2)_{t_0} \\ & \quad + C_1 ((1 + |T^{(1)}| + |c^{(1)}|) |\nabla_y (\phi^{(1)} - \phi^{(2)})|, |\phi^{(1)} - \phi^{(2)}| w_\lambda^2)_{t_0} \\ & \leq C_2 \|w_\lambda (T^{(1)} - T^{(2)})\|_{L_{\tau_1}(J(t_0))}^2 + C_3 \|w_\lambda (c^{(1)} - c^{(2)})\|_{2, 2, t_0}^2 \\ & \quad + C_4 \|w_\lambda (\phi^{(1)} - \phi^{(2)})\|_{\tau_2, 2, t_0}^2 + \eta \|w_\lambda \nabla_y (\phi^{(1)} - \phi^{(2)})\|_{2, 2, t_0}^2 \\ & \quad + C_5(\eta) (\|T_1\|_{L_{\tau_3}(J(t_0))} + 2)^2 \|w_\lambda (\phi^{(1)} - \phi^{(2)})\|_{\tau_4, 2, t_0}^2 \\ & \leq C_2 \|w_\lambda (T^{(1)} - T^{(2)})\|_{L_{\tau_1}(J(t_0))}^2 + C_3 \|w_\lambda (c^{(1)} - c^{(2)})\|_{2, 2, t_0}^2 + \\ & \quad + \eta \|w_\lambda \nabla_y (\phi^{(1)} - \phi^{(2)})\|_{2, 2, t_0}^2 + C_6(\eta) \|w_\lambda (\phi^{(1)} - \phi^{(2)})\|_{\tau_5, 2, t_0}^2 \end{aligned} \quad (2.27)$$

for certain constants $C_0, \dots, C_6 > 0$.

Since p' is Lipschitz, the embedding $W_s^{1,2}(J(\mathcal{T}) \times Y) \hookrightarrow L_\infty(J(\mathcal{T}) \times Y)$ (for $s > 1 + N/2$) in combination with $\zeta_1 = \max(\tau_5, \mu_2, 2 + \delta)$ for all $0 < \delta \ll \infty$ and $\zeta_2 = \frac{\zeta_1}{\zeta_1 - 2}$, and the constant

$$C = 2 \left\| (\phi^{(1)})^2 + \phi^{(1)} \phi^{(2)} + (\phi^{(2)})^2 + 1 \right\|_{\zeta_2, \infty, t_0} \quad (2.28)$$

yield

$$\begin{aligned} & \left| (p'(\phi^{(1)}) - p'(\phi^{(2)}), (\phi^{(1)} - \phi^{(2)}) w_\lambda^2)_{t_0} \right| \\ & \leq \left| \left(2 \left((\phi^{(1)})^2 + \phi^{(1)} \phi^{(2)} + (\phi^{(2)})^2 + 1 \right) (\phi^{(1)} - \phi^{(2)}), (\phi^{(1)} - \phi^{(2)}) w_\lambda^2 \right)_{t_0} \right| \\ & \leq C \left\| w_\lambda^2 (\phi^{(1)} - \phi^{(2)})^2 \right\|_{\zeta_1/2, 2, t_0} \\ & \leq C \|w_\lambda (\phi^{(1)} - \phi^{(2)})\|_{\zeta_1, 2, t_0}^2. \end{aligned} \quad (2.29)$$

The combination of the estimates from above, a sufficiently small $\eta > 0$ and a sufficiently large $\kappa > 0$ yield

$$\begin{aligned} & \sum_{u=c,\phi} \left(w_\lambda^2(t_0) \left\| (u^{(1)} - u^{(2)})(t_0) \right\|_{L_2(Y)}^2 + \left\| w_\lambda \nabla_Y (u^{(1)} - u^{(2)}) \right\|_{2,2,t_0}^2 \right) \\ & \leq C_0(\eta, \kappa) \sum_{u=c,\phi} \left\| u_0^{(1)} - u_0^{(2)} \right\|_{L_2(Y)}^2 + C_1(\eta, \kappa) \left\| w_\lambda (T^{(1)} - T^{(2)}) \right\|_{L_{\tau_1}(J(t_0))}^2 \\ & \quad + C_2(\eta, \lambda) \sum_{u=c,\phi} \left\| w_\lambda (u^{(1)} - u^{(2)}) \right\|_{\zeta_{1,2,t_0}}^2, \end{aligned} \quad (2.30)$$

with constants $C_0, C_1, C_2 > 0$.

Because of Gronwall's Lemma, $2 < \xi_1 < \infty$, Young's inequality and the definitions

$$\begin{aligned} \tilde{u}(s) &:= w_\lambda(s) \left\| (c^{(1)} - c^{(2)})(s) \right\|_{L_2(Y)} \quad \text{for all } s \in [0, t_0], \\ \tilde{v}(s) &:= w_\lambda(s) \left\| (\phi^{(1)} - \phi^{(2)})(s) \right\|_{L_2(Y)} \quad \text{for all } s \in [0, t_0], \\ \tilde{w}(t_0) &:= \left\| c_0^{(1)} - c_0^{(2)} \right\|_{L_2(Y)} + \left\| \phi_0^{(1)} - \phi_0^{(2)} \right\|_{L_2(Y)} + \left\| w_\lambda (T^{(1)} - T^{(2)}) \right\|_{L_{\tau_1}(J(t_0))} \end{aligned} \quad (2.31)$$

for $t_0 \in J(\mathcal{T})$, the following implications are valid for certain constants $C_0, \dots, C_5 > 0$,

$$\begin{aligned} & \tilde{u}(t_0)^2 + \tilde{v}(t_0)^2 \\ & \leq C_0 \tilde{w}(t_0)^2 + C_1 \left(\int_{J(t_0)} \tilde{u}(s)^{\xi_1} ds \right)^{2/\xi_1} + C_1 \left(\int_{J(t_0)} \tilde{v}(s)^{\xi_1} ds \right)^{2/\xi_1} \\ & \Rightarrow \tilde{u}(t_0)^{\xi_1} + \tilde{v}(t_0)^{\xi_1} \leq C_2 \left(C_0 \tilde{w}(t_0)^{\xi_1} + C_1 \int_{J(t_0)} \tilde{u}(s)^{\xi_1} + \tilde{v}(s)^{\xi_1} dt \right) \\ & \Rightarrow \tilde{u}(t_0)^{\xi_1} + \tilde{v}(t_0)^{\xi_1} \leq C_3 \tilde{w}(t_0)^{\xi_1} \\ & \Rightarrow \tilde{u}(t_0) + \tilde{v}(t_0) \leq C_4 \tilde{w}(t_0) \leq C_5. \end{aligned} \quad (2.32)$$

This finally proves the Theorem. \square

Remark 2.6. *The condition $\tau > 1$ in Theorem 2.5 is essential. This is due to the fact that, in order that the Hölder inequality for $|T^{(1)} - T^{(2)}| |\phi^{(1)} - \phi^{(2)}|$ in (2.27) holds true, $\tau_1 = 1$ yields $\tau_2 = \infty$. But, if $\tau_2 = \infty$ then $\zeta_1 = \tau_5 = \tau_2 = \infty$ and the implications (2.32) do not hold.*

Fix $1 < \tau \leq s$, $\lambda \geq 0$ and $t_0 \in J(\mathcal{T})$. The weighted metric d ,

$$d(T_1, T_2; t_0, \lambda, \tau) = \sqrt[\tau]{\int_{J(t_0)} e^{-\lambda\tau(t_0-t)} |(T_1 - T_2)(t)|^\tau dt}. \quad (2.33)$$

measures the distance of two temperature-evolutions $T_1, T_2 \in L_s(J(t_0))$ in the time-interval $J(t_0)$. It is equipped with a fading memory if the history parameter λ does not vanish. The larger λ the faster the memory fades i.e. the smaller the significant time-interval.

An obvious consequence of Theorem 2.5 is the following one.

Corollary 2.7. *Let the assumptions of Theorem 2.5 be met. If $c_0^{(1)} = c_0^{(2)}$ and $\phi_0^{(1)} = \phi_0^{(2)}$, then for all $t_0 \in J(\mathcal{T})$ there follows*

$$\begin{aligned} & \left\| (c^{(1)} - c^{(2)})(t_0) \right\|_{L_2(Y)} + \left\| (\phi^{(1)} - \phi^{(2)})(t_0) \right\|_{L_2(Y)} \\ & \leq C(\lambda) d(T^{(1)}, T^{(2)}; t_0, \lambda, \tau). \end{aligned} \quad (2.34)$$

Therefore, the distance of two microscopic solutions is bounded by the product of a constant, that depends amongst others exponentially on λ , and the d -distance of the two influencing temperature evolutions. That is, the solution of the microscopic problem depends continuously on the influencing temperature evolution.

Corollary 2.7 presents the key to an adaptive solution scheme for the two-scale model. Disregarding the constant, the in the next section developed adaptive strategy assumes that the solution of a microscopic problem approximates appropriately the solution of another microscopic problem as long as the d -distance of their two influencing temperature evolutions is not larger than a certain threshold.

3 A fast and accurate adaptive solution strategy for two-scale models with continuous inter-scale dependencies

Abstract

This section presents a fast and accurate adaptive algorithm that numerically solves a two-scale model with continuous inter-scale dependencies. The considered sample two-scale model describes a phase transition of a binary mixture with the evolution of equiaxed dendritic microstructures. It consists of a macroscopic heat equation and a family of microscopic cell problems that model the phase transition of the mixture. Both scales are coupled: the macroscopic temperature field influences the evolution of the microstructure and the microscopic fields enter to the macroscopic heat equation via averaged coefficients.

Adaptivity exploits the constitutive assumption that the evolving microstructure depends in a continuous way on the macroscopic temperature field: macroscopic nodes with similar temperature evolutions use the same microscopic data. A suitable metric compares temperature evolutions and adaptive methods select active macroscopic nodes. Microscopic cell problems are solved for active nodes only; microscopic data in inactive nodes is approximated from microscopic data of active nodes with a similar temperature evolution. The set of active nodes is updated in course of the simulation: active nodes are deactivated until all active nodes have unsimilar temperature evolutions, and inactive nodes are activated until for every inactive node there exists at least one active node with a similar temperature evolution.

Numerical examples, in two and in three space dimensions, show that the adaptive solution is only slightly less accurate than the direct solution, but it is computationally much more efficient. Therefore, the adaptive algorithm enables the solution of two-scale models with continuous inter-scale dependencies on large computational macroscopic and microscopic grids within an acceptable period of time for computation.

3.1 Introduction

Many technically relevant processes exhibit a priori unknown microstructures that evolve in time. Important examples are solidification processes with dendritic and eutectic microstructures [16, 43], flow in porous media with changing pore geometry as a consequence of elastoplastic deformations and deposition or desorption of matter, and microstructures in epitaxial growth of thin solid layers [24]. Due to huge differences in relevant length and possibly also time scales, it is usually not feasible to simulate such processes by a direct numerical discretization of a full model. A much more promising approach is the usage of homogenization or averaging techniques, that were originally developed with the aim to find purely macroscopic models with suitable constitutive laws that model the properties of the microstructure [15, 32, 34]. The application of those methods to processes with evolution of a priori unknown microstructures typically leads to full two- or multi-scale models that combine differential equations on the smallest scales with homogenized differential equations on the macroscopic scales [19]. Both scales are coupled: the macroscopic fields influence the evolution of the microstructures, and the microscopic fields enter to the homogenized equations via averaged coefficients. A direct discretization of such a model typically requires the solution of a full microscopic cell problem for every node of

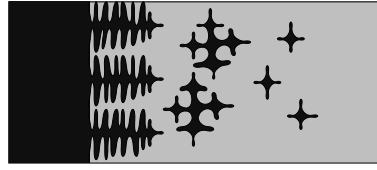


Figure 3.1: Columnar (on the left) and equiaxed dendritic structures, [22].

a macroscopic numerical grid. This leads to a huge numerical complexity and limits the application to problems with comparatively small macroscopic grids.

The aim of the Adaptive Strategy is to crack this limitation. It intends to solve only a small fraction, adaptively selected, of all the microscopic problems of the two-scale model. Fundamental to this strategy is the constitutive assumption that declares that the evolving microstructure depends in a continuous way on the macroscopic fields. Consequently, the key to an efficient algorithm is to reuse already computed data of microscopic problems for other microscopic problems with similar macroscopic data. This approach is different to existing methods for the efficient solution of multi-scale models, see e.g. [33, 56], insofar that this approach still solves full microscopic problems but tries to reduce their number as far as possible. It has some similarity to the method in [53], that uses a database approach for solidification processes: a directional/columnar solidification problem (see Figure 3.1) is studied, and the microscopic problems in the multi-scale model are replaced by simplified sample problems with prescribed temperature evolutions that are obtained by a global iterative procedure. Contrary to that, this section's Adaptive Strategy is mainly based on an efficient adaptive "online" selection of relatively few microscopic problems that are solved, "online" within one single solution of the two-scale model. This is in particular reasonable if the microscopic problems are comparatively hard to solve, as it is the case for the equiaxed dendritic growth problem (see Figure 3.1) to be discussed here.

The organization of this section is as follows: Subsection 3.2 briefly describes the two-scale model to be solved, Subsection 3.3 develops the Adaptive Strategy, and finally Subsection 3.4 presents numerical results, in two and also in three space dimensions, that show the efficiency and the accuracy of the Adaptive Strategy.

3.2 The considered two-scale model

Many solidification processes develop dendritic microstructures of equiaxed morphology. Equiaxed structures grow from small solid kernels that nucleate in an undercooled melt. During solidification these kernels develop dendritic instabilities, for more details see e.g. [43] or [16]. To control these instabilities, models for dendritic growth must account for curvature undercooling and possibly also kinetic undercooling. The phenomenologically simplest model is the Stefan problem with Gibbs-Thomson effect, [57]. In contrast to the Stefan problem, a phase field model approximates the sharp transition layer between the solid and the liquid phase by a diffuse phase transition region, [9, 36, 48]: the phase transition is described by a phase field ϕ , which smoothly varies from its liquid value ϕ_ℓ to its solid value ϕ_s .

The two-scale model is obtained by the application of a homogenization technique, under the assumption of fast heat diffusion and slow solute diffusion, to a phase transition model describing a solidification process of a binary mixture (a large Lewis number, that

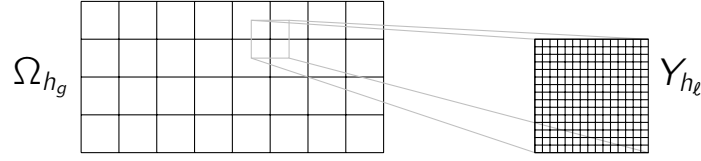


Figure 3.2: The macroscopic Ω_{h_g} and the local microscopic grid Y_{h_l} .

is a large ratio of thermal to solutal diffusivity, is typical of mixtures). The model consists of a macroscopic homogenized heat equation, and for each point of the macroscopic domain of a microscopic cell problem with periodic boundary conditions. For details on the homogenization see [20, 21, 23] or the brief recapitulation in Section 2.

3.2.1 The macroscopic homogenized heat equation

The macroscopic heat equation in dimensionless form reads

$$\partial_t T = K \Delta_x T + \frac{1}{2} \partial_t \overline{\phi}^Y. \quad (3.1)$$

It must be solved for the macroscopic temperature field $T = T(t, x)$ in the macroscopic time-space cylinder $Q_{I_{t_{\text{end}}}\Omega} = I_{t_{\text{end}}} \times \Omega$ consisting of the time interval $I_{t_{\text{end}}} = [0, t_{\text{end}}]$ and the macroscopic domain $\Omega \subset \mathbb{R}^N$ for space dimension $N \in \{2, 3\}$. The averaged phase field

$$\overline{\phi(t, x)}^Y = \frac{1}{|Y|} \int_Y \phi(t, x, y) dy \quad (3.2)$$

depends on the microscopic cell problem in macroscopic point x . Consequently, $\frac{1}{2} \partial_t \overline{\phi(t, x)}^Y$ describes the averaged latent heat that is released during the phase transition from liquid to solid in the microscopic cell problem of $x \in \Omega$. Parameter K describes the heat conductivity, which is independent of the phase field. The macroscopic equation is supplemented by a Neumann boundary condition and an initial temperature condition $T(0, x) = T_0(x)$ for all $x \in \Omega$.

3.2.2 The microscopic cell problems

The microscopic cell problems describe the liquid-solid phase transition for a binary mixture depending on a temperature T that is taken from the solution of the macroscopic problem. The governing equations in dimensionless form are

$$\begin{aligned} \frac{1+k}{2} \partial_t U = & \frac{1}{2} \partial_t (\phi [1 + (1-k)U]) + \\ & + \nabla_y \cdot \left(\lambda a_2 \frac{W_0^2}{\tau_0} \frac{1-\phi}{2} \nabla_y U + \frac{W_0 A(\hat{n})}{2\sqrt{2}} [1 + (1-k)U] \partial_t \phi \frac{\nabla_y \phi}{|\nabla_y \phi|} \right), \end{aligned} \quad (3.3)$$

$$\begin{aligned} \tau \partial_t \phi = & \phi - \phi^3 - \lambda (1 - \phi^2)^2 (T + M c_\infty U) + W_0^2 \nabla_y \cdot (A(\hat{n})^2 \nabla_y \phi) + \\ & + W_0^2 \sum_{j=1}^N \partial_{y_j} \left(\frac{|\nabla_y \phi|^2}{2} \frac{\partial A(\hat{n})^2}{\partial (\partial_{y_j} \phi)} \right). \end{aligned} \quad (3.4)$$

The microscopic problem in macroscopic point $x \in \Omega$ must be solved for the microscopic chemical potential $U = U(t, x, y)$ and the microscopic phase field $\phi = \phi(t, x, y)$ on the time-space cylinder $Q_{I_{t_{\text{end}}}\times Y} = I_{t_{\text{end}}} \times \{x\} \times Y$, see Figure 3.2. It depends on the the

macroscopic temperature $T = T(t, x)$. Phase field ϕ varies smoothly from its liquid value $\phi_\ell = -1$ to its solid value $\phi_s = 1$. The initial conditions $U_0(y)$ for the chemical potential and $\phi_0(y)$ for the phase field are independent of the macroscopic grid point. The equations are supplemented with Y -periodic boundary conditions for U and ϕ . The domain Y is an interval in \mathbb{R}^N , $N \in \{2, 3\}$.

The equations (3.3) and (3.4) are introduced in [36, 48]. Their model is physically more realistic than the phase field model in [21]. The authors of [36, 48] study the issue of length scales, in particular the width of the phase transition region. They present results that illustrate the utility of their model for simulating dendritic solidification for large ratios of the thermal to the solutal diffusivity. Here, their model is extended to the described two-scale model. The numerical examples in Subsection 3.4 depend on the physical parameters proposed in [48]: $k = 0.15$, $\lambda = 3.1913$, $a_2 = 0.6267$ and $Mc_\infty = 0.5325$. The microscopic thermal diffusivity is assumed to be infinitely large, such that τ reduces to $\tau = \tau_0 A(\hat{n})^2 Mc_\infty (1 + (1 - k)U)$, [48]. The numerical discretization scales out the measure W_0 of the interface width and the relaxation time τ_0 , see Subsection 3.2.3. Function

$$A(\hat{n}) = 1 - \epsilon(3 - 4|\hat{n}|_4^4), \quad \hat{n} = -\frac{\nabla_y \phi}{|\nabla_y \phi|}, \quad (3.5)$$

triggers the dendritic growth, depending on the outward normal \hat{n} to the solid phase and the strength $\epsilon > 0$ of the anisotropy, [37]. Function $A(\hat{n})$ yields four favored directions of dendritic growth in two space dimensions and six in three. The dendrites grow along the principal directions e_j , $j = 1, \dots, N$, where e_j is the j -th unit vector of \mathbb{R}^N . In the numerical examples, parameter $\epsilon = 0.02$ is used in two space dimensions and $\epsilon = 0.04$ in three.

The two-scale model does not include stochastic perturbations (noise) in the equations for the chemical potential. Such perturbations are used to trigger the sidebranching into dendrites of second and higher order. Therefore, the numerical results will only show primary dendrites. In fact the model is intended as a "simple" model case for the Adaptive Strategy. The applicability of the strategy to models with stochastic perturbations is discussed in Subsection 3.5.

3.2.3 Discretization of the two-scale model

The macroscopic as well as the microscopic problems are discretized by explicit finite difference methods with respect to the time on a uniform partition $I_{t_{\text{end}}, k_t} = \{t_n \in I_{t_{\text{end}}} \mid t_n = nk_t, n = 0, \dots, N, N = \frac{t_{\text{end}}}{k_t}\}$ of the time interval with time-step size $k_t = 0.018\tau_0$, [48]. With respect to the space standard second-order finite differences are used on uniform rectangular grids Ω_{h_g} and Y_{h_ℓ} , where $h_g = c_g h_\ell$ is the macroscopic and $h_\ell = 0.4W_0$ the microscopic mesh-size, [48]. As in reference [37], a nine-point isotropic stencil in two space dimensions and a 19-point isotropic stencil in three dimensions, [46], discretizes $\nabla_y \cdot (A(\hat{n})^2 \nabla_y \phi)$. The macroscopic heat conductivity is $K = K_0 \frac{W_0^2}{\tau_0}$. These specifications scale out the measure W_0 of the interface width and the relaxation time τ_0 . The factor K_0 of the macroscopic heat conductivity, the final time t_{end} , the domains Ω_{h_g} and Y_{h_ℓ} , and the boundary condition for the macroscopic temperature are specified in the numerical examples subsection.

The time discretization decouples the macroscopic and the microscopic problems: at first, in each time step, all (active) microscopic problems are solved (at first the phase field equation is solved and afterwards the equation for the chemical potential) with temperature values taken from the previous time step, then the macroscopic problem is solved.

3.3 The adaptive solution strategy

Aim of the Adaptive Strategy is to solve the two-scale model efficiently: this means on the one hand to considerably reduce the number of cell problems that are computed, but on the other to obtain an accurate solution anyway. Background of the Adaptive Strategy is the constitutive assumption that microstructures evolving at similar macroscopic conditions, given by similar evolutions of the macroscopic fields, develop similar features. Consequently, already computed data of a microstructure evolution in a certain macroscopic node may also be used as the data in another macroscopic node with a similar temperature evolution. A suitable metric $d_E(T_1, T_2)$ compares the evolutions of two temperatures T_1 and T_2 , and a tolerance limits the distance d_E of similar temperature evolutions. Macroscopic nodes whose microscopic cell problems are solved are called *active nodes*; the remaining nodes are called *inactive*. Initially, only one macroscopic node is active. $N_A(t_n)$ denotes the set of active nodes at time $t_n = nk_t$. It is constructed by adding nodes to and removing nodes from the previous set of active nodes $N_A(t_{n-1})$. This is done according to the following steps:

1. The *First Refining Routine* ensures that the macroscopic nodes with “highest” and “lowest” temperature evolutions are active.
2. The *Coarsening Routine* successively *deactivates* (removes active nodes from N_A) active nodes whose temperature evolutions are *very* similar to that of another active node. This step is crucial to reduce the number of active nodes and thereby the required numerical effort.
3. The *Second Refining Routine* successively *activates* (adds inactive nodes to N_A) inactive nodes that do not possess at least one active node with a similar temperature evolution. This step is crucial to ensure a good approximation of the two-scale model's solution.

The routine that approximates microscopic data in inactive nodes is subdivided into two parts: transfer of data and type of approximation. The Adaptive Strategy provides two methods to transfer microscopic data from active to inactive macroscopic nodes:

1. The *Interpolation Transfer Method* interpolates the data of several or all active nodes.
2. The *Single Transfer Method* uses only the data of the active node with the most similar temperature evolution.

Moreover, the Adaptive Strategy provides two different methods to approximate the discrete release of latent heat $(\overline{\Phi(t_n, x)}^Y - \overline{\Phi(t_{n-1}, x)}^Y)/k_t$ in inactive nodes x :

1. The *Complete Approximation Method* approximates $\overline{\Phi(t_n, x)}^Y$ and $\overline{\Phi(t_{n-1}, x)}^Y$ by the microscopic data transferred from the same active nodes by a Transfer Method for time t_n .
2. The *Separate Approximation Method* approximates $\overline{\Phi(t_n, x)}^Y$ by a Transfer Method for time t_n , and $\overline{\Phi(t_{n-1}, x)}^Y$ by the same Transfer Method for time t_{n-1} .

The following subsections describe the Adaptive Strategy in detail.

3.3.1 Comparison of macroscopic temperature evolutions

A fundamental part of the Adaptive Strategy is the distinction between similar and unsimilar temperature evolutions. This distinction depends firstly on the distance of the temperature evolutions, and secondly on the tolerance that defines an upper bound for the distance of similar temperature evolutions. What is needed in order to measure a distance of two temperature evolutions, is a suitable metric that takes history into account. Typically, such a metric has the form

$$d_E(T_1, T_2; t) = d_E(T_1, T_2; t, \lambda, \tau) := \left(\int_0^t w(t-s; \lambda)^\tau |(T_1 - T_2)(s)|^\tau ds \right)^{1/\tau}, \quad (3.6)$$

with a suitable weight function w , e.g.

$$w(t-s; \lambda) := e^{-\lambda(t-s)} \text{ with a History Parameter } \lambda \geq 0. \quad (3.7)$$

The History Parameter λ determines the significance of a value of the difference $|T_1 - T_2|$ in the past: if λ is large, then only the values of $|T_1 - T_2|$ in the recent past of t are relevant. In other words, if $\lambda > 0$ then the metric is equipped with a fading memory; the larger the History Parameter the faster the memory fades. An advantage of d_E is the possibility to compute its values recursively:

$$\begin{aligned} & d_E(T_1, T_2; (n+1)k_t) \\ &= \left(e^{-\lambda\tau k_t} d_E(T_1, T_2; nk_t)^\tau + \int_0^{k_t} e^{-\lambda\tau(k_t-s)} |(T_1 - T_2)(nk_t + s)|^\tau ds \right)^{1/\tau}. \end{aligned} \quad (3.8)$$

In the numerical examples, Formula (3.8) is used with the approximation

$$\int_0^{k_t} e^{-\lambda\tau(k_t-s)} |(T_1 - T_2)(nk_t + s)|^\tau ds \approx k_t |(T_1 - T_2)(nk_t)|^\tau. \quad (3.9)$$

Corollary 2.7 shows that a certain multiple of the distance of two temperature evolutions measured in this weighted L_τ -norm defines an upper-bound for the distance of the two corresponding evolving microstructures measured in the L_2 -norm in the microscopic domain. Of course, this relation is valid only for the simple model considered in Section 2, but nevertheless the numerical results show that the strategy works well with this metric.

Some useful definitions. Say T_{x_1} is the temperature evolution in macroscopic node x_1 and T_{x_2} in x_2 . T_{x_1} and T_{x_2} are called *similar (at time t with tolerance $\text{tol}(t)$)* if their distance $d_E(T_{x_1}, T_{x_2}; t)$ is not larger than $\text{tol}(t)$. On the contrary, T_{x_1} and T_{x_2} are called *different* in case that they are not similar. Furthermore, if, in comparison to all temperature evolutions, T_{x_1} is the temperature evolution with the smallest (largest) distance to T_{x_2} , then T_{x_1} is called *most similar to (most different to) T_{x_2}* . The same relations as for their temperature evolutions also hold for the macroscopic nodes x_1 and x_2 : for instance, x_1 and x_2 are called *similar* if and only if their temperature evolutions T_{x_1} and T_{x_2} are similar.

What is of special interest are the two following types of relations between macroscopic nodes: active to inactive, and active to active. On the one hand, if all active nodes are different to an inactive node, then the inactive node is activated; on the other hand, if a pair of similar active nodes exists, then one of them is deactivated. In order to avoid a permanent update of N_A , it is wise to use a smaller tolerance for the relation of two active nodes than for the relation of inactive to active nodes. Therefore, the *Refining Tolerance*

tol_r defines the upper bound for the distance of similar temperature evolutions of an inactive and an active node, and the *Coarsening Tolerance* tol_c defines the upper bound for the distance of similar temperature evolutions of active nodes. In order to scale appropriately, tol_r depends on the distance of the two most different temperature evolutions on the (whole) macroscopic grid: a possible choice is $c_{\text{tol}_r,1} \cdot \max_{x,\bar{x} \in \Omega_{hg}} \{d_E(T_x, T_{\bar{x}}; t_n)\}$, where parameter $0 \leq c_{\text{tol}_r,1} \leq 1$ influences the number of active nodes. Because the refining tolerance tol_r gives an upper bound for the distance between the temperature evolutions of an inactive node and a similar active node, and because of possible error propagation with increasing time, it may be plausible to increase tol_r relatively with increasing time. Consequently, with $c_{\text{tol}_r,0} \geq 0$ and $0 \leq c_{\text{tol}_r,1} \leq 1$, Refining Tolerance tol_r is defined as

$$\text{tol}_r(t) := \left(1 + c_{\text{tol}_r,0} \cdot \frac{t}{t_{\text{end}}}\right) \cdot c_{\text{tol}_r,1} \cdot \max_{x,\bar{x} \in \Omega_{hg}} \{d_E(T_x, T_{\bar{x}}; t)\}. \quad (3.10)$$

The Coarsening Tolerance $\text{tol}_c(t)$ is defined as a fraction of the Refining Tolerance:

$$\text{tol}_c(t) := c_{\text{tol}_c} \cdot \text{tol}_r(t) \text{ with } 0 \leq c_{\text{tol}_c} < 1. \quad (3.11)$$

3.3.2 The first refining routine

The farther below the solidification point a temperature evolves, the quicker proceeds the solidification in the corresponding microstructure. Therefore, the First Refining Routine ensures that the set of active nodes $N_A(t_n)$ contains macroscopic nodes with the "highest" and the "lowest" temperature evolution. The artificial temperature evolutions

$$T_{\max}(t_n) := \max_{x \in \Omega_{hg}} T_x(t_n) \text{ and } T_{\min}(t_n) := \min_{x \in \Omega_{hg}} T_x(t_n) \quad (3.12)$$

help to define the sets $\Omega_{T_{\max}}(t_n)$ and $\Omega_{T_{\min}}(t_n)$ of such macroscopic nodes:

$$\begin{aligned} \Omega_{T_{\max}}(t_n) &:= \arg \min_{x \in \Omega_{hg}} \{d_E(T_x, T_{\max}; t_n)\}, \\ \Omega_{T_{\min}}(t_n) &:= \arg \min_{x \in \Omega_{hg}} \{d_E(T_x, T_{\min}; t_n)\}. \end{aligned} \quad (3.13)$$

In order to avoid a permanent update of N_A , an inactive node $x^i \in \Omega_{T_{\max}}(t_n) \cup \Omega_{T_{\min}}(t_n)$ is activated only if x^i is different to all active nodes with tolerance $c_{\text{tol}_e} \cdot \text{tol}_r(t_n)$:

$$d_E(T_{x^i}, T_{x^a}; t_n) > c_{\text{tol}_e} \cdot \text{tol}_r(t_n) \quad \forall x^a \in N_A(t_n) \text{ with } c_{\text{tol}_e} \geq 0. \quad (3.14)$$

In case there is more than one inactive node in $\Omega_{T_{\max}}(t_n) \cup \Omega_{T_{\min}}(t_n)$ that fulfills condition (3.14), then the nodes to be activated are chosen with respect to the selection criteria of the Second Refining Routine. Please note that the First Refining Routine adds at most two inactive nodes to the set of active nodes.

3.3.3 The coarsening routine

The Coarsening Routine ensures that active nodes are not similar to each other. In other words, the Coarsening Routine avoids the calculation of similar microscopic problems. At first, all similar active nodes are collected in $M^c(t_n)$, the set of active nodes that may be deactivated. Then, until $M^c(t_n)$ is empty, nodes $x^c \in M^c(t_n)$ are successively deactivated, that is x^c is removed from the set of active nodes as well as from $M^c(t_n)$; moreover, all

nodes of $M^c(t_n)$ that (after the deactivation of $x^c \in M^c(t_n)$) are different to all the other active nodes, all those nodes are also removed from $M^c(t_n)$. All the active nodes are different to each other if and only if the set $M^c(t_n)$ is empty. A node $x^c \in M^c(t_n)$ to be deactivated is selected either randomly or with respect to the following criteria. The first criterion

$$x^c \notin M_0^c(t_n) := M^c(t_n) \cap \{\arg \min_{x \in N_A(t_n)} \{d_E(T_x, T_{\max}; t_n)\} \cup \arg \min_{x \in N_A(t_n)} \{d_E(T_x, T_{\min}; t_n)\}\}, \quad (3.15)$$

ensures that neither an active macroscopic node with the highest nor an active node with the lowest temperature evolution is deactivated.

The second criterion

$$x^c \in M_1^c(t_n) := \arg \min_{x \in M^c(t_n) \setminus M_0^c(t_n)} \{d_E(T_x, T_{\hat{x}^c(x, t_n)}; t_n)\}, \quad (3.16)$$

with the set $N_A^x(t_n) := \{x^a \in N_A(t_n) \mid d_E(T_x, T_{x^a}; t_n) > \text{tol}_c(t_n)\}$ containing all different active nodes to x , and with the first element $\hat{x}^c(x, t_n)$ of $\arg \min_{\hat{x} \in N_A^x(t_n)} \{d_E(T_x, T_{\hat{x}}; t_n)\}$, guarantees that the remaining active nodes are more different (concerning the distance of temperature evolutions) from their most similar active node than the one which is deactivated.

The third criterion

$$x^c \in M_2^c(t_n) := \arg \min_{x \in M_1^c(t_n)} \{|x - \hat{x}^c(x, t_n)|\}. \quad (3.17)$$

effects that the remaining active nodes are farther away (concerning Euclidean distance on the macroscopic domain) from their most similar active node than the one that is deactivated. Finally, the first element of $M_2^c(t_n)$ is deactivated.

As mentioned above, another possibility is random coarsening: if the First Refining Routine is executed, then a randomly chosen active node of $M^c(t_n) \setminus M_0^c(t_n)$ is deactivated; otherwise, a randomly chosen active node of $M^c(t_n)$ is deactivated.

3.3.4 The second refining routine

The Second Refining Routine ensures that for every inactive node there exists at least one similar active node. In other words, it ensures that the approximated microscopic data in inactive nodes is accurate. At first, all inactive nodes without a similar active node are collected in the set $M^r(t_n)$. Then, until $M^r(t_n)$ is empty, inactive nodes $x^r \in M^r(t_n)$ are successively activated, that is x^r is added to $N_A(t_n)$ and removed from $M^r(t_n)$; moreover, all nodes of $M^r(t_n)$ that are similar to x^r are also removed from $M^r(t_n)$. There is a similar active node to every inactive node if and only if the set $M^r(t_n)$ is empty. A node $x^r \in M^r(t_n)$ to be activated is selected either, as in the Coarsening Routine, randomly or with respect to the following criteria. The first criterion

$$x^r \in M_1^r(t_n) := \arg \max_{x \in M^r(t_n)} \{d_E(T_x, T_{\hat{x}^a(x, t_n)}; t_n)\}, \quad (3.18)$$

with the first element $\hat{x}^a(x, t_n)$ of $\arg \min_{x^a \in N_A(t_n)} \{d_E(T_{x^a}, T_x; t_n)\}$ (that is $\hat{x}^a(x, t_n)$ is one of the most similar active nodes to x), implies that x^r is one of the elements of $M^r(t_n)$ that differ most from their respective most similar active node (concerning the distance of temperature evolutions).

The second criterion

$$x^r \in M_2^r(t_n) := \arg \max_{x \in M_1^r(t_n)} \{|x - \hat{x}^a(x, t_n)|\} \quad (3.19)$$

ensures that x^r is one of the elements of $M_1^r(t_n)$ that are farthest away (concerning Euclidean distance) from their respective most similar active node; thus, this criterion ensures that the most similar active nodes are geometrically well distributed in order to avoid agglomerations of them. Finally, the first inactive node of $M_2^r(t_n)$ is activated.

Another possibility, as in the Coarsening Routine, is random refining: a randomly chosen element of $M^r(t_n)$ is activated.

3.3.5 "New" microscopic initial conditions in newly activated macroscopic nodes

What is needed for the future solution of the microscopic problem of a newly activated macroscopic node are accurate initial conditions. The Adaptive Strategy provides two methods to gain those *new* initial conditions. The first method, the *Retrospective Method*, computes the new initial conditions retrospectively: it solves the microscopic problem, depending on the temperature evolution in the newly activated node, from initial time until the time of activation minus one time-step. This method requires the knowledge of the whole history of the temperature field for every macroscopic node. Since this needs a lot of memory, the method provides the possibility to store these data with a larger time increment than k_t and to determine the data for the relevant numerical points in time by linear interpolation. The second method, the *Copy Method*, that is considerably easier to code efficiently than the Retrospective Method, approximates the new initial data by the microscopic data of the active macroscopic node with the most similar temperature evolution: it simply copies the current microscopic data of the most similar active node to the newly activated node. On the one hand, it is the Copy Method that is implemented easily, but on the other hand, it is the Retrospective Method that is most likely to produce the more accurate results.

3.3.6 Approximation of the latent heat released in inactive macroscopic nodes

The latent heat released $(\overline{\Phi(t_n, x^i)} - \overline{\Phi(t_{n-1}, x^i)})/k_t$ in inactive macroscopic nodes x^i must be approximated. The approximation routine is subdivided into two parts: transfer of data and type of approximation.

The Adaptive Strategy provides two methods for the transfer of data from active to inactive nodes: *Single Transfer* (abbr.: ST) and *Interpolation Transfer* (IT), see Figure 3.3. The Single Transfer Method simply copies to an inactive node the microscopic data of the most similar active node. On the contrary, the Interpolation Transfer Method interpolates an inactive node's data between the data of several or all active nodes. Say $A_{x^i}(t_n) \subseteq N_A(t_n)$ is the subset of all the active nodes that in time-step n contribute to the interpolation of data in the inactive node x^i , and say $\hat{x}^a(x^i, t_n)$ is the most similar active node to x^i at time t_n . Common sense advises to correlate the weights of the contributions to the distances of the temperature evolutions: the more similar an active node is to an inactive node, the higher the weight of the active node's contribution; consequently, the *weight* $w_{x^i}(t_n, x^a)$ of the contribution of $x^a \in A_{x^i}(t_n)$ at time t_n to the interpolation of

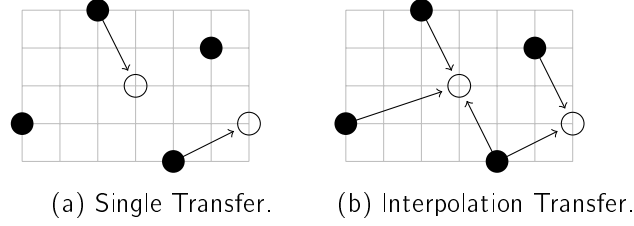


Figure 3.3: Approximation of microscopic data in inactive nodes: the Single in (a) and the Interpolation Transfer Method in (b). Filled circles indicate active nodes, unfilled circles represent inactive nodes, and a vector displays if an active node contributes to the approximation of data in an inactive node.

microscopic data in the inactive node x^i is defined as follows

$$\begin{aligned}
 w_{x^i}(t_n, x^a) &= \left(\sum_{\tilde{x}^a \in A_{x^i}(t_n)} \tilde{w}_{x^i}(t_n, \tilde{x}^a) \right)^{-1} \tilde{w}_{x^i}(t_n, x^a), \\
 \tilde{w}_{x^i}(t_n, x^a) &= \begin{cases} 1, & x^a = \hat{x}^a(x^i, t_n), \\ (d_E(T_{x^i}, T_{x^a}; t_n))^{-1} d_E(T_{x^i}, T_{\hat{x}^a(x^i, t_n)}; t_n), & x^a \neq \hat{x}^a(x^i, t_n). \end{cases} \quad (3.20)
 \end{aligned}$$

The intention of the interpolation is to minimize possible under- or overestimations of the latent heat released in inactive nodes. This may be achieved by the so called *Equality Condition*. This condition is a constriction to the set $A_{x^i}(t_n)$. It requires that the half of all active nodes $x^a \in A_{x^i}(t_n)$ have temperature evolutions *higher* and the other half *lower* temperature evolutions than the temperature evolution of x^i . By definition, temperature evolution T_1 is *higher* (*lower*) than T_2 if and only if T_1 has a smaller distance to T_{\max} (T_{\min}) (of (3.12)) than T_2 . Say there are m_h active nodes with a higher and m_ℓ active nodes with a lower temperature evolution than inactive node x^i , then the Equality Condition constructs $A_{x^i}(t_n)$ as follows: in case of $m_h = m_\ell$ every active node is contained in $A_{x^i}(t_n)$; if $m_h > m_\ell \geq 1$ then $A_{x^i}(t_n)$ contains every active node with a lower temperature evolution but only the m_ℓ most similar active nodes with a higher temperature evolution, it is vice versa in case of $m_\ell > m_h \geq 1$; if there are only active nodes with either higher or lower temperature evolutions, then $A_{x^i}(t_n)$ only contains the most similar active node $\hat{x}^a(x^i, t_n)$. Furthermore, the Adaptive Strategy provides the possibility to limit the maximum number M_A of active nodes that contribute to the interpolation of data in inactive nodes. If the Equality Condition is invalid and in case that $M_A < |N_A(t_n)|$ then $A_{x^i}(t_n)$ simply contains the M_A most similar active nodes. Otherwise, if the Equality Condition is valid and $M_A < |N_A(t_n)|$ then $A_{x^i}(t_n)$ is chosen not from all the active nodes but from the subset that only contains the $\min(m_h, \lfloor \frac{M_A}{2} \rfloor)$ most similar active nodes with a higher and the $\min(m_\ell, \lfloor \frac{M_A}{2} \rfloor)$ most similar active nodes with a lower temperature evolution than x^i .

There are two types of approximation methods of the latent heat released: *complete* and *separate*. Say $\overline{\phi_x^n}^Y := \overline{\phi(t_n, x)}^Y$ for all $n = 1, \dots, N$ and for all $x \in \Omega_{h_g}$. The *Complete Approximation Method* (abbr.: CA) interpolates, in case of the Interpolation Transfer Method, the latent heat released in inactive nodes between the latent heat released of all active nodes contained in $A_{x^i}(t_n)$,

$$\text{IT-CA: } \overline{\phi_{x^i}^n}^Y - \overline{\phi_{x^i}^{n-1}}^Y \approx \sum_{x^a \in A_{x^i}(t_n)} w_{x^i}(t_n, x^a) \left(\overline{\phi_{x^a}^n}^Y - \overline{\phi_{x^a}^{n-1}}^Y \right). \quad (3.21)$$

In case of the Single Transfer Method (3.21) becomes

$$\text{ST-CA: } \overline{\phi_{x^i}^n}^Y - \overline{\phi_{x^i}^{n-1}}^Y \approx \overline{\phi_{\hat{x}^a(x^i, t_n)}^n}^Y - \overline{\phi_{\hat{x}^a(x^i, t_n)}^{n-1}}^Y. \quad (3.22)$$

On the contrary, the *Separate Approximation Method* (abbr.: SA) interpolates, in case of the Interpolation Transfer Method, separately each microscopic phase average $\overline{\phi_{x^i}^m}^Y$, $m = n - 1, n$, between the phase averages $\overline{\phi_{x^a}^m}^Y$ of the contributing active nodes $x^a \in A_{x^i}(t_m)$ at time t_m ,

$$\text{IT-SA: } \overline{\phi_{x^i}^n}^Y - \overline{\phi_{x^i}^{n-1}}^Y \approx \sum_{x^a \in A_{x^i}(t_n)} w_{x^i}(t_n, x^a) \overline{\phi_{x^a}^n}^Y - \sum_{x^a \in A_{x^i}(t_{n-1})} w_{x^i}(t_{n-1}, x^a) \overline{\phi_{x^a}^{n-1}}^Y. \quad (3.23)$$

In case of the Single Transfer Method (3.23) becomes

$$\text{ST-SA: } \overline{\phi_{x^i}^n}^Y - \overline{\phi_{x^i}^{n-1}}^Y \approx \overline{\phi_{\hat{x}^a(x^i, t_n)}^n}^Y - \overline{\phi_{\hat{x}^a(x^i, t_{n-1})}^{n-1}}^Y. \quad (3.24)$$

3.3.7 Algorithm of the adaptive strategy in time-step $n = 1, \dots, N$

1. Update the distances of the temperature evolutions.
2. Update the set of active nodes $N_A(t_n)$: First Refining, Coarsening, and Second Refining Routine.
3. Solve the microscopic problems of the active macroscopic nodes.
4. Approximate the latent heat released.
5. Solve the macroscopic problem.

3.4 Numerical results

In order to evaluate the Adaptive Strategy's quality, this subsection presents the results of numerical computations. The Adaptive Strategy solves the two-scale model in two and in three space dimensions. In two space dimensions, the set of parameters and the methods of the Adaptive Strategy are opted for, and, afterwards, it is demonstrated that for the refining tolerance tending to zero the adaptive solution converges to the direct solution; solving the two-scale problem directly means, in contrast to solving it adaptively, to solve the microscopic problem of every macroscopic node. Convergence is also demonstrated in three space dimensions. Finally, the Adaptive Strategy solves the two-scale model on a very large three-dimensional macroscopic grid; obtaining the corresponding direct solution would, because every microscopic problem must be solved, require enormous computing and memory resources.

An adaptive solution's accuracy is estimated by comparing its macroscopic temperature solution T_{adaptive} to the direct method's temperature solution T_{direct} . The error $\Delta T := |T_{\text{direct}} - T_{\text{adaptive}}|$ is measured in the discrete L_2 -norm and the discrete L_∞ -norm. These norms can be taken for the discrete macroscopic space domain Ω_{h_g} , or, with the discrete time-interval $I_{t_{\text{end}}, k_t} = \{t_n = n \cdot k_t \mid 0 \leq n \leq N, N \cdot k_t = t_{\text{end}}\}$, for the whole discrete

time-space cylinder $Q_{k_t, h_g} = I_{t_{\text{end}}, k_t} \times \Omega_{h_g}$:

$$\begin{aligned} \|\Delta T(t_n, \cdot)\|_{\Omega, 2} &= \sqrt{\frac{1}{|\Omega_{h_g}|} \sum_{x \in \Omega_{h_g}} |\Delta T(t_n, x)|^2}, \\ \|\Delta T(\cdot, \cdot)\|_{Q, 2} &= \sqrt{\frac{1}{N+1} \sum_{n=0}^N \|\Delta T(t_n, \cdot)\|_{\Omega, 2}^2}, \\ \|\Delta T(t_n, \cdot)\|_{\Omega, \infty} &= \max_{x \in \Omega_{h_g}} |\Delta T(t_n, x)|, \\ \|\Delta T(\cdot, \cdot)\|_{Q, \infty} &= \max_{n=0, \dots, N} \|\Delta T(t_n, \cdot)\|_{\Omega, \infty}. \end{aligned} \quad (3.25)$$

3.4.1 Numerical results in two space dimensions

The two-scale model to be solved in two space dimensions is given by the microscopic problem (3.3) and (3.4) on the microscopic domain $Y_{h_\ell} = [0, 1600h_\ell]^2$ with space increment $h_\ell = 0.4W_0$, and by the macroscopic heat equation (3.1) on the macroscopic domain $\Omega_{h_g} = [0, 39h_g] \times [0, 19h_g]$ with $h_g = 1600h_\ell$. Therefore, Ω_{h_g} consists of 800 nodes, each of them governing one microscopic problem on Y_{h_ℓ} consisting of 1601^2 nodes. The computation time is from 0 to $10^5 k_t$ with time increment $k_t = 0.018\tau_0$. On the macroscopic scale, the effective heat conductivity K_0 is chosen as 32000, and the boundary conditions of the heat equation are the prescribed heat fluxes:

$$\nabla T \cdot n = \begin{cases} -3 \cdot 10^{-5} \cdot \frac{0.4 \cdot 1600}{0.018} \cdot \frac{1}{32000} & \text{for } x_1 = 0, \\ -1.5 \cdot 10^{-5} \cdot \frac{0.4 \cdot 1600}{0.018} \cdot \frac{1}{32000} & \text{for } x_2 = 0, \\ 0 & \text{otherwise.} \end{cases} \quad (3.26)$$

Put more simply, two parts of the boundary have cooling conditions, and the remaining two parts are isolated. For the microscopic cell problems the boundary conditions are periodic. The initial temperature T , the initial chemical potential U and the initial phase field ϕ are specified for all $x \in \Omega_{h_g}$ and all $y \in Y_{h_\ell}$ as

$$\begin{aligned} T(0, x) &= -0.3, \\ U(0, x, y) &= 0, \\ \phi(0, x, y) &= \tanh\left(-0.3 \left(\left\lfloor \frac{1}{h_\ell} y - (800 \ 800)^\top \right\rfloor - 5\right)\right). \end{aligned} \quad (3.27)$$

By reason that the initial conditions of the microscopic unknowns U and ϕ are independent of the macroscopic node x , they are equal for all the microscopic problems. Furthermore, they (in combination with the initial temperature condition) imply that, initially, a small solid kernel occupies the center of every microscopic domain and that each kernel is surrounded by an undercooled melt.

Figure 3.4 presents the two-scale model's direct solution. Solving the two-scale model directly becomes very costly for large macroscopic grids, therefore the global grid is chosen to be rather small. What is interesting to note in Figure 3.4 is that the fastest solidification takes place in the microscopic problem of the macroscopic node $(0, 0)^\top$. This is due to the fact, caused by the boundary condition on the macroscopic domain, that in every time-step macroscopic node $(0, 0)^\top$ records the lowest temperature. In contrast, since macroscopic node $(39, 19)^\top$ always records the highest temperature, this node's microscopic problem produces the smallest dendrite.

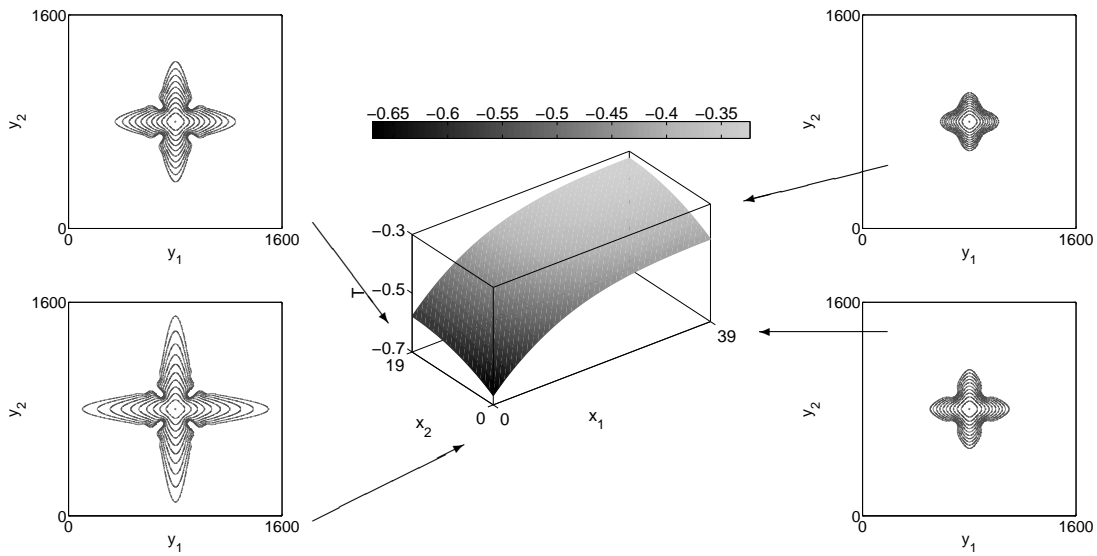


Figure 3.4: Direct solution of the two-scale model in two space dimensions. The figure in central position depicts the macroscopic temperature field at final time. The remaining figures present the evolution of the dendritic crystals in the microscopic problems of the corner nodes of the macroscopic grid. The crystals evolve from small initial solid kernels in the center of the microscopic domains. Their current states (the contour of $\phi = 0$) are displayed every 10000 time steps.

3.4.1.1 Optimization of the adaptive strategy for $c_{\text{tol},1} = 0.1$

The Adaptive Strategy depends on the History Parameter λ and the norm parameter τ in the metric that measures the difference of temperature evolutions, on the tolerances for the refining and the coarsening routines, and on the initial set of active nodes $N_A(0)$. In the computations to be presented, $N_A(0)$ consists of one node only. Moreover, the Adaptive Strategy provides different methods to transfer data from active to inactive nodes (Single (abbr.: ST) and Interpolation (IT) Transfer Method), and to compute the latent heat released in inactive nodes (Complete (CA) and Separate (SA) Approximation Method). The IT-methods for the transfer of data depend on the set of active nodes that contribute to the interpolation. Furthermore, the Adaptive Strategy depends on the method that approximates initial conditions for newly activated nodes. Inactive nodes to be activated or active nodes to be deactivated are either chosen randomly or according to the selection criteria presented above. This subsection explores these dependencies and tries to optimize the Adaptive Strategy, that is to discover the parameters and methods that result in the most accurate solution.

Unless definitions are explicitly given, the parameters and the methods of the Adaptive Strategy are prescribed as follows: method IT-CA approximates the latent heat released in inactive nodes, the set $A_{x^i}(t_n)$ of active nodes that contribute to the interpolation of data of the inactive node x^i is chosen with respect to the Equality Condition, at most two active nodes contribute to an interpolation (that is $M_A = 2$); parameters: $\lambda = 0.1$ and $\tau = 1$ in (3.6), $c_{\text{tol},0} = 0$ and $c_{\text{tol},1} = 0.1$ in Refining Tolerance tol_r , (3.10), $c_{\text{tol}_c} = 0.2$ in Coarsening Tolerance tol_c , (3.11), $c_{\text{tol}_e} = 0.01$ in the tolerance (3.14) for activating the nodes with the highest or the lowest temperature evolution; the set of active

λ	$\ \Delta T\ _{Q,\infty}$	$\overline{\ \Delta T\ _{\Omega,\infty}}$	$\overline{\ \Delta T\ _{\Omega,\infty}}^\sigma$	$\ \Delta T\ _{Q,2}$	$\overline{\ \Delta T\ _{\Omega,2}}$	$\overline{\ \Delta T\ _{\Omega,2}}^\sigma$	$\overline{ N_A }$	$\overline{ N_A }^\sigma$
10000	2.96e-4	1.27e-4	1.06e-4	4.62e-5	3.58e-5	2.92e-5	11.58	1.39
10	2.96e-4	1.27e-4	1.06e-4	4.62e-5	3.58e-5	2.92e-5	11.58	1.39
1	2.96e-4	1.27e-4	1.06e-4	4.60e-5	3.59e-5	2.88e-5	11.57	1.40
0.1	1.75e-4	9.00e-5	6.61e-5	2.96e-5	2.46e-5	1.65e-5	12.26	1.55
0.01	1.36e-4	9.64e-5	4.75e-5	4.64e-5	4.12e-5	2.12e-5	12.57	1.41
0.001	8.14e-4	3.73e-4	2.88e-4	1.66e-4	1.34e-4	9.83e-5	12.64	1.47
0	1.20e-3	4.49e-4	3.80e-4	2.15e-4	1.66e-4	1.37e-4	12.40	1.33

Table 3.1: Results of the Adaptive Strategy for $c_{\text{tol}_c} = 0.2$ and a varying History Parameter λ . The table describes the errors of the temperature field, measured in the L_∞ -norm $\|\Delta T\|_{Q,\infty}$ and in the L_2 -norm $\|\Delta T\|_{Q,2}$ on the time-space cylinder Q , the average $\overline{\|\Delta T\|_{\Omega,\infty}}$ and the standard deviation $\overline{\|\Delta T\|_{\Omega,\infty}}^\sigma$ over time of the error measured in the $L_\infty(\Omega)$ -norm on the domain Ω , $\overline{\|\Delta T\|_{\Omega,2}}$ and $\overline{\|\Delta T\|_{\Omega,2}}^\sigma$ in the $L_2(\Omega)$ -norm, and the average number of active nodes $\overline{|N_A|}$ as well as the standard deviation $\overline{|N_A|}^\sigma$ over time.

τ	$\ \Delta T\ _{Q,\infty}$	$\overline{\ \Delta T\ _{\Omega,\infty}}$	$\overline{\ \Delta T\ _{\Omega,\infty}}^\sigma$	$\ \Delta T\ _{Q,2}$	$\overline{\ \Delta T\ _{\Omega,2}}$	$\overline{\ \Delta T\ _{\Omega,2}}^\sigma$	$\overline{ N_A }$	$\overline{ N_A }^\sigma$
1	1.75e-4	9.00e-5	6.61e-5	2.96e-5	2.46e-5	1.65e-5	12.26	1.55
1.1	1.74e-4	8.97e-5	6.60e-5	2.95e-5	2.44e-5	1.66e-5	12.26	1.54
1.5	2.95e-4	1.28e-4	1.03e-4	4.57e-5	3.67e-5	2.72e-5	11.59	1.33
2	2.96e-4	1.27e-4	1.04e-4	4.58e-5	3.65e-5	2.77e-5	11.58	1.37
4	2.97e-4	1.27e-4	1.06e-4	4.62e-5	3.63e-5	2.86e-5	11.58	1.36
8	2.97e-4	1.27e-4	1.06e-4	4.64e-5	3.63e-5	2.90e-5	11.57	1.39
16	2.97e-4	1.27e-4	1.06e-4	4.65e-5	3.62e-5	2.92e-5	11.57	1.39

Table 3.2: Adaptive results for $\lambda = 0.1$ and $c_{\text{tol}_c} = 0.2$ as well as a norm-parameter τ .

nodes is initialized as $N_A(0) = (0, 0)^\top$, it is not updated randomly but according to the selection criteria described above; the Retrospective Method provides initial data for the future microscopic solution of newly activated macroscopic nodes; for this purpose the temperature is stored in every time step and in every macroscopic node.

This paragraph explores the Adaptive Strategy's dependence on the parameters λ , τ , c_{tol_c} , $c_{\text{tol}_r,0}$ as well as on the set A_{x^i} . Table 3.1 presents the dependence on the History Parameter λ . What surprises is that the Adaptive Strategy is least accurate in case that the metric takes into account the whole history of the temperature evolutions ($\lambda = 0$) in order to measure differences. Furthermore astonishingly is that the accuracy for the metric without a memory ($\lambda = 10000$) is significantly higher than the accuracy for the metric with the full memory ($\lambda = 0$). An optimal choice of λ seems to be 0.1: the accuracy measured in the $L_2(Q)$ -norm is highest and measured in the $L_\infty(Q)$ -norm is second best; furthermore, the average number of active nodes is only slightly larger than this category's minimum. Table 3.2 explores the dependence on τ : the numerical results show that the adaptive results for $\tau = 1$ are only insignificantly worse than the most accurate results for $\tau = 1.1$. Hence, in the following the weighted L_1 -norm is used to measure the distance of temperature evolutions because it is significantly simpler to measure such a distance in the weighted L_1 -norm than in any other weighted L_τ -norm with $\tau > 1$. The results in Table 3.3 for variations of c_{tol_c} indicate that the coarsening tolerance should not

c_{tol_c}	$\ \Delta T\ _{Q,\infty}$	$\overline{\ \Delta T\ _{\Omega,\infty}}$	$\overline{\ \Delta T\ _{\Omega,\infty}}^\sigma$	$\ \Delta T\ _{Q,2}$	$\overline{\ \Delta T\ _{\Omega,2}}$	$\overline{\ \Delta T\ _{\Omega,2}}^\sigma$	$ N_A $	$ N_A ^\sigma$
0	3.35e-4	8.43e-5	9.08e-5	5.88e-5	3.97e-5	4.34e-5	12.62	1.27
0.1	7.45e-4	2.05e-4	2.23e-4	9.38e-5	6.33e-5	6.92e-5	10.98	0.91
0.2	1.75e-4	9.00e-5	6.61e-5	2.96e-5	2.46e-5	1.65e-5	12.26	1.55
0.4	2.15e-4	1.06e-4	8.07e-5	3.22e-5	2.69e-5	1.77e-5	9.97	0.77
0.8	2.25e-4	1.06e-4	7.94e-5	3.53e-5	2.84e-5	2.09e-5	8.65	0.81

Table 3.3: Adaptive results for $\lambda = 0.1$ and a varying coarsening tolerance parameter c_{tol_c} .

$(\lambda, c_{\text{tol}_c})$	$\ \Delta T\ _{Q,\infty}$	$\overline{\ \Delta T\ _{\Omega,\infty}}$	$\overline{\ \Delta T\ _{\Omega,\infty}}^\sigma$	$\ \Delta T\ _{Q,2}$	$\overline{\ \Delta T\ _{\Omega,2}}$	$\overline{\ \Delta T\ _{\Omega,2}}^\sigma$	$ N_A $	$ N_A ^\sigma$
(1, 0)	1.90e-4	6.03e-5	4.78e-5	3.39e-5	2.65e-5	2.11e-5	13.53	1.52
(1, 0.1)	2.28e-4	9.52e-5	7.78e-5	3.55e-5	2.76e-5	2.22e-5	12.54	1.52
(1, 0.4)	2.94e-4	1.27e-4	1.05e-4	4.53e-5	3.55e-5	2.82e-5	10.36	0.93
(1, 0.8)	2.90e-4	1.26e-4	1.04e-4	4.43e-5	3.49e-5	2.74e-5	9.03	0.76
(0.01, 0)	1.86e-4	1.12e-4	6.03e-5	5.77e-5	4.92e-5	3.01e-5	12.68	1.37
(0.01, 0.1)	1.86e-4	1.12e-4	6.03e-5	5.77e-5	4.92e-5	3.01e-5	12.68	1.37
(0.01, 0.4)	1.81e-4	1.07e-4	5.86e-5	4.76e-5	4.21e-5	2.22e-5	10.43	0.97
(0.01, 0.8)	2.49e-4	1.44e-4	6.95e-5	5.78e-5	5.28e-5	2.36e-5	8.80	0.93

Table 3.4: Some further adaptive results for varying λ and c_{tol_c} .

$c_{\text{tol}_r,0}$	$\ \Delta T\ _{Q,\infty}$	$\overline{\ \Delta T\ _{\Omega,\infty}}$	$\overline{\ \Delta T\ _{\Omega,\infty}}^\sigma$	$\ \Delta T\ _{Q,2}$	$\overline{\ \Delta T\ _{\Omega,2}}$	$\overline{\ \Delta T\ _{\Omega,2}}^\sigma$	$ N_A $	$ N_A ^\sigma$
0	1.75e-4	9.00e-5	6.61e-5	2.96e-5	2.46e-5	1.65e-5	12.26	1.55
0.05	2.13e-4	8.12e-5	6.14e-5	3.62e-5	2.80e-5	2.29e-5	12.44	1.64
0.1	2.51e-4	1.04e-4	7.85e-5	3.96e-5	3.11e-5	2.46e-5	12.54	1.60
0.2	4.81e-4	1.26e-4	1.35e-4	8.22e-5	5.57e-5	6.05e-5	11.46	1.02

Table 3.5: Adaptive results for a varying refining tolerance parameter $c_{\text{tol}_r,0}$.

be too small. This observation is surprising because of the natural expectation that an increasing number of active nodes results in an increasing accuracy. An explanation for this phenomenon might be that a very small coarsening tolerance, somehow, prohibits the activation of macroscopic nodes with potentially valuable microscopic data. The Adaptive Strategy solves the problem most accurately for $c_{\text{tol}_c} = 0.2$. Table 3.4 presents some more results of the strategy for variations of the parameters λ and c_{tol_c} . What is interesting to note is that for both History Parameters $\lambda = 1$ and $\lambda = 0.01$, contrary to $\lambda = 0.1$, the strategy produces the most accurate results for $c_{\text{tol}_c} = 0$. However, comparing accuracy to cost of computation, the results presented in the Tables 3.1-3.4 suggest that the best pair of parameters is $(\lambda, c_{\text{tol}_c}) = (0.1, 0.2)$. Table 3.5 displays the dependence of the strategy on the refining tolerance parameter $c_{\text{tol}_r,0}$: increasing $c_{\text{tol}_r,0}$ results in a significant loss of accuracy; accordingly, this parameter does not have the desired influence, therefore it should be chosen to be zero. What is presented in Table 3.6 are results of the Adaptive Strategy depending on a varying strategy to select active nodes that contribute to the interpolation of microscopic data in inactive nodes. These results advise to select those active nodes with respect to the Equality Condition as well as to restrict their maximum number to be two. In other words, the results advise to interpolate the microscopic data

(eC, M_A)	$\ \Delta T\ _{Q,\infty}$	$\overline{\ \Delta T\ _{\Omega,\infty}}$	$\overline{\ \Delta T\ _{\Omega,\infty}}^\sigma$	$\ \Delta T\ _{Q,2}$	$\overline{\ \Delta T\ _{\Omega,2}}$	$\overline{\ \Delta T\ _{\Omega,2}}^\sigma$	$\overline{ N_A }$	$\overline{ N_A }^\sigma$
(0, 2)	2.70e-4	8.05e-5	6.76e-5	3.90e-5	3.00e-5	2.49e-5	12.25	1.54
(1, 2)	1.75e-4	9.00e-5	6.61e-5	2.96e-5	2.46e-5	1.65e-5	12.26	1.55
(0, 4)	8.59e-4	3.19e-4	2.46e-4	2.84e-4	2.22e-4	1.77e-4	11.92	1.25
(1, 4)	2.67e-4	7.98e-5	6.78e-5	3.78e-5	2.79e-5	2.55e-5	12.26	1.55
(0, 8)	3.16e-3	1.19e-3	9.61e-4	1.25e-3	9.60e-4	8.02e-4	12.00	1.35
(1, 8)	8.01e-4	1.82e-4	2.17e-4	1.25e-4	7.80e-5	9.78e-5	12.26	1.55
(0, $ N_A $)	7.78e-3	2.29e-3	2.20e-3	2.65e-3	1.91e-3	1.85e-3	11.65	1.07
(1, $ N_A $)	1.42e-3	2.96e-4	3.79e-4	2.06e-4	1.23e-4	1.65e-4	12.26	1.55

Table 3.6: Adaptive results for a varying method to select active nodes that contribute to the interpolation of microscopic data in inactive nodes. $eC = 1$ claims that the active nodes are chosen with respect to the Equality Condition, and otherwise without respect to that condition. M_A defines the maximum number of active nodes that contribute to an interpolation; there is no upper bound for $M_A = |N_A|$.

Method	$\ \Delta T\ _{Q,\infty}$	$\overline{\ \Delta T\ _{\Omega,\infty}}$	$\overline{\ \Delta T\ _{\Omega,\infty}}^\sigma$	$\ \Delta T\ _{Q,2}$	$\overline{\ \Delta T\ _{\Omega,2}}$	$\overline{\ \Delta T\ _{\Omega,2}}^\sigma$	$\overline{ N_A }$	$\overline{ N_A }^\sigma$
ST-CA	4.31e-4	2.05e-4	1.41e-4	1.07e-4	8.83e-5	6.05e-5	11.82	1.20
IT-CA	1.75e-4	9.00e-5	6.61e-5	2.96e-5	2.46e-5	1.65e-5	12.26	1.55
ST-SA	7.40e-3	1.23e-3	1.18e-3	2.74e-4	2.07e-4	1.80e-4	12.03	1.32
IT-SA	1.22e-3	4.08e-4	3.59e-4	2.52e-4	1.83e-4	1.74e-4	11.90	1.24

Table 3.7: Adaptive results for a varying method that approximates latent heat released in inactive nodes. ST denotes the Single and IT the Interpolation Transfer Method for the data, CA denotes the Complete and SA the Separate Approximation Method. The Equality Condition and M_A influence, of course, only the interpolation approaches IT-CA and IT-SA.

of an inactive node only between the data of the most similar active node with higher and of the most similar active node with lower temperature evolution. Furthermore, since for every value of M_A the performance of the method with respect to the Equality Condition is significantly better than of the method without respect to that condition, the Equality Condition seems to be fundamental to the adaptive solution's accuracy. In conclusion, the results presented in this paragraph suggest that quite an optimal choice for the parameter set $(\lambda, \tau, c_{\text{tol},c}, c_{\text{tol},0}, eC, M_A)$ is $(0.1, 1, 0.2, 0, 1, 2)$.

This paragraph focuses on the Adaptive Strategy's dependence on the method that approximates the latent heat released in inactive nodes: there are two methods for the transfer of data (Single (ST) and Interpolation Transfer (IT), of course with $eC = 1$ and $M_A = 2$ in case of IT) and two for the type of approximation (Complete (CA) and Separate Approximation (SA)). Table 3.7 clearly reveals that the method IT-CA performs significantly better than the other methods: the average number of active nodes is similar for all methods, but method IT-CA's accuracy is significantly higher than the other methods' accuracy. The method ST-SA performs worst. This can also be seen in Figure 3.5, which illustrates the final temperature solutions for the methods IT-CA and ST-SA. Indeed hard to see, but the temperature field of ST-SA comprises some slight non-physical oscillations. It is different with IT-CA: the temperature field is smooth. The non-physical oscillations

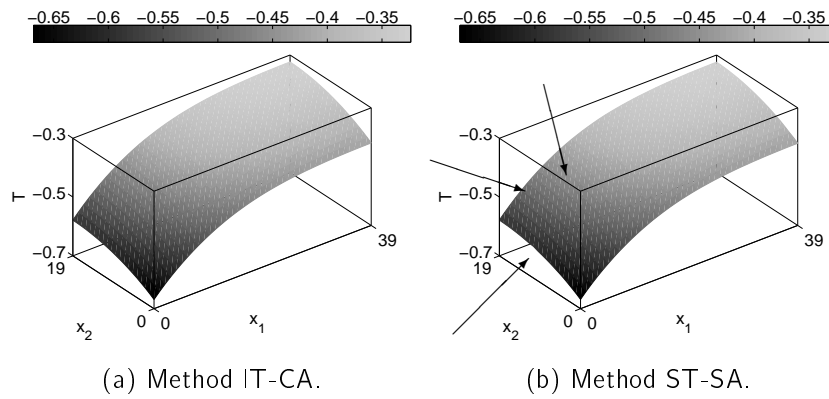


Figure 3.5: Adaptive macroscopic temperature solutions at final time in two-space dimensions. Figure (a) presents the temperature for approximation method IT-CA, and Figure (b) for ST-SA. The arrows in (b) point at some slight non-physical oscillations in the temperature field for ST-SA.

increment	$\ \Delta T\ _{Q,\infty}$	$\overline{\ \Delta T\ _{\Omega,\infty}}$	$\overline{\ \Delta T\ _{\Omega,\infty}}^\sigma$	$\ \Delta T\ _{Q,2}$	$\overline{\ \Delta T\ _{\Omega,2}}$	$\overline{\ \Delta T\ _{\Omega,2}}^\sigma$	$\overline{N_A}$	$\overline{N_A}^\sigma$
{1,10,100}	1.75e-4	9.00e-5	6.61e-5	2.96e-5	2.46e-5	1.65e-5	12.26	1.55
1000	1.75e-4	8.99e-5	6.61e-5	2.95e-5	2.45e-5	1.65e-5	12.26	1.55
10000	1.75e-4	8.96e-5	6.60e-5	2.85e-5	2.39e-5	1.55e-5	12.26	1.55
100000	1.66e-4	8.76e-5	6.24e-5	3.33e-5	2.73e-5	1.90e-5	12.26	1.55

Table 3.8: Adaptive results for a varying time increment for storing the history of the macroscopic temperature field. The increment influences the Retrospective Method.

in the temperature field of ST-SA arise, at least it is likely that they do, from the Separate Approximation Method of the latent heat released in inactive nodes: for instance, assume that firstly x^{a_1} and x^{a_2} are active nodes; secondly, as in the current example, that every active node's solid phase grows permanently, meaning the latent heat released in active nodes is always positive; thirdly that x^i is an inactive node whose most similar active node of time step n is x^{a_1} and of time step $n+1$ it is x^{a_2} ; then method ST-SA, see (3.24), approximates the latent heat released in x^i in time step $n+1$ by $\overline{\phi_{x^{a_1}}^{n+1}}^Y - \overline{\phi_{x^{a_2}}^n}^Y$, this difference can be of negative value; and a negative latent heat released in an inactive node causes a dent in the temperature field at the inactive node. Such dents are flattened out by the interpolation strategy. Dents seem to be unlikely in case of the Complete Approximation Method, this is because (taking into account the assumptions from above) latent heat released is always positive in every macroscopic node. Finally in this paragraph, Figure 3.6 displays the errors of the temperature field for the different strategies, measured in the $L_2(\Omega)$ - and the $L_\infty(\Omega)$ -norm. All the errors grow with increasing time (disregarding a few small time spans). The errors of ST-SA oscillate rapidly with large magnitudes. There is also oscillation for IT-SA, but because of the interpolation on a smaller level. The errors of the complete approximation strategies do not oscillate at all. A possible explanation for the oscillations is again the "dent-production" of the Separate Approximation methods.

Table 3.8 shows the influence of the time increment for memorizing the history of the temperature field on the performance of the Adaptive Strategy depending on the

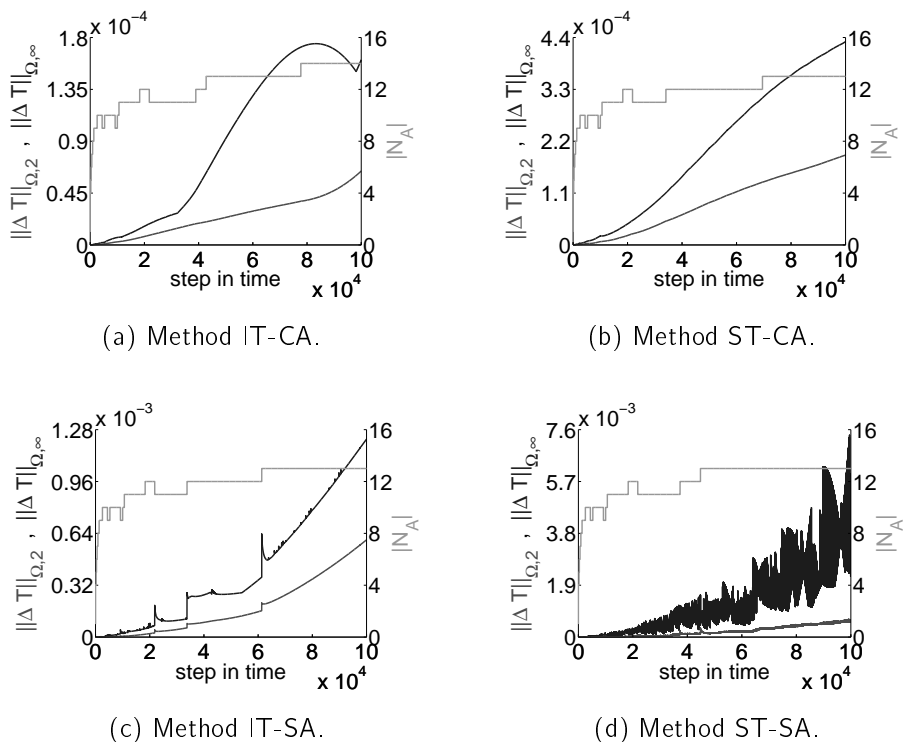


Figure 3.6: $L_2(\Omega)$ -norm $\|\Delta T\|_{\Omega,2}$ and $L_\infty(\Omega)$ -norm $\|\Delta T\|_{\Omega,\infty}$ of the error of the temperature field on the macroscopic domain Ω , as well as the number of active nodes $|N_A|$, all plotted versus the time step, for the Adaptive Strategy with method IT-CA in (a), ST-CA in (b), IT-SA in (c) and ST-SA in (d). Please note that the left axes of the graphs do not have the same limits.

Retrospective Method: for the moment surprising is the observation that the increment does not influence the performance significantly, but this is only due to the fact that the temperature in the activated macroscopic nodes either decreased at nearly constant rate or was nearly constant itself.

Finally, the Adaptive Strategy is opted for the method that selects the active macroscopic nodes. The first line of Table 3.9, which presents average results of ten solutions of the Adaptive Strategy with random initial active macroscopic node, suggests that if the set of active nodes is updated by execution of all three update routines, meaning in particular the macroscopic nodes with highest and with lowest temperature evolution are always active, and if macroscopic nodes are selected according to the criteria described above, then the solution of the Adaptive Strategy is nearly independent of the one macroscopic node that is active in the beginning. This can also be seen in Figure 3.7(a), which shows the distribution of the active nodes on the macroscopic domain at final time t_{end} for all ten solutions: nine of ten solutions produce the same distribution. The average accuracy decreases significantly in case that the macroscopic nodes with highest or lowest temperature evolutions are active not by instruction but only if they are not similar to an active node, that is only if their latent heat released is not approximated accurately enough. The same is observed for the case that the macroscopic nodes to be activated or deactivated are selected randomly: the average accuracy is significantly higher if the macroscopic nodes with highest or lowest temperature evolutions are active by instruction (compare

(RI,RU,AE)	$\overline{\ \Delta T\ _{Q,\infty}}$	$\overline{\ \Delta T\ _{Q,\infty}}^\sigma$	$\overline{\ \Delta T\ _{Q,2}}$	$\overline{\ \Delta T\ _{Q,2}}^\sigma$	$\overline{ N_A }$	$\overline{ N_A }^\sigma$
(1, 0, 1)	1.88e-4	3.91e-5	3.11e-5	4.68e-6	12.25	1.10e-2
(1, 0, 0)	3.82e-4	3.08e-4	6.94e-5	5.71e-5	11.99	5.26e-1
(1, 1, 1)	2.52e-4	7.52e-5	4.16e-5	1.26e-5	11.19	6.94e-1
(1, 1, 0)	4.69e-4	3.60e-4	9.29e-5	7.33e-5	10.97	8.96e-1

Table 3.9: Adaptive results for a varying method to select active macroscopic nodes. *RI* abbreviates random initial macroscopic node, that is $RI=1$ demands that the initial active macroscopic node is chosen randomly. *RU* means random update of the set of active nodes: the macroscopic nodes to be activated or deactivated are chosen according to the selection criteria described above for $RU=0$, for $RU=1$ those nodes are chosen randomly. *AE* abbreviates activating the macroscopic nodes with extreme temperature evolutions: for $AE=0$ the First Refining Routine is omitted and the first criterion of the Coarsening Routine is invalid, that means that the macroscopic nodes with highest or lowest temperature evolutions are only active if their latent heat released is not approximated accurately enough; for $AE=1$ they are always active. Each line of the table presents the results of ten adaptive solutions: $\overline{\|\Delta T\|_{Q,\infty}}$ is the average and $\overline{\|\Delta T\|_{Q,\infty}}^\sigma$ is the standard deviation of the ten errors of the temperature field measured in the L_∞ -norm on the space time-cylinder Q , $\overline{\|\Delta T\|_{Q,2}}$ and $\overline{\|\Delta T\|_{Q,2}}^\sigma$ denote the same for the L_2 -norm, and $\overline{|N_A|}$ and $\overline{|N_A|}^\sigma$ are the average and the standard deviation of the ten numbers of active macroscopic nodes averaged over time.

the results of $(RI,RU,AE)=(1,1,1)$ to the results of $(RI,RU,AE)=(1,1,0)$). Choosing the active macroscopic nodes according to the selection criteria rather than randomly results on average in a higher accuracy. What is also interesting to note in Figure 3.7 is that most of the active nodes are around macroscopic node $(0,0)^T$: this is due to the fact that this is the subdomain of Ω_{hg} in which the differences in the temperature field are largest.

This subsection opted the Adaptive Strategy for its methods and parameters in dependence on the parameter $c_{tol,r,1} = 0.1$ of the refining tolerance (3.10). The next subsection will prove that for $c_{tol,r,1}$ tending to zero the solution of the Adaptive Strategy converges to the direct solution.

3.4.1.2 Convergence of the adaptive strategy for $c_{tol,r,1} \rightarrow 0$

The previous subsection opted the Adaptive Strategy for in dependence not only on the fixed parameter $c_{tol,r,1} = 0.1$ of the refining tolerance (3.10) but also in dependence on the Retrospective Method, which retrospectively computes the *new* initial data of newly activated macroscopic nodes. Contrary to that, in this subsection the parameter $c_{tol,r,1}$ is varied. Moreover, not the Retrospective Method but the Copy Method is used, meaning that the microscopic data of the most similar active node is used as new initial condition for a newly activated node. The other methods and parameters are given as listed in the beginning of the Subsection 3.4.1.1. Table 3.10 provides at least three interesting informations. Firstly, as expected, the adaptive solution for $c_{tol,r,1} = 0.1$ for the Copy Method is less accurate than for the Retrospective Method (compare line three of Table 3.10 to line one of Table 3.8). Secondly, assuming that the optimal choice of methods and parameters

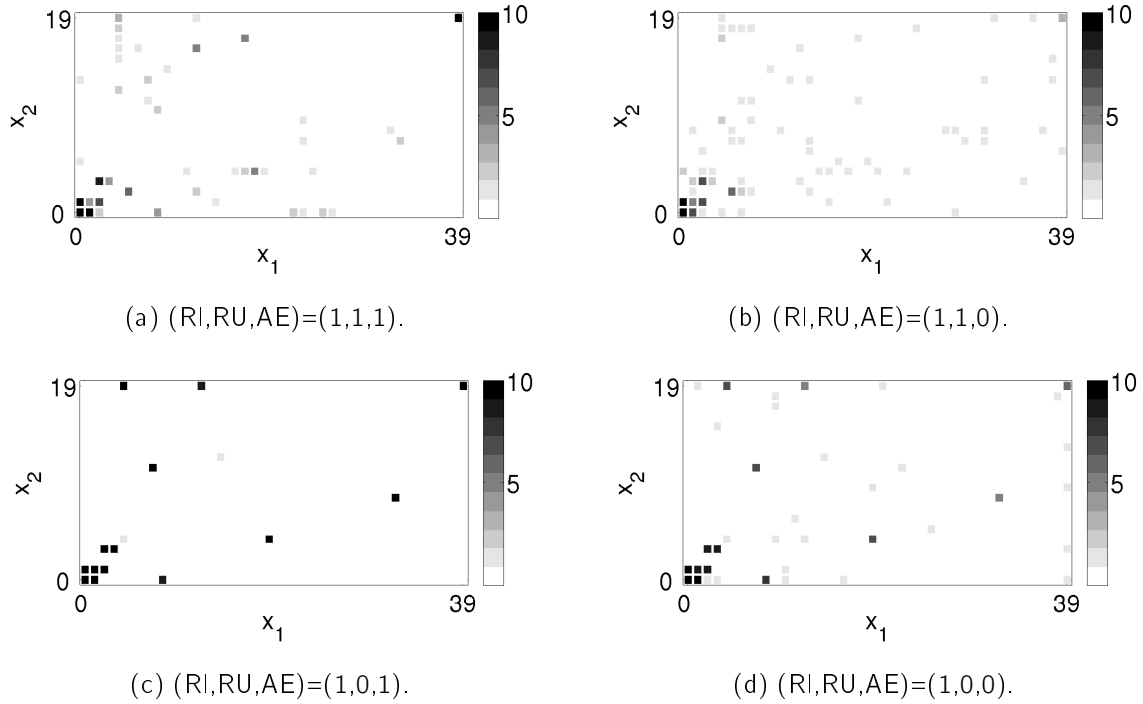


Figure 3.7: Results for the same Adaptive Strategies as in Table 3.9. Figure (a) depicts the distribution of the active macroscopic nodes on the macroscopic domain in the end of the time-interval for the ten solutions of the Adaptive Strategy with $(RI,RU,AE)=(1,1,1)$: the marker colors indicate in how many solutions a macroscopic node is active. Figure (b) depicts the same for $(RI,RU,AE)=(1,1,0)$, (c) for $(RI,RU,AE)=(1,0,1)$ and (d) for $(RI,RU,AE)=(1,0,0)$.

$c_{tol,r,1}$	$\ \Delta T\ _{Q,\infty}$	$\overline{\ \Delta T\ _{\Omega,\infty}}$	$\overline{\ \Delta T\ _{\Omega,\infty}}^\sigma$	$\ \Delta T\ _{Q,2}$	$\overline{\ \Delta T\ _{\Omega,2}}$	$\overline{\ \Delta T\ _{\Omega,2}}^\sigma$	$\overline{ N_A }$	$\overline{ N_A }^\sigma$
1	$1.26e-2$	$2.88e-3$	$3.46e-3$	$2.81e-3$	$1.78e-3$	$2.18e-3$	2.00	0.00
0.316	$2.49e-3$	$6.13e-4$	$7.12e-4$	$4.18e-4$	$2.64e-4$	$3.24e-4$	4.00	0.01
0.1	$2.14e-4$	$8.30e-5$	$5.76e-5$	$4.76e-5$	$3.84e-5$	$2.82e-5$	12.26	1.55
0.0316	$3.87e-4$	$1.43e-4$	$1.28e-4$	$5.76e-5$	$4.23e-5$	$3.92e-5$	29.52	3.89
0.0316*	$1.47e-4$	$6.35e-5$	$4.25e-5$	$3.19e-5$	$2.64e-5$	$1.79e-5$	32.03	4.14
0	$0.00e+0$	$0.00e+0$	$0.00e+0$	$0.00e+0$	$0.00e+0$	$0.00e+0$	799.82	10.23

Table 3.10: Adaptive results for $\lambda = 0.1$, $\tau = 1$, $c_{tol,c} = 0.2$, $c_{tol,r,0} = 0$, $c_{tol,e} = 0.01$, $eC = 1$, $M_A = 2$, $IT-CA$, $N_A(0) = (0,0)^\top$, the Copy Method and a varying refining tolerance parameter $c_{tol,r,1}$. For 0.0316* it is $c_{tol,c} = 0.1$ instead of $c_{tol,c} = 0.2$.

of the Adaptive Strategy for the Retrospective Method is equal for the Copy Method, a little surprising is the observation that for $c_{tol,r,1} = 0.0316$, in contrast to $c_{tol,r,1} = 0.1$, the optimal coarsening tolerance parameter is $c_{tol,c} = 0.1$ rather than $c_{tol,c} = 0.2$. However, the most important observation in Table 3.10 is, thirdly, that the adaptive solution converges to the direct solution for the refining tolerance tending to zero. For $c_{tol,r,1} = 0$, the solution of the Adaptive Strategy is equal to the direct solution, only the initial condition of the temperature field circumvents that all macroscopic nodes are always active.

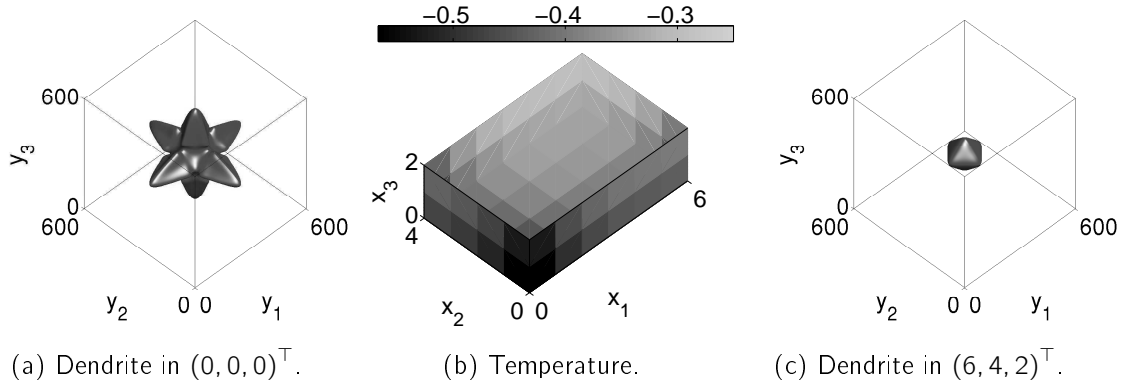


Figure 3.8: Direct solution of the two-scale model (on the small macroscopic grid) in three space dimensions. Figure (b) depicts the macroscopic temperature field at final time on some boundary parts of the macroscopic domain. Figure (a) presents the dendritic microstructure in the end of the simulation in macroscopic node $(0, 0, 0)^T$: because of the macroscopic boundary conditions, this node always records the lowest temperature and, consequently, its dendritic microstructure is always largest. Figure (c) shows the smallest dendrite in the end of the time-interval, it is located in macroscopic node $(6, 4, 2)^T$.

3.4.2 Numerical results in three space dimensions

Now, the Adaptive Strategy solves the two-scale model in three space dimensions. At first, on a small macroscopic grid, it is shown that the adaptive solution converges to the direct solution. Afterwards, the Adaptive Strategy solves the model on a huge macroscopic grid.

3.4.2.1 Convergence of the adaptive strategy for $c_{\text{tol},1} \rightarrow 0$

The two-scale model to be solved in three space dimensions is given by the microscopic problem (3.3) and (3.4) on the microscopic domain $Y_{h_\ell} = [0, 600h_\ell]^3$ with space increment $h_\ell = 0.4W_0$, and by the macroscopic heat equation (3.1) on the macroscopic domain $\Omega_{h_g} = [0, 6h_g] \times [0, 4h_g] \times [0, 2h_g]$ with $h_g = 600h_\ell$. Therefore, Ω_{h_g} consists of only 105 nodes, but each of them is governing one microscopic problem on Y_{h_ℓ} consisting of 601^3 nodes. The computation time is from 0 to $12000k_t$ with time increment $k_t = 0.018\tau_0$. On the macroscopic scale, the effective heat conductivity K_0 is chosen as 600, the boundary conditions of the heat equation are prescribed heat fluxes:

$$\nabla T \cdot n = \begin{cases} -0.25 \cdot \frac{1}{12000} \cdot \frac{0.4 \cdot 600}{0.018} \cdot \frac{1}{600} & \text{for } x_1 = 0, \\ -0.2 \cdot \frac{1}{12000} \cdot \frac{0.4 \cdot 600}{0.018} \cdot \frac{1}{600} & \text{for } x_2 = 0, \\ -0.15 \cdot \frac{1}{12000} \cdot \frac{0.4 \cdot 600}{0.018} \cdot \frac{1}{600} & \text{for } x_3 = 0, \\ 0 & \text{otherwise.} \end{cases} \quad (3.28)$$

Thus, as in the two-dimensional setting, some parts of the boundary have cooling conditions, and the remaining parts are isolated. The initial temperature T , the initial chemical

$c_{\text{tol},1}$	$\ \Delta T\ _{Q,\infty}$	$\overline{\ \Delta T\ _{\Omega,\infty}}$	$\overline{\ \Delta T\ _{\Omega,\infty}^\sigma}$	$\ \Delta T\ _{Q,2}$	$\overline{\ \Delta T\ _{\Omega,2}}$	$\overline{\ \Delta T\ _{\Omega,2}^\sigma}$	$ N_A $	$ N_A ^\sigma$
1	3.73e-3	6.51e-4	9.47e-4	7.91e-4	4.46e-4	6.54e-4	2.00	0.01
0.316	6.79e-4	1.25e-4	1.73e-4	1.48e-4	8.37e-5	1.22e-4	3.30	0.46
0.1	2.23e-4	3.90e-5	6.01e-5	2.56e-5	1.36e-5	2.17e-5	8.05	1.06
0.0316	1.95e-4	2.58e-5	4.50e-5	1.19e-5	6.21e-6	1.01e-5	21.38	5.22
0	0.00e+0	0.00e+0	0.00e+0	0.00e+0	0.00e+0	0.00e+0	104.91	1.92

Table 3.11: Adaptive results of the Adaptive Strategy in three space dimensions for $\lambda = 0.1$, $\tau = 1$, $c_{\text{tol},c} = 0.1$, $c_{\text{tol},r,0} = 0$, $c_{\text{tol},e} = 0.01$, $eC = 1$, $M_A = 2$, IT-CA, $N_A(0) = (0, 0, 0)^\top$, the Copy Method and a varying refining tolerance parameter $c_{\text{tol},1}$.

potential U and the initial phase field ϕ are specified as ($\forall x \in \Omega_{h_g}, \forall y \in Y_{h_\ell}$)

$$\begin{aligned}
T(0, x) &= -0.25, \\
U(0, x, y) &= 0, \\
\phi(0, x, y) &= \tanh\left(-0.3 \left(\left|\frac{1}{h_\ell}y - (300, 300, 300)^\top\right| - 5\right)\right).
\end{aligned} \tag{3.29}$$

Consequently, a small solid kernel occupies, surrounded by an undercooled melt, the center of every microscopic domain. Figure 3.8 presents the corresponding direct solution.

Table 3.11 shows that the solution of the Adaptive Strategy converges to the direct solution for the refining tolerance tending to zero – to put it simply, this observation shows that the Adaptive Strategy works accurately not only in two but also in three space dimensions.

3.4.2.2 Adaptive Solution on a Huge Macroscopic Domain

Finally, Figure 3.9 presents the solution of the Adaptive Strategy with $c_{\text{tol},1} = 0.1$ on the large three-dimensional macroscopic grid $\Omega_{h_g} = [0, 39h_g] \times [0, 29h_g] \times [0, 19h_g]$. Therefore, Ω_{h_g} consists of 24000 nodes and each of them is governing one microscopic problem on Y_{h_ℓ} consisting of 601^3 nodes. The physical parameters are the same as in Section 3.4.2.1, the only difference is the heat conductivity $K_0 = 4.8 \cdot 10^4$ and the boundary condition $\nabla T \cdot n = c_T \cdot \frac{1}{12000} \cdot \frac{0.4 \cdot 600}{0.018} \cdot \frac{1}{4.8 \cdot 10^4}$ with $c_T = -1.6$ for $x_1 = 0$, $c_T = -1.1$ for $x_2 = 0$, $c_T = -0.9$ for $x_3 = 0$ and $c_T = 0$ otherwise. Most of the active nodes are accumulated near $(0, 0, 0)^\top$, that is in the subdomain of Ω_{h_g} where the temperature values differ most.

Solving the problem directly requires, in every step of time, to solve each and every one of the 24000 microscopic problems. This requires enormous computing and memory resources. Contrary to that, the Adaptive Strategy solves, in every step of time, on average only 13.03 microscopic problems – despite this large reduction of numerical effort the resulting temperature field is smooth.

3.5 Conclusion and outlook

The presented numerical results indicate that the Adaptive Strategy is a very powerful ingredient for an accurate and fast algorithm to solve two-scale models with continuous inter-scale dependencies. For the considered sample model, the strategy's performance

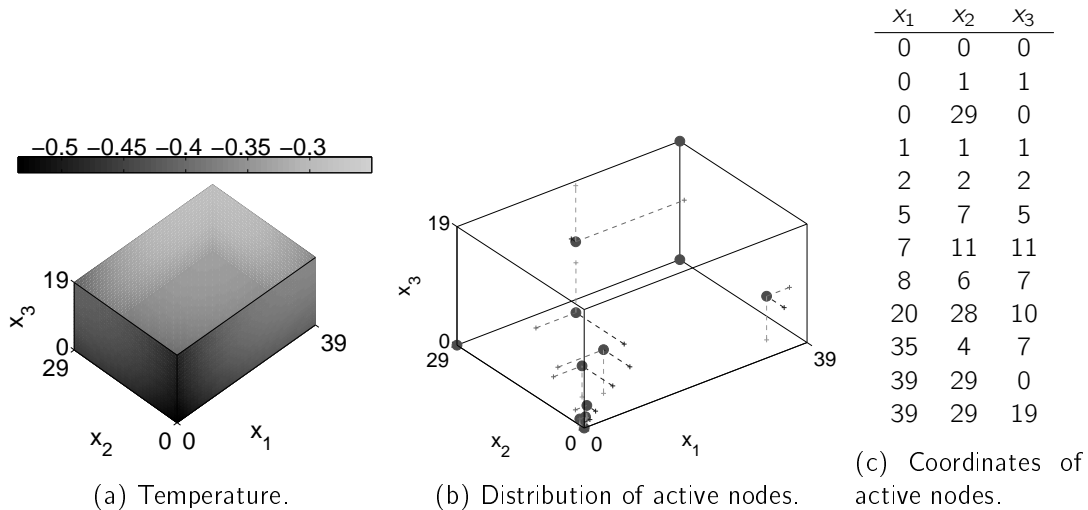


Figure 3.9: Solution of the Adaptive Strategy for $c_{\text{tol},1} = 0.1$ of the two-scale problem on a huge three-dimensional macroscopic grid. Figure (a) shows the final temperature solution on some parts of the boundary of the macroscopic domain, (b) depicts the distribution of the active macroscopic nodes (indicated by balls) in the end of the time-interval, and Table (c) presents their coordinates.

depends in particular on the refining tolerance: the smaller the tolerance the higher the computational effort but also the solution's accuracy. What is surprising is the low dependence of the adaptive results on the History Parameter λ . On the contrary, the method that approximates the latent heat released in inactive macroscopic nodes influences the adaptive result significantly: the result is most accurate for the method IT-CA (Interpolation Transfer of data from active to inactive nodes and Complete Approximation of latent heat released); the worst result is exhibited with the method ST-SA (Single Transfer of data and Separate Approximation); the other approximation methods perform slightly worse than the method IT-CA. Another important tool of the Adaptive Strategy is the Equality Condition: interpolating the microscopic data of an inactive node only between the microscopic data of the active node with the most similar *higher* temperature evolution and of the active node with the most similar *lower* temperature evolution, increases the adaptive solution's accuracy significantly.

In order to justify the Adaptive Strategy mathematically, it is intended to prove an error estimate of the type

$$\begin{aligned} & \|\phi^{(1)}(t, \cdot) - \phi^{(2)}(t, \cdot)\|_{L_2(\mathcal{Y})} + \|U^{(1)}(t, \cdot) - U^{(2)}(t, \cdot)\|_{L_2(\mathcal{Y})} \\ & \leq C \cdot d_E(T^{(1)}, T^{(2)}; t, \lambda, \tau) \end{aligned} \quad (3.30)$$

for the solutions $(\phi^{(\ell)}, U^{(\ell)})$ of the microscopic problem (3.3) and (3.4) to temperature evolutions $T^{(\ell)}(t)$ for $\ell = 1, 2$. Corollary 2.7 proves such an error estimate for a similar two-scale model for $\lambda \geq 0$ and $1 < \tau \leq s$ if $T^{(1)}$ and $T^{(2)}$ are s -th power integrable functions.

Models that include sidebranching of dendrites usually use stochastic perturbations in the equations for the temperature field or the field of the chemical potential. The Adaptive Strategy's method that selects microscopic cell problems that are numerically computed

depends only on the difference of temperatures. Hence, it is in principle possible to apply the strategy directly to a corresponding model with stochastic perturbations of the chemical potential. There are two possibilities to handle stochastic perturbations within this strategy. The first method computes for each active node only one sample with a randomly generated perturbation. It is likely that the number of active nodes increases, because the latent heat that enters to the macroscopic heat equation may be changed by the stochastic perturbations. Due to the same reason the difference between the results for the direct approach and the Adaptive Strategy may increase; but this would also be the case for two solutions of the direct approach with different perturbations. The second method computes the microscopic cell problems for several or many different stochastic perturbations and uses the mean value of the latent heat in the macroscopic equations. In this case it is likely that the accuracy of the Adaptive Strategy is similar to that of the Adaptive Strategy for the (physical) case without perturbations. However, the computation of the cell problems is numerically expensive, therefore the solution of several cell problems for one active node increases the required numerical effort considerably.

Further improvements of the Adaptive Strategy may be possible with a method that approximates the microscopic data in inactive nodes not only by microscopic data computed in the current time step but also by data computed in previous time steps; this will be a topic of future research. Nevertheless, in its current state, compared to the direct solution, the Adaptive Strategy already provides a tremendous increase of computational speed while losing only little accuracy.

Acknowledgment

The results presented in this section result from joint work with Christof Eck. They have been published by *Journal of Computational Physics*, [49].

4 A POD-EIM reduced two-scale model for crystal growth

Abstract

Complex physical models depending on microstructures developing over time often result in simulation schemes that are very demanding concerning computational time. The two-scale model considered in the current presentation describes a phase transition of a binary mixture with the evolution of equiaxed dendritic microstructures. It consists of a macroscopic heat equation and a family of microscopic cell problems modeling the phase transition. Those phase transitions need to be resolved by very fine computational meshes leading to the demanding numerical complexity.

The current study presents a reduced version of this two-scale model. The reduction aims at accelerating the microscopic model, which is parametrized by the macroscopic temperature, while maintaining the accuracy of the detailed system. Parameter dependency, non-linearity, time-dependency, coupled field-variables and high solution complexity are challenging difficulties. They are addressed by a combination of several approaches: Proper Orthogonal Decomposition (POD), Empirical Interpolation Method (EIM) and a partitioning approach generating sub-models for different solution regimes. A new partitioning criterion based on feature extraction is applied.

The applicability of the reduction scheme is demonstrated experimentally: while the accuracy is largely maintained, the dimensionality of the detailed model and the computation time are reduced significantly.

4.1 Introduction

Many technically relevant processes exhibit a priori unknown microstructures that evolve in time. Important examples are solidification processes with dendritic and eutectic microstructures [16, 43], flow in porous media with changing pore geometry as a consequence of elastoplastic deformations and deposition or desorption of matter, and microstructures in epitaxial growth of thin solid layers. Due to huge differences in relevant length and possibly also time scales, it is usually not feasible to simulate such processes by a direct numerical discretization of a full model. A much more promising approach is the usage of homogenization or averaging techniques, that were originally developed with the aim to find purely macroscopic models with suitable constitutive laws that model the properties of the microstructure [15, 32, 34]. The application of those methods to processes with evolution of a priori unknown microstructures typically leads to full two- or multi-scale models that combine differential equations on the smallest scales with homogenized differential equations on the macroscopic scales [19]. Both scales are coupled: the macroscopic fields influence the evolution of the microstructure, and the microscopic fields enter the homogenized equations via averaged coefficients. A direct discretization of such a model typically requires the solution of a full microscopic cell problem for every node of a macroscopic numerical grid. This leads to a huge numerical complexity and limits the application to problems with comparatively small macroscopic grids.

The present study presents a model reduction approach for a two-scale model for crystal growth. The procedure aims at the reduction of the microscopic model in order to accelerate the overall model. The problem poses several challenges for model reduction: parameter dependency via the macroscopic temperature, high dimensionality, several coupled field variables, time-dependency and non-linearity in the microscopic model. Correspondingly,

several modern reduction strategies need to be combined. First, the high dimensionality of the microscopic model is addressed via a Proper Orthogonal Decomposition (POD) strategy [35, 58], i.e. snapshot-based generation of a low-dimensional approximation space and projection of the detailed microscopic model to this subspace. Different POD spaces for the different field variables are generated resulting in coupled reduced models. The non-linearity and parameter-dependency is addressed by the Empirical Interpolation Method (EIM) [2], which enables to efficiently evaluate local parametric discretization operators as in [14, 18]. Finally, the high solution complexity demands for partitioning approaches of the reduced models. This means, that not only one set of bases is generated, but several sets of reduced bases for different solution regimes. During the simulation a switching between these sub-models is realized by orthogonal projection. The criterion for partitioning is not time [17] nor some implicit partitioning [47, 59], but a partitioning according to a problem specific criterion that is obtained via a feature extraction of the present solution.

The reader is referred to other methods for the efficient solution of multi-scale models as e.g. [33, 56] as well as the adaptive strategy of Section 3, which are different to the current approach, which has some similarity to the method introduced in [53] using a database approach. In [53] the microscopic problems in the multi-scale model are replaced by simplified sample problems with prescribed macroscopic fields which are obtained by a global iterative procedure. Some further approaches of model reduction for multi-scale methods can be found in the literature, as the combination of these fields is currently a very active direction. Reduced basis approaches for cell problems in stationary two-scale problems have been presented in [5, 45]. An instationary problem of polymeric flow involving macroscopic and microscopic models and their reduction has been shown in [40]. Projection-based approaches in the spirit of multi-scale FEM can also be found in [1, 38]. In contrast to these, the considered microscopic model is a coupled nonlinear system, that requires more complex approximation procedures to obtain successful reduction.

The organization of this section is as follows: Subsection 4.2 describes the detailed two-scale model to be solved, Subsection 4.3 introduces the reduced two-scale model, and finally Subsection 4.4 presents numerical results in two space dimensions which show the reduced model's efficiency.

4.2 The detailed two-scale model

Many solidification processes develop dendritic microstructures of equiaxed morphology as illustrated in Figure 4.1. Equiaxed structures grow from small solid kernels that nucleate in an undercooled melt. During solidification these kernels develop dendritic instabilities, for more details see e.g. [16] or [43]. To control these instabilities, models for dendritic growth must account for curvature undercooling and possibly also kinetic undercooling. The phenomenologically simplest model is the Stefan problem with Gibbs-Thomson effect, [57]. In contrast to the Stefan problem, a phase-field model approximates the sharp transition layer between the solid and the liquid phase by a diffuse phase transition region, [9]: the phase transition is described by a phase-field ϕ , which smoothly varies from its liquid value ϕ_ℓ to its solid value ϕ_s .

The detailed two-scale model is obtained by the application of a homogenization technique, under the assumption of fast heat diffusion and slow solute diffusion, to a microscopic model describing a solidification process of a binary mixture. The two-scale model

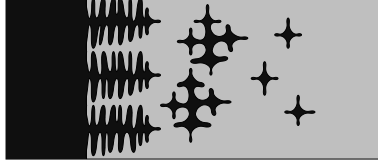


Figure 4.1: Columnar (on the left) and equiaxed dendritic structures, [22].

consists of a macroscopic homogenized heat equation, and for each point of the macroscopic domain of a microscopic cell problem with periodic boundary conditions. For details see [20, 21, 23] or the brief recapitulation in Section 2. Please note that the here considered model results from the model considered in Section 2 by the substitution $c = u - \phi$, the specifications $L = 1$, $D_1 = 1$, $D_2 = -1$ and $K(\phi) = K \in \mathbb{R}$ and the commutation of the liquid and the solid value of the phase-field.

4.2.1 The macroscopic homogenized heat equation

The macroscopic heat equation in dimensionless form reads

$$\partial_t T - K \Delta_x T = \partial_t \overline{\phi}^Y. \quad (4.1)$$

It is solved for the macroscopic temperature field $T = T(t, x)$ in the macroscopic time-space cylinder $Q = I_{t_{\text{end}}} \times \Omega$ consisting of the time interval $I_{t_{\text{end}}} = [0, t_{\text{end}}]$ and the macroscopic domain $\Omega \subset \mathbb{R}^2$. The averaged phase-field

$$\overline{\phi(t, x)}^Y = \frac{1}{|Y|} \int_Y \phi(t, x, y) dy \quad (4.2)$$

depends on the microscopic cell problem in macroscopic point x , where Y denotes the microscopic cell domain; $\partial_t \overline{\phi(t, x)}^Y$ describes the averaged latent heat that is released during the phase transition from liquid to solid. The parameter K describes the heat conductivity, which is independent of the phase-field. The macroscopic equation is supplemented by a Neumann boundary condition and a constant initial temperature $T(0, x) = T_0$ for all $x \in \Omega$.

4.2.2 The microscopic cell problems

The microscopic cell problems describe the liquid-solid phase transition of a binary mixture. The governing equations in dimensionless form are

$$\partial_t u - \Delta_y u = \partial_t \phi, \quad (4.3)$$

$$\alpha \xi^2 \partial_t \phi - \xi^2 \Delta_y \phi + p'(\phi) - q(T, u, \phi) = 0. \quad (4.4)$$

The microscopic problem in a macroscopic point $x \in \Omega$ must be solved for the microscopic chemical potential $u = u(t, x, y)$ and the microscopic phase-field $\phi = \phi(t, x, y)$ on the time-space cylinder $I_{t_{\text{end}}} \times \{x\} \times Y$, see Figure 4.2. It depends on the macroscopic temperature $T = T(t, x)$, hence the microscopic model is a parametrized model, where the macroscopic temperature represents the varying parameter. The phase-field ϕ varies smoothly from its liquid value -1 to its solid value 1 . The equations are supplemented by

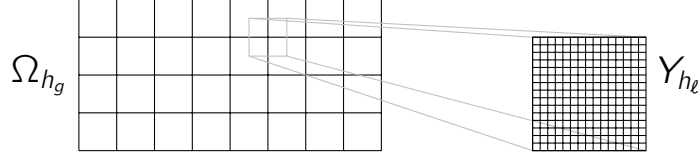


Figure 4.2: The macroscopic Ω_{h_g} and the local microscopic grid Y_{h_l} .

Y -periodic boundary conditions for u and ϕ and initial conditions $u_0(y)$ for the chemical potential and $\phi_0(y)$ for the phase-field which are independent of the macroscopic grid point. The domain Y is a rectangle in \mathbb{R}^2 . The function $p(\phi) = \frac{1}{2}(1 - \phi^2)^2$ is a double-well potential with minima zero in ± 1 . The function q triggers the dendritic growth and realizes the deviation from the equilibrium melting point,

$$q(T, u, \phi) = 1.2(1 - \phi^2) \cdot \arctan\left(\frac{\xi}{1.2}(-u - T)\sigma_0\left(1 + \sigma_1\left(-1 + 2\left(2\frac{\|\nabla_y \phi\|_4^4}{\|\nabla_y \phi\|_2^4} - 1\right)\right)\right)\right). \quad (4.5)$$

The constants α , ξ , σ_0 and σ_1 are specified in Subsection 4.4.

The model does not include stochastic perturbations in the equations for the chemical potential. Such perturbations could trigger the sidebranching into dendrites of second and higher order [41]. Therefore, the numerical results will only show four primary dendrites. In fact, the model is intended as a "simple" model case for the reduction scheme to be developed in Subsection 4.3.

4.2.3 The discretization of the two-scale model

The macroscopic as well as the microscopic problems are discretized with respect to the time by the Crank-Nicolson-method with a uniform time-step size $k_t := t_{\text{end}}/K_t$ with total step number K_t introducing the discrete time instants $t_n := nk_t, n = 0, \dots, K_t$. With respect to the spatial discretization, standard second-order finite differences are used on uniform rectangular grids Ω_{h_g} and Y_{h_l} , where $h_g = H_\ell h_l$ is the macroscopic and h_l the microscopic mesh-size. Furthermore introduced is $\phi^n(y)$ as approximation of $\phi(t_n, x, y)$, where the x -dependency is suppressed for ease of the notation of the microscopic problem, and similarly $u^n(y)$, $T^n(x)$, $\overline{\phi^n(x)}^Y$ for $x = (x_0, x_1) \in \Omega_{h_g}, y = (y_0, y_1) \in Y_{h_l}$. The discrete phase-field equation reads

$$\begin{aligned} & \left(1 + \frac{2k_t}{\alpha h_l^2} + \frac{6k_t}{\alpha \xi^2} (\phi^n(y))^2\right) \phi^{n+1}(y) - \frac{k_t}{2\alpha h_l^2} \sum_{\bar{y} \in \bar{Y}_{h_l}(y)} \phi^{n+1}(\bar{y}) \\ &= \left(1 - \frac{2k_t}{\alpha h_l^2} + \frac{2k_t}{\alpha \xi^2} (1 + 2(\phi^n(y))^2)\right) \phi^n(y) + \frac{k_t}{2\alpha h_l^2} \sum_{\bar{y} \in \bar{Y}_{h_l}(y)} \phi^n(\bar{y}) + \\ &+ \frac{k_t}{\alpha \xi^2} q(T^n, u^n(y), \phi^n(y)), \end{aligned} \quad (4.6)$$

with the central node $y = (y_0, y_1)$ and its neighbors $\bar{Y}_{h_l}(y) = \{(y_0 + h_l, y_1), (y_0 - h_l, y_1), (y_0, y_1 + h_l), (y_0, y_1 - h_l)\}$, the discrete equation for the chemical potential

$$\begin{aligned} & \left(1 + \frac{2k_t}{h_l^2}\right) u^{n+1}(y) - \frac{k_t}{2h_l^2} \sum_{\bar{y} \in \bar{Y}_{h_l}(y)} u^{n+1}(\bar{y}) \\ &= \left(1 - \frac{2k_t}{h_l^2}\right) u^n(y) + \frac{k_t}{2h_l^2} \sum_{\bar{y} \in \bar{Y}_{h_l}(y)} u^n(\bar{y}) + (\phi^{n+1}(y) - \phi^n(y)), \end{aligned} \quad (4.7)$$

and the discrete equation for the temperature

$$\begin{aligned} & \left(1 + \frac{2k_t K}{h_g^2}\right) T^{n+1}(x) - \frac{k_t K}{2h_g^2} \sum_{\bar{x} \in \bar{X}_{h_g}(x)} T^{n+1}(\bar{x}) \\ &= \left(1 - \frac{2k_t K}{h_g^2}\right) T^n(x) + \frac{k_t K}{2h_g^2} \sum_{\bar{x} \in \bar{X}_{h_g}(x)} T^n(\bar{x}) + \left(\overline{\phi^{n+1}(x)}^Y - \overline{\phi^n(x)}^Y\right), \end{aligned} \quad (4.8)$$

with the central node $x = (x_0, x_1)$ and its neighbors $\bar{X}_{h_g}(x) = \{(x_0 + h_g, x_1), (x_0 - h_g, x_1), (x_0, x_1 + h_g), (x_0, x_1 - h_g)\}$. Stability considerations resp. linearization arguments yield the quadratic-term on the left-hand side of discretization (4.6), resulting from the approximation

$$\begin{aligned} \rho'(\phi) &\approx 2 \left((\phi^{n+1})^3 - \phi^n \right) \\ &\approx 2 \left((\phi^n)^3 + 3(\phi^n)^2 (\phi^{n+1} - \phi^n) - \phi^n \right) \\ &= 2 \left(3(\phi^n)^2 \phi^{n+1} - 2(\phi^n)^2 - \phi^n \right). \end{aligned} \quad (4.9)$$

The time discretization decouples the macroscopic and the microscopic problems: at first, in each time step, all microscopic problems are solved (at first the phase-field equation is solved and afterwards the equation for the chemical potential) with temperature data from the previous time step, then the macroscopic problem is solved.

As the microscopic model is reduced, a compactly written vector-matrix formulation is provided in the following, which is more accessible than the above detailed formulation. For this define $H := |Y_{h_\ell}|$ as the (high) dimension of the field variables of the microscopic model and introduce the vectors of degrees of freedom (DOF) $\underline{\phi}_H^n := (\phi^n(y))_{y \in Y_{h_\ell}}$, $\underline{u}_H^n := (u^n(y))_{y \in Y_{h_\ell}} \in \mathbb{R}^H$ assuming a suitable enumeration of Y_{h_ℓ} . First, for each given macroscopic temperature $T = T^n(x)$, $x \in \Omega_{h_g}$ the phase-field is updated by determining $\underline{\phi}_H^{n+1}$ from

$$\underline{L}_{\phi, H}(\underline{\phi}_H^n) \underline{\phi}_H^{n+1} = \underline{r}_H(\underline{\phi}_H^n, \underline{u}_H^n, T), \quad (4.10)$$

where $\underline{L}_{\phi, H} \in \mathbb{R}^{H \times H}$ is a matrix and $\underline{r}_H \in \mathbb{R}^{H \times 1}$ a vector which depend nonlinearly on their arguments. Then, the chemical potential \underline{u}_H^{n+1} is computed by

$$\underline{L}_{u, H} \underline{u}_H^{n+1} = \underline{F}_H \underline{u}_H^n + (\underline{\phi}_H^{n+1} - \underline{\phi}_H^n), \quad (4.11)$$

where $\underline{L}_{u, H}, \underline{F}_H \in \mathbb{R}^{H \times H}$ are constant matrices. Hence, the potential problem will be simple to reduce, the phase-field model, however, will require more complex treatment.

4.3 The reduced two-scale model

This subsection develops a reduced version of the detailed two-scale model. Because the detailed macroscopic problem is by far not as hard to solve as the detailed microscopic problems, only the microscopic problems are reduced. Therefore, the reduced two-scale model consists of a detailed macroscopic problem for the temperature and reduced microscopic problems for the chemical potential and the phase-field.

The reduced model must account for the parameter dependency in the microscopic model (via the macroscopic temperature T in each point $x \in \Omega_{h_g}$), the nonlinearities

on both sides of the microscopic phase-field equation (4.6) or rather (4.10), the time-dependency, i.e. good approximation of complete trajectories, a high solution variability as is expected in evolution of phase boundaries, and the coupling of the microscopic equations for the potential and the phase-field. To consider this, a POD for the trajectory treatment, EIM for the nonlinearities and parametrization and a partitioning approach to account for different solution regimes will be applied.

As typical in parametrized model reduction procedures, the overall reduction process consists of an offline and an online phase. In the offline phase, the reduced basis and further quantities are precomputed, this phase is accepted to be costly, but only performed once. The online phase of the reduced model then will be of low order complexity and allows the reduced scheme to be used rapidly and multiply, i.e. for all macroscopic nodes and all times.

4.3.1 The offline phase

In the offline phase, all data required in the online phase has to be computed. Therefore, the following steps are processed.

1. Solve the detailed two-scale model and collect snapshots
 - (a) of the microscopic phase-field solution $\underline{\phi}_H^{n+1}$ of (4.6)/(4.10) to the set Π_ϕ ,
 - (b) of the microscopic solution of the chemical potential \underline{u}_H^{n+1} of (4.7)/(4.11) to the set Π_u ,
 - (c) and of the right hand side $\underline{r}_{\phi,H}^n = \underline{r}_{\phi,H}^n(\underline{\phi}_H^n, \underline{u}_H^n, T^n)$ of equation (4.6)/(4.10) to the set Π_r .

The choice of macroscopic nodes to draw trajectories from, and the sampling step width of the trajectories will be varied and specified in the experiments.

2. Construct two reduced bases by POD:
 - (a) $\Phi_\phi = \{\varphi_{\phi,1}, \dots, \varphi_{\phi,N_\phi}\} \subset \text{span}(\Pi_\phi)$ with size $N_\phi = |\Phi_\phi|$,
 - (b) and $\Phi_u = \{\varphi_{u,1}, \dots, \varphi_{u,N_u}\} \subset \text{span}(\Pi_u)$ with size $N_u = |\Phi_u|$.

For $\Delta = \phi, u$ and $i = 1, \dots, N_\Delta$, the N_Δ vectors $\varphi_{\Delta,i}$ are exactly the eigenvectors of the correlation operator of Π_Δ corresponding to the N_Δ largest eigenvalues. If the eigenvalues λ_i are sorted decreasingly, then N_Δ is the smallest number fulfilling the condition $\sum_{i=1, \dots, N_\Delta} \lambda_i \geq (1 - \epsilon_{POD}) \sum_{i=1, \dots, |\Pi_\Delta|} \lambda_i$ with a tolerance $0 < \epsilon_{POD} < 1$. The reader is referred to [35, 58] for further details on POD.

3. Perform the offline phase of the Empirical Interpolation Method to generate an approximation of the microscopic phase-field model. Use as training data the snapshot set Π_r , define the tolerance $0 < \epsilon_{EI} < 1$, determine the indices $Y_M \subset Y_H$ of the magic points and generate the collateral basis Φ_ϕ^{EI} , cf. [14, 18]: training snapshots $\underline{L}_{\phi,H} \underline{\phi}_H^{n+1} - \underline{r}_H$ as required for the considered model are always zero, therefore snapshots of only \underline{r}_H are used. Furthermore, with respect to the five-point-stencil discretizing the spatial derivatives, determine the indices $Y_{N_M} \subset Y_H$ of the magic points' neighbors, but only of those neighbors which are not magic points themselves, i.e. $Y_M \cap Y_{N_M} = \emptyset$. Define $Y_M^* = Y_M \cup Y_{N_M}$ and introduce an enumeration by $Y_M^*(i) = Y_M(i)$ for all $i = 1, \dots, |Y_M|$ and $Y_M^*(i) = Y_{N_M}(i - |Y_M|)$ for all $i = |Y_M| + 1, \dots, |Y_M| + |Y_{N_M}|$. The online phase of the Empirical Interpolation will be involved in the next subsections.
4. Determine the reduced operators required for the solution of the reduced model;

details on the operators are described in the following.

Although these offline quantities comprise two reduced bases and the interpolation points, this set of quantities is denoted a *reduced basis set* $\mathcal{B} = \{\Phi_\phi, \Phi_u, Y_M, Y_M^*\}$.

Numerical results presented in Subsection 4.4 indicate that it is not practical to use only one basis set. Aim of the reduced model is on the one hand to obtain a solution in much less online time than needed for the detailed model, but, what is also important, on the other hand the reduced solution should be a good approximation of the detailed one. Therefore, as always, it is a competition between accuracy and cost of computation. Accuracy increases with increasing numbers N_ϕ , N_u and $|Y_M|$. Contrary to this relation, speed of computation increases with decreasing numbers N_ϕ , N_u , $|Y_M|$ and $|Y_{N_M}|$. In order to keep those numbers low but still to gain accurate results, it is advisable to use a partitioning approach to obtain multiple basis sets. Such procedures have been developed and applied successfully in literature. For example, partitionings of the input parameter domain can be realized, e.g. via the hp-RB [25, 26, 27] or P-partitioning [30] approach. A partitioning of the time-axis can be applied to reduce complexity over time [17]. Also implicit partitioning approaches have been developed [47, 59] based on unsupervised learning approaches.

In this study, a problem-specific feature extraction is used to partitioning the solution space. This is a new conceptual contribution. The main principle of the partitioning strategy is in the offline phase to subdivide the set of snapshots into subsets with respect to a certain criterion and to construct from each subset one basis set. In the online phase a reduced solution is searched for in the span of a certain basis set if the solution of the previous time-step fulfills the distinguishing condition of that special basis set. The utilized criterion is the volume of the solid phases: the number of primary dendrites and their growth directions are prescribed by parameters, which as well as the initial condition are the same for all the microscopic problems, altogether they imply that microscopic solutions with similar solid phases' volumes also have similar shapes.

The proposed partitioning scheme is more suitable to the present application than the other schemes described above: a partitioning of the input parameter domain is inappropriate because the input parameter changes in time, therefore the input parameter domain consists of trajectories; a partitioning with respect to the time is unsuitable because the growth rate of a dendrite depends on the input parameter and therefore not explicitly on the time; it is the additional prior knowledge of volume growth that draws a distinction to unsupervised clustering procedures: as including prior knowledge is important in machine learning, the volume size is used as a distinctive feature characterizing solution regimes.

In the following the construction of the $N_B \in \mathbb{N} \setminus \{0\}$ basis sets $\mathcal{B}_1, \dots, \mathcal{B}_{N_B}$ in the offline phase is explained. For every snapshot S_H that is collected while solving the detailed model, the corresponding volume $v_H(S)$ of the solid phase is determined, that is

$$v_H(S) = v_H(S(\phi_H^{n+1})) = \frac{1}{2} + \frac{1}{2H} \sum_{(y_0, y_1) \in Y_{n_\ell}} \phi_H^{n+1}(y_0, y_1). \quad (4.12)$$

Say $N_{S,\phi}$ is the total number of snapshots of the phase-field, $N_{S,u}$ of the chemical potential and $N_{S,r}$ of the right hand side. The volumes for the snapshot set Π_ϕ are ordered by size, the minimum $v_0 = \min_{S \in \Pi_\phi} v_H(S)$ as well as the maximum volume $v_{N_B} = \max_{S \in \Pi_\phi} v_H(S)$ are determined, and for $i = 1, \dots, N_B - 1$ value v_i is equal to the $i \cdot \lfloor \frac{N_{S,\phi}}{N_B} \rfloor$ -th smallest volume. Then each of the snapshot-sets Π_ϕ , Π_u and Π_r is subdivided into N_B subsets

$\Pi_{\phi,1}, \dots, \Pi_{\phi,N_B}, \Pi_{u,1}, \dots, \Pi_{u,N_B}$ and $\Pi_{r,1}, \dots, \Pi_{r,N_B}$ according to the following criterion

$$\Pi_{\Delta,i} = \{S \in \Pi_{\Delta} \mid v_{i-1} - \epsilon_B(v_{i-1} - v_{i-2}) \leq v_H(S) \leq v_i + \epsilon_B(v_{i+1} - v_i)\} \quad (4.13)$$

for $i = 1, \dots, N_B$ and $\Delta = \phi, u, r$, with $v_{-1} = v_0$ and $v_{N_B+1} = v_{N_B}$ and $0 \leq \epsilon_B < 1$. If ϵ_B is zero, then all the subsets $\Pi_{\phi,i}$ have the same cardinal number. If ϵ_B is larger than zero, then the intersection of two subsets $\Pi_{\phi,i}$ and $\Pi_{\phi,i+1}$ might contain more than only one snapshot. Allowing intersections pursues the objective to guarantee smooth transitions from one basis set to a neighboring one in the online phase. Finally, for $i = 1, \dots, N_B$ the basis sets $\mathcal{B}_i = (\Phi_{\phi,i}, \Phi_{u,i}, Y_{M,i}, Y_{M,i}^*)$ are determined according to the steps 2.-4. from the subsets of snapshots $\Pi_{\phi,i}, \Pi_{u,i}$ and $\Pi_{r,i}$. The reason for the subdivision of the snapshots into subsets with similar cardinal numbers is the expectation that this results in similar cardinal numbers $N_{\phi}, N_u, |Y_M|$ and $|Y_M^*|$ for all the basis sets $\mathcal{B}_i, i = 1, \dots, N_B$. If the sizes of all basis sets are similar, then not only the accuracy but also the cost of computation is on the same level for the whole set of basis sets.

How the N_B basis sets $\mathcal{B}_1, \dots, \mathcal{B}_{N_B}$ are used to construct the reduced solutions in the online phase is explained in this paragraph. In the beginning of every time-step $n+1$ the new i.e. appropriate basis set is determined, that is at first the volume $v_{N_{\phi}}^n$ of the solid phase is determined, for the old i.e. current basis set \mathcal{B}_i that is

$$v_{N_{\phi}}^n = \frac{1}{2} + \frac{1}{2H} (1 \dots 1) \underline{\Phi}_{\phi,i} \underline{\phi}_{N_{\phi},i}^n, \quad (4.14)$$

and if $v_{j-1} < v_{N_{\phi}}^n \leq v_j$ then \mathcal{B}_j is the appropriate basis set. Contrary to the offline phase, it is $v_0 = -\infty$ and $v_{N_B} = \infty$ in the online phase in order to capture all possible volume sizes, including those exceeding the training data range. If the current and the appropriate basis set differ, then the reduced solutions of the previous time-step n are orthogonally projected into the span of the appropriate basis set, that is

$$\underline{\phi}_{N_{\phi},j}^n = \underline{\Phi}_{\phi,j}^{\top} \underline{\Phi}_{\phi,i} \underline{\phi}_{N_{\phi},i}^n, \quad \underline{u}_{N_u,j}^n = \underline{\Phi}_{u,j}^{\top} \underline{\Phi}_{u,i} \underline{u}_{N_u,i}^n, \quad (4.15)$$

where for $\Delta = \phi, u$ and $\ell = 1, \dots, N_B$ the columns of the matrix $\underline{\Phi}_{\Delta,\ell} \in \mathbb{R}^{H, N_{\Delta,\ell}}$ are equal to the DOF-vectors of the POD-basis $\Phi_{\Delta,\ell}$. Completing this, the current basis set turns from \mathcal{B}_i to the appropriate \mathcal{B}_j .

If a reduced model with multiple basis sets instead of only one is used, then what must be determined additionally in the online phase is only the appropriate basis set and potentially the projection of the phase-field and the chemical potential, where the projection matrices $\underline{\Phi}_{\Delta,i\pm 1}^{\top} \underline{\Phi}_{\Delta,i}$ are precomputed in the offline phase. The volumes of the solid phases are computed anyway because they are parameters of the macroscopic problem.

4.3.2 The reduced model for the chemical potential

In the online phase, the reduced chemical potential $\underline{u}_{N_u}^{n+1} \in \mathbb{R}^{N_u,1}$ is determined by the following equation, which is simply a Galerkin projection of (4.11), i.e. multiplication by $\underline{\Phi}_u^{\top}$ from the left and inserting the reduced quantities. As the system matrix is constant, the system can be inverted resulting in

$$\underline{u}_{N_u}^{n+1} = (\underline{\Phi}_u^{\top} \underline{L}_{u,H} \underline{\Phi}_u)^{-1} \underline{\Phi}_u^{\top} \left(\underline{E}_H \underline{\Phi}_u \underline{u}_{N_u}^n + \underline{\Phi}_{\phi} \left(\underline{\phi}_{N_{\phi}}^{n+1} - \underline{\phi}_{N_{\phi}}^n \right) \right), \quad (4.16)$$

where $\underline{\Phi}_u \in \mathbb{R}^{H, N_u}$ is the matrix with columns equal to the DOF-vectors of the current appropriate POD-basis Φ_u , and $\underline{\Phi}_\phi \in \mathbb{R}^{H, N_\phi}$ is the matrix with columns equal to the DOF-vectors of the current appropriate POD-basis Φ_ϕ .

The matrix operating on $\underline{u}_{N_u}^n$ as well as the matrix operating on the difference $\underline{\phi}_{N_\phi}^{n+1} - \underline{\phi}_{N_\phi}^n$ are constant for all times: they are precomputed in the offline phase. Consequently, what remains to be computed in the online phase, in order to determine the reduced solution $\underline{u}_{N_u}^{n+1}$ of the chemical potential, are two small matrix vector products only.

4.3.3 The reduced model for the phase-field

The standard Empirical Interpolation system approximating the detailed system (4.10) for the phase-field reads

$$\underline{\Phi}_\phi^{EI} \underline{L}_{\phi, H}(\underline{\phi}_{N_\phi}^n)_{Y_M} \underline{\Phi}_\phi \underline{\phi}_{N_\phi}^{n+1} = \underline{\Phi}_\phi^{EI} \underline{r}_H(\underline{\phi}_{N_\phi}^n, \underline{u}_{N_u}^n, T)_{Y_M}, \quad (4.17)$$

with $\underline{L}_{\phi, H}(\underline{\phi}_{N_\phi}^n)_{Y_M} \in \mathbb{R}^{|Y_M|, H}$ and $\underline{r}_H(\underline{\phi}_{N_\phi}^n, \underline{u}_{N_u}^n, T)_{Y_M} \in \mathbb{R}^{|Y_M|, 1}$, where the index Y_M denotes that only the rows belonging to the 'magic points' indices are considered. This system is not suitable because a high-dimensional system must be solved in the online phase and, furthermore, it is unknown whether the system is of full rank.

Therefore, $\underline{\Phi}_\phi^{EI}$ is eliminated from the equation by a suitable biorthogonal matrix multiplication, resulting in

$$\underline{L}_{\phi, Y_M}(\underline{\phi}_{N_\phi}^n) \underline{\phi}_{N_\phi}^{n+1} = \underline{r}_{Y_M}(\underline{\phi}_{N_\phi}^n, \underline{u}_{N_u}^n, T), \quad (4.18)$$

with a matrix $\underline{L}_{\phi, Y_M}(\underline{\phi}_{N_\phi}^n) \in \mathbb{R}^{|Y_M|, N_\phi}$, a vector $\underline{r}_{Y_M}(\underline{\phi}_{N_\phi}^n, \underline{u}_{N_u}^n, T) \in \mathbb{R}^{|Y_M|, 1}$ and a scalar T which is the detailed macroscopic temperature solution of time-step n at the location of the microscopic problem in the macroscopic domain. This system is suitable because it is low-dimensional. It is solved for $\underline{\phi}_{N_\phi}^{n+1}$ by a Least-Squares procedure via the pseudoinverse, as it will be overdetermined in general.

The matrix and the vector are defined as follows

$$\begin{aligned} \underline{L}_{\phi, Y_M}(\underline{\phi}_{N_\phi}^n) &= \underline{L}(\underline{\phi}_{N_\phi}^n) \underline{\tau}_{Y_M^*} \underline{\Phi}_\phi, \\ \underline{r}_{Y_M}(\underline{\phi}_{N_\phi}^n, \underline{u}_{N_u}^n, T^n) &= \underline{R} \underline{\tau}_{Y_M^*} \underline{\Phi}_\phi \underline{\phi}_{N_\phi}^n + \hat{\underline{r}}_{Y_M}(\underline{\phi}_{N_\phi}^n, \underline{u}_{N_u}^n, T^n), \end{aligned} \quad (4.19)$$

with $\underline{L}(\underline{\phi}_{N_\phi}^n) \in \mathbb{R}^{|Y_M|, |Y_M^*|}$ defined as

$$\left(\underline{L}(\underline{\phi}_{N_\phi}^n) \right)_{i,j} = \begin{cases} 1 + \frac{2k_t}{\alpha h_\ell^2} + \frac{6k_t}{\alpha \xi^2} \left(\left(\underline{\tau}_{Y_M^*} \underline{\Phi}_\phi \underline{\phi}_{N_\phi}^n \right)_i \right)^2 & \text{for } j = i, \\ -\frac{k_t}{2\alpha h_\ell^2} & \text{if } Y_M^*(j) \text{ is a neighbor of magic point } Y_M(i), \\ 0 & \text{otherwise,} \end{cases} \quad (4.20)$$

and $\underline{R} \in \mathbb{R}^{|Y_M|, |Y_M^*|}$ defined as

$$\underline{R}_{i,j} = \begin{cases} 1 - \frac{2k_t}{\alpha h_\ell^2} + \frac{2k_t}{\alpha \xi^2} & \text{for } j = i, \\ \frac{k_t}{2\alpha h_\ell^2} & \text{if } Y_M^*(j) \text{ is a neighbor of magic point } Y_M(i), \\ 0 & \text{otherwise,} \end{cases} \quad (4.21)$$

with the restriction-matrices $\mathcal{T}_{Y_M} \in \mathbb{R}^{|Y_M|, H}$ and $\mathcal{T}_{Y_M^*} \in \mathbb{R}^{|Y_M^*|, H}$ defined as

$$\left(\mathcal{T}_{Y_M}\right)_{i,j} = \begin{cases} 1 & \text{for } j = Y_M(i), \\ 0 & \text{otherwise,} \end{cases} \quad \left(\mathcal{T}_{Y_M^*}\right)_{i,j} = \begin{cases} 1 & \text{for } j = Y_M^*(i), \\ 0 & \text{otherwise.} \end{cases} \quad (4.22)$$

and finally with

$$\begin{aligned} & \left(\hat{\mathcal{I}}_{Y_M}(\underline{\phi}_{N_\phi}^n, \underline{u}_{N_u}^n, T^n)\right)_i \\ &= \frac{4k_t}{\alpha\xi^2} \left(\mathcal{T}_{Y_M}\Phi_\phi\phi_{N_\phi}^n\right)_i^3 + q\left((\nabla_y\phi^*)_i, T^n, (\mathcal{T}_{Y_M}\Phi_u\underline{u}_{N_u}^n)_i, (\mathcal{T}_{Y_M}\Phi_\phi\phi_{N_\phi}^n)_i\right), \end{aligned} \quad (4.23)$$

where $(\nabla_y\phi^*)_i$ is the approximation of the j -th derivative of ϕ^n in the i -th magic point: without going into the details here, in order to obtain the j -th derivatives in the magic points simply a matrix-vector product must be computed, where the matrix is similar to the restriction matrix $\mathcal{T}_{Y_M^*}$ and the vector is the former reduced solution.

Many of the products of the reduced system (4.18) are precomputed in the offline phase, what still has to be computed in every time step $n+1$ in the online phase is

1. the matrix vector products of $\mathcal{T}_{Y_M}\Phi_\phi \in \mathbb{R}^{|Y_M|, N_\phi}$ and $\phi_{N_\phi}^n \in \mathbb{R}^{N_\phi, 1}$ as well as of $\mathcal{T}_{Y_M}\Phi_u \in \mathbb{R}^{|Y_M|, N_u}$ and $\underline{u}_{N_u}^n \in \mathbb{R}^{N_u, 1}$ – in order to obtain the values of ϕ and u in the magic points,
2. the matrix vector products of $A_j\mathcal{T}_{Y_M^*}\Phi_\phi \in \mathbb{R}^{|Y_M|, N_\phi}$ and $\phi_{N_\phi}^n \in \mathbb{R}^{N_\phi, 1}$ – in order to obtain the j -derivatives of ϕ in the magic points, with a suitable $A_j \in \mathbb{R}^{|Y_M|, |Y_M^*|}$,
3. the first diagonal of matrix $\underline{L}(\phi_{N_\phi}^n) \in \mathbb{R}^{|Y_M|, |Y_M^*|}$ and the product of the two matrices $\underline{L}(\phi_{N_\phi}^n) \in \mathbb{R}^{|Y_M|, |Y_M^*|}$ and $\mathcal{T}_{Y_M^*}\Phi_\phi \in \mathbb{R}^{|Y_M^*|, N_\phi}$ – in order to obtain the left-hand side matrix $\underline{L}_{\phi, Y_M}(\phi_{N_\phi}^n)$ of (4.18),
4. the product of $\underline{R}\mathcal{T}_{Y_M^*}\Phi_\phi \in \mathbb{R}^{|Y_M|, N_\phi}$ and $\phi_{N_\phi}^n \in \mathbb{R}^{N_\phi, 1}$, the vector $\hat{\mathcal{I}}_{Y_M}(\phi_{N_\phi}^n, \underline{u}_{N_u}^n, T^n) \in \mathbb{R}^{|Y_M|, 1}$, and the sum of these two vectors – in order to obtain the right hand side vector $\mathcal{I}_{Y_M}(\phi_{N_\phi}^n, \underline{u}_{N_u}^n, T^n)$ of (4.18),
5. and finally, the Least-Squares solution $\phi_{N_\phi}^{n+1} \in \mathbb{R}^{N_\phi, 1}$ of (4.18).

All of these computations for the online phase of the reduced models are completely independent of the high dimension H . The computational complexity only scales with N_ϕ , N_u , $|Y_M|$ and $|Y_M^*|$. This is true for the reduced systems, but as well the projection operations for a basis set change and the averaging procedure for coupling into the macroscopic temperature equation. Consequently, the reduced model provides an ideal offline-online decomposition.

4.4 Numerical results

In order to evaluate the reduced two-scale model's quality, this subsection presents the results of numerical computations. In particular compared are reduced to detailed numerical results. At first in order to show that the reduced model features a possible reproduction of detailed results, the detailed and the reduced solution are compared for a setting with a small time-space cylinder. In a second step, on a larger time-space cylinder, it is shown that the reduced model not only produces accurate results but also speeds up the computation significantly. And finally in a third step, generalization abilities of the reduced model are investigated.

This paragraph defines the different detailed models to be solved or to be approximated by reduced models in the following subsections. Equations (4.6)/(4.10) and (4.7)/(4.11) describe the microscopic model to be solved on the microscopic domain $Y_{h_\ell} = [0, H_\ell h_\ell]^2$ with space increment $h_\ell = 0.005$, and the macroscopic heat equation (4.8) is to be solved on the macroscopic domain $\Omega_{h_g} = [0, H_{g,1} h_g] \times [0, H_{g,2} h_g]$ with space increment $h_g = H_\ell h_\ell$. Therefore, Ω_{h_g} consists of $(H_{g,1} + 1) \cdot (H_{g,2} + 1)$ nodes, each of them governing one microscopic problem on Y_{h_ℓ} consisting of $(H_\ell + 1)^2$ nodes. The computation time is from 0 to $K_t k_t$ with time increment $k_t = 2e-6$. On the macroscopic scale, the effective heat conductivity K is larger than zero, and the boundary conditions of the heat equation are the prescribed heat fluxes

$$\frac{k_t K}{2h_g^2} \nabla T \cdot n = \begin{cases} -2c_{\text{boundary-flux}} & \text{for } x_1 = 0, \\ -c_{\text{boundary-flux}} & \text{for } x_2 = 0, \\ 0 & \text{otherwise,} \end{cases} \quad c_{\text{boundary-flux}} > 0. \quad (4.24)$$

Put more simply, two parts of the boundary have cooling conditions, and the remaining two parts are isolated. For the microscopic cell problems the boundary conditions are periodic. The initial temperature T , the initial chemical potential u and the initial phase-field ϕ are for all $x \in \Omega_{h_g}$ and for all $y \in Y_{h_\ell}$ specified as

$$\begin{aligned} T(0, x) &= -0.1, \\ u(0, x, y) &= -0.1, \\ \phi(0, x, y) &= \tanh \left(0.25 \left(\sqrt{\sum_{i=1,2} \left(\frac{1}{h_\ell} y_i - \frac{H_\ell}{2} \right)^2} - 5 \right) \right). \end{aligned} \quad (4.25)$$

By reason that the initial conditions of the microscopic unknowns u and ϕ are independent of their location on the macroscopic domain, they are equal for all the microscopic problems. Furthermore, they (in combination with the initial temperature condition) imply that, initially, a small solid kernel occupies the center of every microscopic domain and that each kernel is surrounded by an undercooled melt. The microscopic physical parameters are specified as $\alpha = 5$, $\xi = 0.01$, $\sigma_0 = 5000$ and $\sigma_1 = 0.5$. Consequently, the different models to be solved differ only in the following variables: the number of microscopic nodes $H_\ell > 0$ in both dimensions, the number of macroscopic nodes $H_{g,1} > 0$ in the first and $H_{g,2} > 0$ in the second dimension, the number of time-steps $K_t > 0$, the macroscopic boundary temperature outflow-constant $c_{\text{boundary-flux}} > 0$ and the macroscopic heat conductivity $K > 0$.

A reduced solution's accuracy is estimated by comparing its macroscopic temperature solution T_{red} to the detailed method's temperature solution T_{det} . The error $\Delta T := |T_{\text{red}} - T_{\text{det}}|$ is measured in the discrete L_2 - and L_∞ -norms on the discrete macroscopic space domain Ω_{h_g} or on the whole discrete time-space cylinder $Q_{k_t, h_g} = I_{t_{\text{end}}, k_t} \times \Omega_{h_g}$:

$$\begin{aligned} \|\Delta T(t_n, \cdot)\|_{\Omega, 2} &= \sqrt{\frac{1}{|\Omega_{h_g}|} \sum_{x \in \Omega_{h_g}} |\Delta T(t_n, x)|^2}, \\ \|\Delta T(\cdot, \cdot)\|_{Q, 2} &= \sqrt{\frac{1}{N+1} \sum_{n=0}^N \|\Delta T(t_n, \cdot)\|_{\Omega, 2}^2}, \\ \|\Delta T(t_n, \cdot)\|_{\Omega, \infty} &= \max_{x \in \Omega_{h_g}} |\Delta T(t_n, x)|, \\ \|\Delta T(\cdot, \cdot)\|_{Q, \infty} &= \max_{n=0, \dots, N} \|\Delta T(t_n, \cdot)\|_{\Omega, \infty}. \end{aligned} \quad (4.26)$$

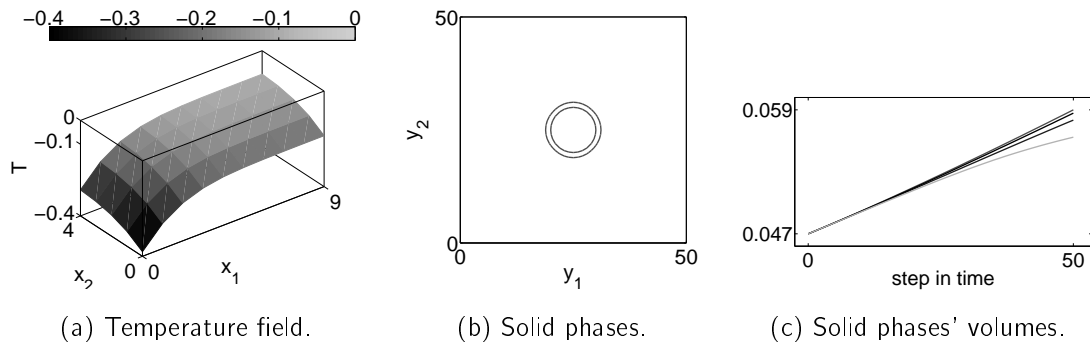


Figure 4.3: Results of the detailed two-scale model on the small time-space cylinder. Figure (a) depicts the macroscopic temperature field in the end. Figure (b) presents the initial (inner circle) and the final solid phase in the macroscopic node $(0,0)$. Figure (c) illustrates the evolution of the volumes of the solid phases in the macroscopic corner-nodes $(0,0)$, $(0,4)$, $(9,0)$ and $(9,4)$, listed from largest to smallest volume.

Unfortunately, a small temperature-error is only a necessary but not a sufficient condition for a good reduced approximation of the detailed microscopic solution. Therefore, if a reduced solution with a small temperature-error exists, then also the errors of the microscopic reduced solutions are measured in the discrete L_∞ -/ L_2 -norm in the discrete microscopic time-space cylinder $Q^* = I_{t_{\text{end}}, k_t} \times \Omega_{h_g}^* \times Y_{h_\ell}$, where $\Omega_{h_g}^*$ represents only the four nodes in the corners of the macroscopic domain, which are $(0,0)$, $(H_{g,1}, 0)$, $(0, H_{g,2})$ and $(H_{g,1}, H_{g,2})$. Evaluating all microscopic solutions would require an enormous amount of memory, therefore only the solutions in the corners are evaluated. Furthermore, in the subsections 4.4.2 and 4.4.3 with large time-space cylinders, the microscopic solutions are evaluated only every 50 steps in time. Still, this evaluation-strategy seems not to be too unreasonable because, due to the macroscopic boundary conditions, macroscopic corner node $(0,0)$ records the lowest and $(H_{g,1}, H_{g,2})$ the highest temperature in every time-step, and therefore the microscopic solutions characterized by the largest and the smallest dendrite are evaluated. The two remaining corner nodes represent dendrites in between.

4.4.1 Results on a small time-space cylinder

The detailed two-scale model to be solved in this subsection is completed by the following set of parameters: $H_\ell = 50$, $H_{g,1} = 10$, $H_{g,2} = 5$, $K_t = 50$, $c_{\text{boundary-flux}} = 2e-3$ and $K = 2000$. This model-setting is designed in order to test only whether the reduced model is capable of reproducing detailed results. The other important feature of reduced models, the increase of computational speed is, alongside of accuracy of course, a topic of the next subsection. Figure 4.3 illustrates the detailed model's macroscopic temperature solution, its microscopic phase-field solution in the macroscopic node $(0,0)$ and the evolutions of the volumes of the solid phases in the macroscopic corners nodes.

The reduced models to be evaluated in the following are constructed from snapshots produced by the detailed solution with snapshot-time-increment $s_t = 1$, that is every microscopic solution participates in their construction. For 50 microscopic problems and 50 steps in time this results in 2500 snapshots of the phase-field, of the chemical potential and of the right-hand side.

$(\epsilon_{POD}, \epsilon_{EI})$	N_ϕ	N_u	$ Y_M $	$ Y_M^* $	$\ \Delta T\ _{Q,\infty}$	$\ \Delta T\ _{Q,2}$
(1e-4, 1e-4)	2	3	14	46	3.38e-3	1.96e-3
(1e-5, 1e-5)	2	4	23	58	4.03e-3	2.78e-3
(1e-6, 1e-6)	3	5	28	63	2.58e-3	5.94e-4
(1e-10, 1e-10)	9	14	58	112	1.20e-5	2.41e-6
(1e-14, 1e-4)	21	30	14	46	7.81e-2	7.13e-2
(1e-14, 1e-5)	21	30	23	58	1.32e-7	3.34e-8
(1e-14, 1e-6)	21	30	28	63	2.69e-7	6.31e-8
(1e-14, 1e-10)	21	30	58	112	1.34e-7	1.90e-8
(1e-14, 1e-14)	21	30	114	251	2.35e-8	4.10e-9

Table 4.1: Results of reduced two-scale models on the small time-space cylinder. The reduced models are characterized by one basis set and varying tolerances ϵ_{POD} and ϵ_{EI} .

Table 4.1 presents results for reduced models consisting of one basis set only for varying tolerances ϵ_{POD} and ϵ_{EI} . For a diminishing ϵ_{POD} , the tolerance that influences the construction of the POD-bases for ϕ and u , the sizes N_ϕ and N_u of the two bases Φ_ϕ and Φ_u increase, of course. Certainly as well, for a diminishing ϵ_{EI} the number of the magic points $|Y_M|$ increases. Also increasing is the number $|Y_M^*|$: for larger tolerances it is nearly a factor of five in $|Y_M|$ versus $|Y_M^*|$, which is caused by the five-star finite difference discretization; for smaller tolerances many of the magic points' neighbors are magic themselves. The error results imply that it is not necessary to use tolerances ϵ_{POD} and ϵ_{EI} of the same order. But, comparing the results for $(\epsilon_{POD}, \epsilon_{EI}) = (1e-4, 1e-4)$ and $(\epsilon_{POD}, \epsilon_{EI}) = (1e-14, 1e-4)$, in order to produce accurate reduced results, the size of the POD-basis for the phase-field N_ϕ must not be larger than the number of the magic nodes $|Y_M|$. This is due to the fact that the system of linear equations (4.18) for the reduced phase-field is under-determined for $N_\phi > |Y_M|$. What is of great importance and what justifies the reduced model, is that, disregarding some insignificant deviations, for diminishing tolerances the errors decrease: the reduced model is capable of at least reproducing the detailed macroscopic temperature solution.

Table 4.2 presents results for reduced models consisting of a variable number of basis sets and a varying tolerance ϵ_B , with smallest tolerances $\epsilon_{POD} = \epsilon_{EI} = 1e-14$. For constant ϵ_B but an increasing N_B the average sizes N_ϕ , N_u , $|Y_M|$ and $|Y_M^*|$ of the basis sets decrease, but unfortunately also the accuracy. The last observation can be explained by the constant tolerance ϵ_B : the larger the number of basis sets, the smaller the intersection of the basis sets, and therefore the larger the projection errors. Increasing ϵ_B yields an increasing accuracy. At first sight it is surprising that the error of $(N_B, \epsilon_B) = (10, 1)$ is larger than for example of $(N_B, \epsilon_B) = (2, 0.1)$, but this may explained with projection errors: in case of only a few basis sets with a small ϵ_B , the projection error may be smaller than for the case with a larger N_B and a larger ϵ_B , but in the latter case the errors add up for each change of the basis set. Still, because the error is not significantly larger for models with a larger number of basis sets, and because the online computation time decreases significantly for decreasing sizes of the basis sets, therefore it is the reduced models with multiple basis sets that are more suitable for situations with larger time-space cylinders.

As mentioned before, small temperature errors are only a necessary condition for a good reduced approximation of the detailed microscopic solution. Therefore, Table 4.3

(N_B, ϵ_B)	N_ϕ	N_u	$ Y_M $	$ Y_M^* $	$\ \Delta T\ _{Q,\infty}$	$\ \Delta T\ _{Q,2}$
(1, -)	21	30	114	251	2.35e-8	4.10e-9
(2, 0.1)	16.50	24.00	93.50	212.00	5.53e-8	2.24e-8
(4, 0.1)	13.75	19.50	81.00	174.75	2.78e-7	7.68e-8
(10, 0)	10.90	15.20	66.60	146.10	1.86e-6	1.15e-6
(10, 0.1)	11.30	15.50	68.70	151.20	3.92e-7	1.30e-7
(10, 0.2)	11.60	15.90	69.90	153.60	2.51e-7	6.28e-8
(10, 0.5)	12.50	17.50	74.80	163.50	1.34e-7	5.50e-8
(10, 1)	13.80	19.30	80.90	178.40	8.60e-8	4.30e-8
(20, 0.1)	10.10	13.95	58.75	128.25	2.98e-6	1.43e-6

Table 4.2: Results of reduced two-scale models on the small time-space cylinder. The reduced models are characterized by $\epsilon_{POD} = \epsilon_{EI} = 1e-14$, a varying number of basis sets N_B and a varying tolerance ϵ_B . If a reduced model consists of more than one basis set, then the numbers N_ϕ , N_u , $|Y_M|$ and $|Y_M^*|$ present the average sizes of all basis sets.

$(N_B, \epsilon_{POD}, \epsilon_{EI})$	$\ \Delta T\ _{Q,\infty}$	$\ \Delta T\ _{Q,2}$	$\ \Delta \phi\ _{Q^*,\infty}$	$\ \Delta \phi\ _{Q^*,2}$	$\ \Delta u\ _{Q^*,\infty}$	$\ \Delta u\ _{Q^*,2}$
(1, 1e-5, 1e-5)	4.03e-3	2.78e-3	2.14e-2	5.82e-3	1.27e-2	5.88e-3
(1, 1e-14, 1e-5)	1.32e-7	3.34e-8	4.11e-6	1.72e-7	3.73e-6	1.38e-7
(1, 1e-14, 1e-14)	2.35e-8	4.10e-9	3.41e-6	8.69e-8	2.12e-6	5.54e-8
(2, 1e-14, 1e-14)	5.53e-8	2.24e-8	2.37e-6	1.27e-7	1.30e-6	9.99e-8
(4, 1e-14, 1e-14)	2.78e-7	7.68e-8	3.52e-6	4.82e-7	2.47e-6	4.54e-7
(10, 1e-14, 1e-14)	3.92e-7	1.30e-7	7.82e-6	7.51e-7	5.60e-6	7.26e-7
(20, 1e-14, 1e-14)	2.98e-6	1.43e-6	1.81e-5	2.77e-6	1.02e-5	2.73e-6

Table 4.3: Results of reduced two-scale models on the small time-space cylinder. The reduced model is characterized by varying parameters N_B , ϵ_{POD} and ϵ_{EI} . In case of multiple basis sets it is $\epsilon_B = 0.1$.

documents the errors of the microscopic solutions for some reduced models: as could be expected in view of the excellent overall macroscopic temperature approximation, the tighter the tolerances the smaller also the microscopic errors.

This subsection showed that the reduced model is capable of reproducing the detailed solution. The next subsection will show that the reduced model also produces accurate results on a larger time-space cylinder. Besides that, it will also show that the reduced model can be solved much more efficiently than the detailed one.

4.4.2 Results on a large time-space cylinder

The detailed two-scale model to be solved in this subsection is completed by the parameters $H_\ell = 200$, $H_{g,1} = 20$, $H_{g,2} = 10$, $K_t = 50000$, $c_{\text{boundary-flux}} = 5e-6$ and $K = 200$. Therefore, this setting, called setting S_0 , is characterized by a larger time-space cylinder than the previous subsection's setting. Figure 4.4 illustrates the result of the detailed two-scale model. Because of the boundary conditions it is always the macroscopic corner $(0, 0)$ which records the lowest temperature and therefore the largest solid.

A reduced model is constructed from snapshots which are produced by the detailed

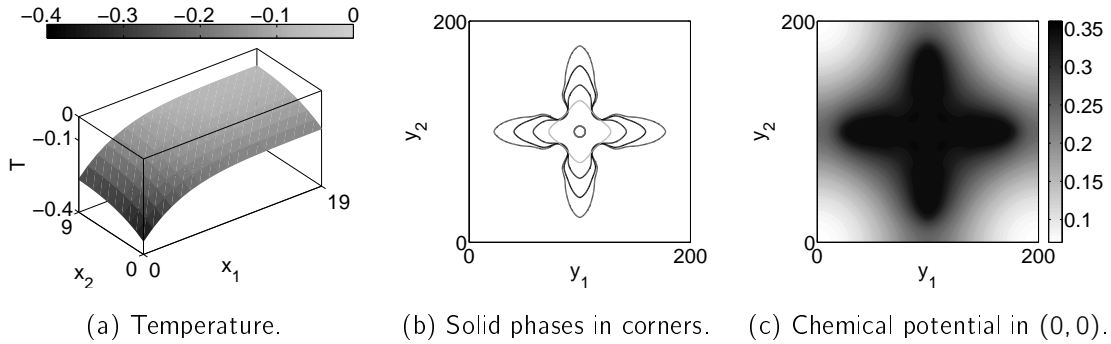


Figure 4.4: Results of the detailed two-scale model on the large time-space cylinder. Figure (a) depicts the macroscopic temperature field in the end, Figure (b) presents the initial (inner circle) and the final solid phases in the macroscopic corner nodes (0, 0) (largest), (0, 9) (second-largest), (19, 0) (third-largest) and (19, 9), and Figure (c) shows the final microscopic chemical potential in (0, 0).

model's solution. In course of the detailed simulation 10,000,000 microscopic problems are solved (50,000 time-steps times 200 macroscopic nodes). What is done in order to preselect the snapshots that are utilized in a reduced model's construction, is that the detailed two-scale model is solved adaptively. The interested reader is referred to Section 3 for details on the adaptive solution strategy. Fundamental to it is the fact that microstructures develop similar features if they are influenced by similar temperature evolutions. Consequently, a microscopic solution can be approximated by the solution of another microscopic problem if the problems are influenced by similar temperature evolutions. Exercising this observation, the strategy selects microscopic problems to be solved and approximates the remaining problems' solutions.

The applied adaptive strategy is characterized by the following parameters: $\lambda = 0.1$, $\tau = 1$, $c_{\text{tol}_c} = 0.2$, $c_{\text{tol}_{r,0}} = 0$, $c_{\text{tol}_e} = 0.01$, $\text{RU} = 0$, $eC = 1$, $M_A = 2$, IT-CA, $N_A(0) = (0, 0)$, the Copy Method and a refining tolerance parameter $c_{\text{tol}_{r,1}} = 0.01$. The last parameter is straight proportional to the maximum distance of an approximated and at least one solved microscopic problem's influencing temperature evolution: the smaller it is the more microscopic problems are solved. Without going into details, the choice $c_{\text{tol}_{r,1}} = 0.01$ is a good compromise between cost of detailed offline computation and reduced online accuracy: on average 52.18 microscopic problems are solved per time-step, topping out at 77, resulting in an adaptive offline temperature solution with the errors $\|\Delta T\|_{Q,\infty} = 3.35e-4$ and $\|\Delta T\|_{Q,2} = 8.93e-5$ compared to the non-adaptive detailed solution.

The ultimate objective is to construct a (non-adaptive) reduced model which is a good approximation of the (non-adaptive) detailed model, desirably an even better approximation than the adaptive solution whose snapshots are used to construct the reduced model. Again without going into details, numerical results indicate that it is not suitable to produce snapshots with a constant time-step-increment s_t : for an oversized s_t the accuracy especially in the very beginning (due to rapid changes in the initially constant chemical potential) is weak, on the other hand the smaller s_t the more memory is needed. In fact a reasonable compromise is the increasing snapshot-increment s_t^i : until the 100-th time-step the increment is 1, then until the 200-th it is 2, until the 500-th 5, until the 1000-th 10, until the 2000-th 25, and afterwards 50. Therefore, 53974 (i.e. around 0.5% of all possibly

	detailed solution	($25, 1e-14, 1e-6$)	($25, 1e-13, 1e-6$)	($25, 1e-13, 1e-5$)	($25, 1e-12, 1e-4$)	($50, 1e-13, 1e-5$)	($100, 1e-13, 1e-5$)	($200, 1e-13, 1e-5$)
$t_{on}((0, 0))$	1595	0.73	1.27	1.46	2.61	3.57	8.14	12.66
$t_{on}((19, 0))$	1479	1.40	2.68	3.23	6.46	5.03	7.78	10.80
$t_{on}((0, 9))$	1536	0.88	1.57	1.84	3.48	3.94	7.84	10.59
$t_{on}((19, 9))$	1347	1.89	3.74	4.86	9.62	7.13	12.03	14.97
$\overline{t_{on}}$	1489.25	1.04	1.89	2.24	4.20	4.51	8.58	11.96
N_ϕ	–	81.16	60.84	60.84	48.04	49.16	41.60	36.93
N_u	–	68.04	49.12	49.12	39.32	40.46	34.86	31.25
$ Y_M $	–	124.48	124.48	89.72	58.88	70.84	59.22	51.24
$ Y_M^* $	–	304.40	304.40	254.04	194.44	216.26	191.34	172.38
$\ \Delta T\ _{Q,\infty}$	–	7.12e-6	9.02e-6	1.29e-5	1.18e-3	4.56e-5	6.08e-5	4.77e-4
$\ \Delta T\ _{Q,2}$	–	4.28e-7	1.02e-6	1.62e-6	1.52e-5	1.51e-6	2.15e-6	4.49e-6

Table 4.4: Run-time and speed-up results on the large time-space cylinder. The reduced models are characterized by the common parameter $\epsilon_B = 0.1$ and the varying parameter set $(N_B, \epsilon_{POD}, \epsilon_{EI})$. For the detailed solution the value $t_{on}(x)$ represents the time in seconds that one Intel(R) Xeon(R) CPU E7- 4830 @ 2.13GHz needs to solve the microscopic problem in the time-space cylinder $I_{t_{end}, k_t} \times \{x\} \times Y_{h_\theta}$, and $\overline{t_{on}}$ represents the average time. For the reduced solutions, which are computed on the same CPU, it is not the absolute time but the speed-up compared to the detailed solution that is presented.

computed) microscopic solutions are used to construct the reduced models presented and evaluated in the following.

Table 4.4 states the time needed to solve the microscopic problems in the macroscopic corner nodes for the detailed and some reduced models, the sizes of the basis sets and the temperature error of the reduced solutions. Certainly, the tighter the tolerances ϵ_{POD} and ϵ_{EI} and the smaller the number of basis sets, the more time is needed to solve the reduced model but also the more accurate are the solutions. A good compromise for efficiency is the reduced model consisting of 100 basis sets which was constructed with respect to the tolerances $\epsilon_{POD} = 1e-13$, $\epsilon_{EI} = 1e-5$ and $\epsilon_B = 0.1$: compared to the detailed solution the microscopic problems are solved 8.5 times faster on average but the maximum error of the temperature is only $6.08e-5$. For this reduced model Figure 4.5 illustrates how the growth of the volume of a solid phase affects the utilized basis set building the reduced solution: the larger the volume the larger the index of the utilized basis set. Also for this model Figure 4.6 depicts its solution's error compared to the non-adaptive detailed solution. The error of the temperature is small in the beginning but it increases rapidly in the very end of the time-interval. Approximately the same holds for the error of the microscopic phase-field and chemical potential in the macroscopic node $(0, 0)$. Contrary to that the errors of the smaller solids remain on nearly the same level throughout the whole time-interval. More probably than not this is due to the fact that the reduced model is constructed from

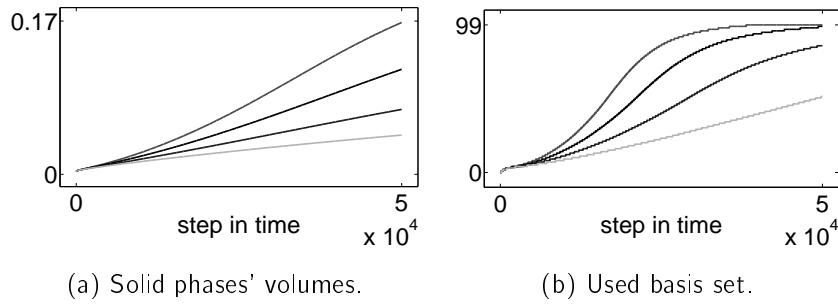


Figure 4.5: Results on the large time-space cylinder of the reduced model with parameters $N_B = 100$, $\epsilon_{POD} = 1e-13$, $\epsilon_{EI} = 1e-5$ and $\epsilon_B = 0.1$. Figure (a) illustrates the evolution of the solid phases' volumes and (b) the evolution of the utilized basis sets, both in the macroscopic corner nodes.

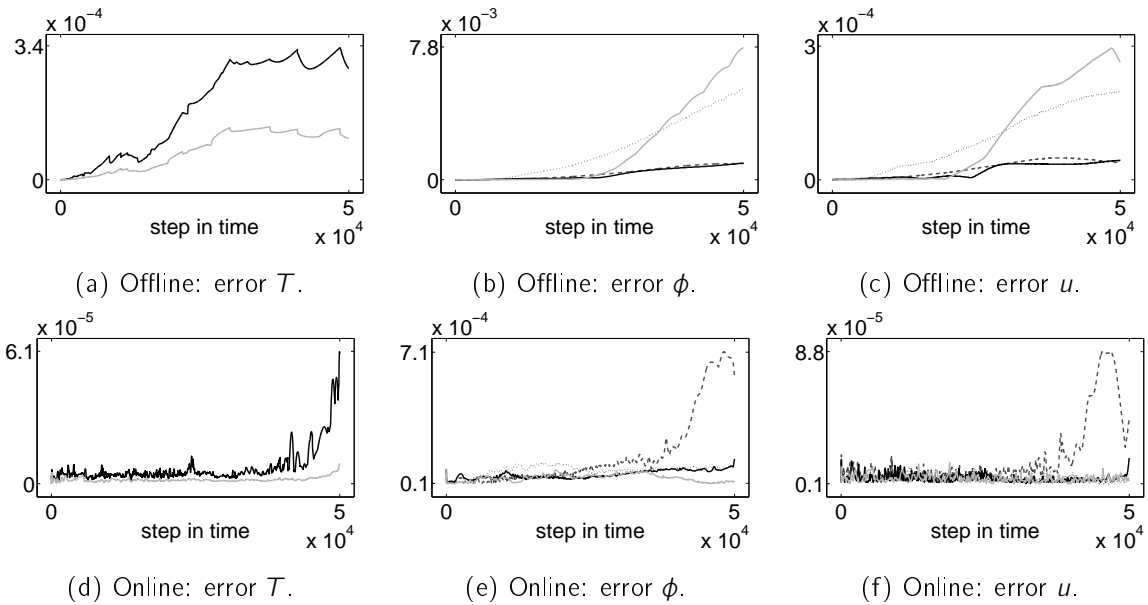


Figure 4.6: Results on the large time-space cylinder. Figures (a)-(c) depict results of the detailed adaptive model and Figures (d)-(f) results of the reduced non-adaptive model with parameters $N_B = 100$, $\epsilon_{POD} = 1e-13$, $\epsilon_{EI} = 1e-5$ and $\epsilon_B = 0.1$; the reduced model is constructed from the detailed adaptive solution. Figures (a) and (d) illustrate the respective $L_\infty(\Omega)$ - (dark-gray) and $L_2(\Omega)$ -error of the temperature solutions compared to the non-adaptive detailed solution. Figures (b) and (e) show the respective $L_\infty(Y)$ -errors of the microscopic phase-fields in the macroscopic corner nodes and (c) and (f) of the microscopic chemical potentials in the macroscopic corner nodes (0, 0) (dashed), (19, 0) (dotted), (0, 9) (dark-gray) and (19, 9).

snapshots which are mostly related to smaller solids. Nevertheless, all errors are smaller than the errors of the adaptive detailed model whose snapshots were used to construct the reduced model. Consequently, preselecting snapshots by the adaptive strategy has the desired effect: the offline phase is computed faster than without the preselection and the reduced model's accuracy is significantly greater than of the underlying adaptive detailed solution.

	(25, 1e-14, 1e-6)	(25, 1e-13, 1e-6)	(25, 1e-13, 1e-5)	(25, 1e-12, 1e-4)	(50, 1e-13, 1e-5)	(100, 1e-13, 1e-5)	(200, 1e-13, 1e-5)
Overall	14.00 h	11.72 h	7.41 h	5.18 h	4.72 h	5.24 h	7.40 h
SubdivSnaps	1.80 %	2.19 %	3.46 %	4.95 %	3.24 %	1.78 %	0.93 %
POD	15.89 %	17.73 %	28.87 %	42.97 %	14.61 %	6.16 %	2.27 %
EIM	73.95 %	72.21 %	54.91 %	35.74 %	47.40 %	32.56 %	17.12 %
MapsIntra	8.36 %	7.87 %	12.76 %	16.33 %	34.73 %	59.47 %	79.65 %
MapsInter	0.01 %	0.01 %	0.01 %	0.01 %	0.02 %	0.03 %	0.03 %

Table 4.5: Run-time on the same computer as in Table 4.4 of the offline phases of the same reduced models as in Table 4.4, that is the reduced models are characterized by the common parameter $\epsilon_B = 0.1$ and the varying parameter set $(N_B, \epsilon_{POD}, \epsilon_{EI})$. 'Overall' gives the offline phases' overall duration measured in hours, 'SubdivSnaps' refers to the subdivision of the snapshots in order to produce N_B reduced basis sets, 'POD' to the POD procedures developing the approximation spaces for the phase-field and the chemical potential, 'EIM' to the EIM addressing the non-linearity of the high-dimensional phase-field equation (4.6)/(4.10), 'MapsIntra' refers to the pre-computation of the constant mappings used in the online phase in order to compute the reduced solutions, and 'MapsInter' refers to the pre-computation of the constant projection operators for basis change in the online phase.

Table 4.5 tabulates the duration of the offline phases of the reduced models considered in the previous paragraph. Clearly, if N_B is fixed, the smaller the tolerances ϵ_{POD} of the POD-procedure and ϵ_{EI} of the EIM, the longer the duration of the offline phase. If ϵ_{POD} and ϵ_{EI} are fixed, then the larger the number N_B of the basis sets, the smaller the POD-procedures' and EIM's share in the overall duration of the offline phase, and contrariwise the larger the share of the procedure that pre-computes the constant mappings in the online phase. Since none of the offline phases takes more than 14 hours, the duration of all seven reduced models' offline phases is very acceptable.

Finally, the last Figures 4.7 and 4.8 of this subsection present results of the construction of the reduced model with parameters $N_B = 100$, $\epsilon_{POD} = 1e-13$, $\epsilon_{EI} = 1e-5$ and $\epsilon_B = 0.1$. The first figure shows that the different basis sets are responsible for different intervals of solid volumes: if a reduced solution's solid phase's volume is located in the specific interval of a basis set, then the reduced solution of the next step in time is constructed by this basis set. Furthermore, it indicates that the sizes of the basis sets are maximal for basis sets correlated to medium volume sizes, and that they differ significantly. These observations indicate that the partitioning method may be optimized. Finally, the figure describes for a sample basis set the decay of the eigenvalues of the two correlation operators of the snapshots for the phase-field and the chemical potential: those decays are rapid implying that the system comprises a strong ability to be compressed. The Figure 4.8 illustrates the differences of the basis sets: for example the location of the magic points moves from the

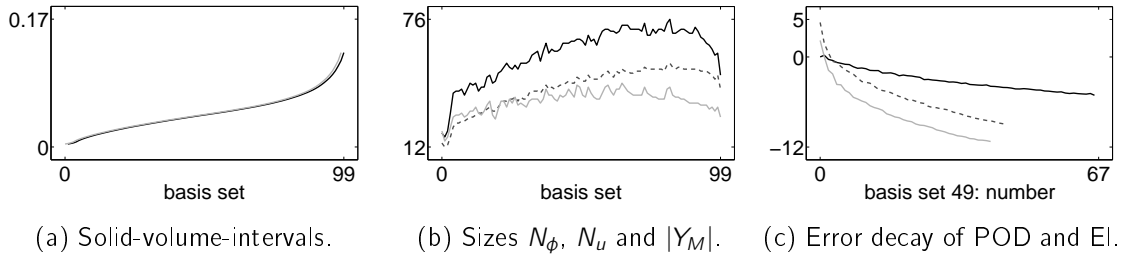


Figure 4.7: Results on the large time-space cylinder of the reduced model with parameters $N_B = 100$, $\epsilon_{POD} = 1e-13$, $\epsilon_{EI} = 1e-5$ and $\epsilon_B = 0.1$. Figure (a) depicts the maximum (light-gray) and minimum of the intervals of the volumes of the solid phases which are constructed by the different basis sets; basis set 0's minimum is zero and basis set 99 is not bounded from above, but the largest volume of the training data is only 0.1684. Figure (b) shows the sizes N_ϕ (dashed), N_u (light-gray) and $|Y_M|$ of the basis sets. And Figure (c) depicts for basis set 49 the decay of the \log_{10} of the eigenvalues of the correlation operator of the underlying snapshots for the phase-field (dashed) and for the chemical potential (light-gray) and furthermore the decay of the error of the Empirical Interpolation Method for the increasing number of magic nodes.

center of the microscopic domain for basis sets related to small volumes to outer regions for larger volumes. This is due to the fact that, disregarding one point in $(0, 0)$, the magic points are always located in the phase transition zones of the microstructures. The inner-to-outer-movement holds also for the characteristic shapes of the principal modes of the POD-bases.

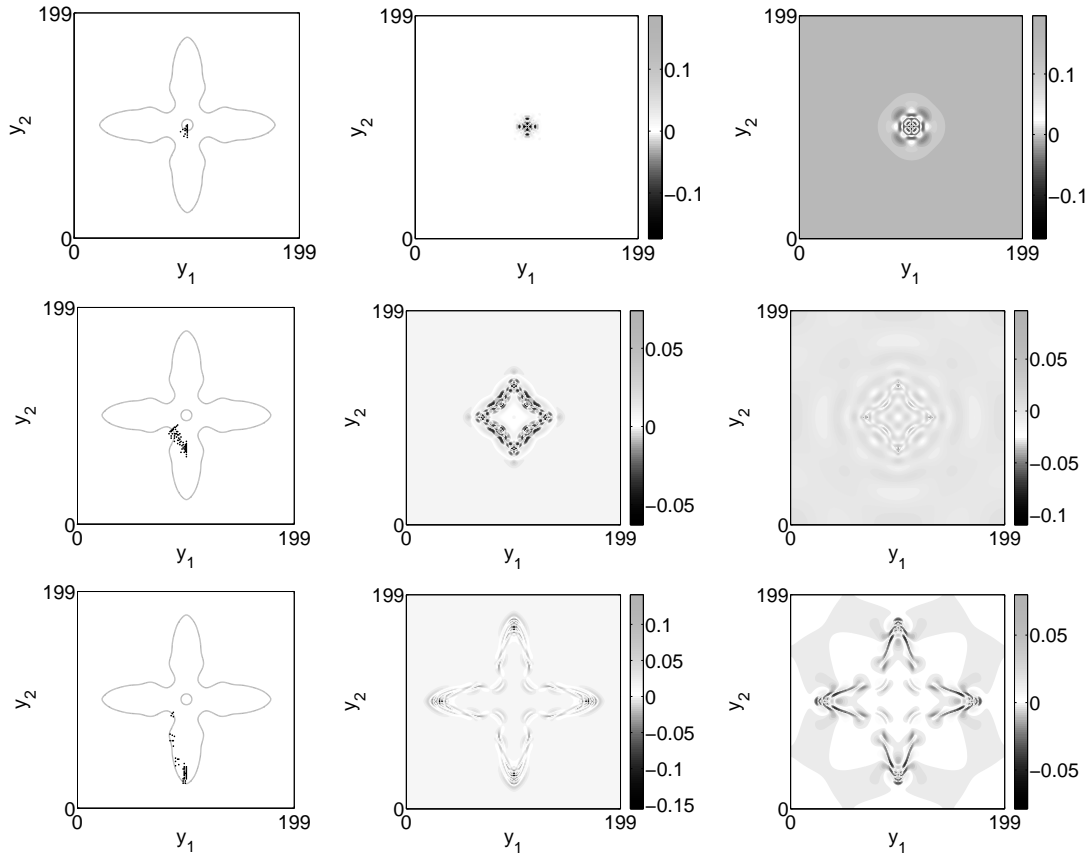
The different sizes of the basis sets explain for example why it takes nearly twice as long to solve the reduced model in $(0, 0)$ as in $(19, 9)$: in course of the simulation all the basis sets are used to construct the solution in $(0, 0)$, but for $(19, 9)$ only the smaller basis sets.

In this subsection a reduced model with parameters $N_B = 100$, $\epsilon_{POD} = 1e-13$, $\epsilon_{EI} = 1e-5$, $\epsilon_B = 0.1$ was constructed that is very efficient: alongside accurate results, the model is solved in much less time than the detailed model. The next subsection is devoted to the macroscopic conditions that must be fulfilled such that the reduced model still delivers accurate results.

4.4.3 Generalization ability: variation of the macroscopic problem

The reduced model is constructed from microscopic solutions whose developments are manipulated by certain temperature evolutions. Hence, it can be expected that if a setting S produces temperature evolutions that are similar to the reduced model's training data evolutions, then the reduced solution is expected to be accurate for the setting S .

Table 4.6 specifies the parameters of three settings and the setting S_0 of the previous subsection used to construct the reduced model with parameters $N_B = 100$, $\epsilon_{POD} = 1e-13$, $\epsilon_{EI} = 1e-5$ and $\epsilon_B = 0.1$. In order to clarify the situation: the settings and the detailed but also the reduced solutions change, although the reduced model remains the same. Figure 4.9 illustrates the detailed macroscopic temperature solutions for the settings S_1 , S_2 and S_3 ; the solution of S_0 is depicted in Figure 4.4. The shape of all solutions is



(a) Magic points of the basis sets 0, 49 and 99 (from top to bottom). (b) Principal phase-field mode of the basis sets 0, 49 and 99 (from top to bottom). (c) Principal chemical potential mode of the basis sets 0, 49 and 99 (from top to bottom).

Figure 4.8: Results on the large time-space cylinder of the reduced model with parameters $N_B = 100$, $\epsilon_{POD} = 1e-13$, $\epsilon_{EI} = 1e-5$ and $\epsilon_B = 0.1$. Figure (a) presents the distribution of the magic points on the microscopic domain for the basis sets 0, 49 and 99: dots mark the magic points, the inner circle represents the initial solid phase and the larger dendrite the largest solid phase of the training data. Figure (b) shows the principal mode of the POD-basis for the phase-field for the same basis sets and Figure (c) depicts the same for the chemical potential.

setting	$H_{g,1}$	$H_{g,2}$	$C_{\text{boundary-flux}}$	K
S_0	20	10	$5e-6$	200
S_1	20	10	$6e-6$	200
S_2	20	10	$4e-6$	200
S_3	50	20	$7e-6$	500

Table 4.6: Generalization ability: variation of the macroscopic problem. Tabulated are the varying parameters of the macroscopic settings S_0 , S_1 , S_2 and S_3 . Common to all of them are $H_\ell = 200$ and $K_t = 50000$.

similar, but the minimal temperature of S_1 is significantly smaller than of S_0 whose itself is significantly smaller than of S_2 . This can also be deduced from the results presented in Table 4.7 comparing not only the detailed macroscopic temperature solutions of the

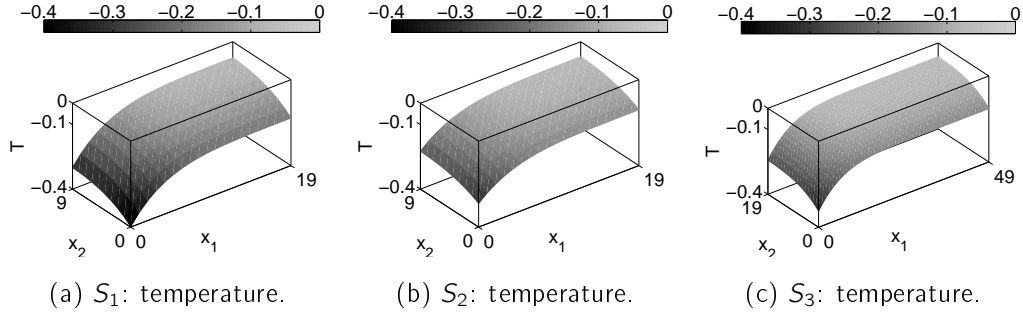


Figure 4.9: Generalization ability: variation of the macroscopic problem. The figures depict the final macroscopic temperature fields for the setting S_1 , S_2 and S_3 . The solution for S_0 is illustrated in Figure 4.4.

difference	$\ \Delta T\ _{Q_1, \infty}$	$\ \Delta T\ _{Q_2}$	$\ \Delta \phi\ _{Q_1^*, \infty}$	$\ \Delta \phi\ _{Q_2^*, \infty}$	$\ \Delta \phi\ _{Q_3^*, \infty}$	$\ \Delta \phi\ _{Q_4^*, \infty}$
$r(S_0) - d(S_0)$	$6.08e-5$	$2.15e-6$	$7.13e-4$	$1.21e-4$	$1.40e-4$	$8.40e-5$
$d(S_1) - d(S_0)$	$5.39e-2$	$1.21e-2$	$1.89e+0$	$1.04e+0$	$1.71e+0$	$6.09e-2$
$r(S_1) - d(S_1)$	$1.53e-1$	$2.12e-3$	$2.22e+0$	$1.25e-3$	$6.30e-2$	$8.40e-5$
$d(S_2) - d(S_0)$	$5.38e-2$	$1.23e-2$	$1.91e+0$	$1.05e+0$	$1.69e+0$	$6.16e-2$
$r(S_2) - d(S_2)$	$1.78e-3$	$3.27e-5$	$1.11e-1$	$7.56e-4$	$6.56e-3$	$8.40e-5$
$r(S_3) - d(S_3)$	$5.60e-3$	$4.68e-5$	$5.50e-1$	$5.79e-4$	$4.38e-3$	$4.90e-4$

Table 4.7: Generalization ability: variation of the macroscopic problem. Tabulated are the differences of the solutions of the macroscopic temperature and the microscopic phase-fields in the corner nodes of the macroscopic domain. For the macroscopic setting S_i the term $r(S_i)$ indicates the reduced and $d(S_i)$ the detailed solution. Q_i^* denotes for $i = 1, \dots, 4$ the time-space cylinder $I_{t_{end}, kt} \times \{x_i\} \times Y_{h_\ell}$ with $x_1 = (0, 0)$, $x_2 = (H_{g,1}, 0)$, $x_3 = (0, H_{g,2})$ and $x_4 = (H_{g,1}, H_{g,2})$.

settings S_0 , S_1 and S_2 but also their microscopic phase-field solutions. Furthermore, for all settings the respective reduced is compared to the respective detailed solution.

Because the minimal temperature decreases faster over time for setting S_1 than for S_0 the largest dendrite of S_1 grows faster than of S_0 resulting in volumes of 0.2029 and 0.1684 in the end. Consequently, as the training data does not contain the largest dendrites of S_1 , they differ significantly: the most appropriate phase-field POD-basis is not appropriate enough to produce an accurate reduced approximation. For smaller dendrites the approximations are noteworthy better. The reduced solution for setting S_2 is much more accurate because the largest dendrite is only of volume 0.1344. Still, the error is not immaterial. The same holds for the setting S_3 with a larger macroscopic domain and a larger diffusivity K . At least the dendrites related to smaller volumes are approximated quite accurately.

Finally, Figure 4.10 presents results for the setting S_4 , which is equal to S_3 , only the heat fluxes on the boundary of the macroscopic domain are different: it is $\frac{k_t K}{2h_g^2} \nabla T \cdot n = -1.4e-5$ for both vertical and $-7e-6$ for both horizontal boundaries in (4.24). In the end, the largest dendrite's volume is 0.1587 which is smaller than of the largest dendrite of setting S_1 . Again, the reduced approximation of the smaller dendrites is accurate, but for the largest it is weak: the fingers of the dendrite are a little longer in the reduced but the body

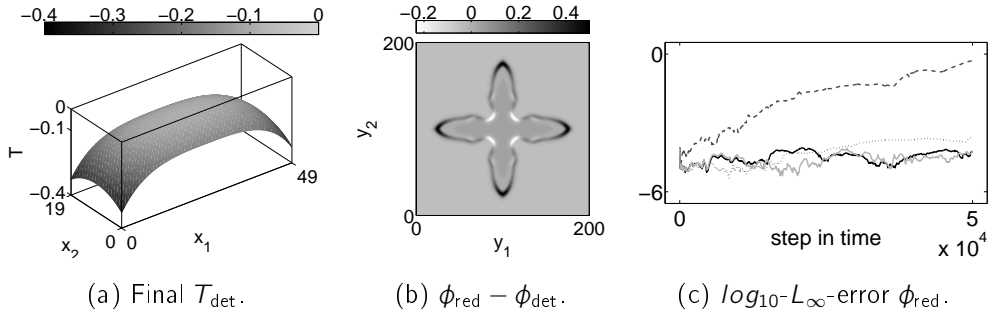


Figure 4.10: Generalization ability: variation of the macroscopic problem. The error of the reduced compared to the detailed temperature solution is $\|\Delta T\|_{Q,\infty} = 5.67e-3$ or rather $\|\Delta T\|_{Q,2} = 8.41e-5$. Figure (a) depicts the detailed temperature solution in the end, (b) the difference of the reduced and the detailed phase-field solution in the end in the macroscopic node $(0,0)$, and Figure (c) the \log_{10} - L_∞ -errors of the microscopic phase-fields in the macroscopic nodes $(0,0)$ (dashed), $(8,3)$ (dotted), $(16,6)$ (dark-gray) and $(24,9)$.

is a little smaller than in the detailed solution.

The numerical results presented in this subsection indicate that the correctness of the reduced model does, as expected, neither depend on the size of the macroscopic domain nor on the shape of the macroscopic temperature field. It is only the temperature evolutions influencing the microscopic problems in the online phase that are fundamental to precision. The closer they are to the offline evolutions influencing the training data, the more accurate is the reduced solution.

4.5 Conclusion and outlook

The combination of several modern procedures for treating time and parameter dependency as well as non-linearity induced a successful model reduction scheme for a nontrivial two-scale model. The complex reduced model comprises a full offline-online decomposition, hence its computational complexity is completely independent of the detailed discretization complexity. Minor new methodological contributions presented in this section are the solution of reduced systems via Least-Squares instead of Galerkin, and the partitioning approach adapted from problem specific feature extraction with projection-based basis change.

A possibility for extension would be an improved basis generation. As described, the number of snapshots for various trajectories is a problem in case of many time-steps and many nodes. Presumably, the POD-Greedy procedure developed in [29, 31] could be applied for the construction of provably quasi-optimal approximation spaces. Also the derivation of error estimators could be a possible future direction for the considered two-scale model.

Acknowledgment

The results presented in this section result from joint work with Bernard Haasdonk. They are published as preprint [50], and since 4 June 2014 they are accepted for publication by

5 Upscaling of a tri-phase phase-field model for precipitation in porous media

Abstract

By combination of several modern modeling techniques, a numerically efficiently solvable two-scale phase-field model is developed. It models a precipitation process in a porous medium whose pore-space is occupied by three phases. A solid P_3 is attached to the grain, and two fluids P_1 and P_2 occupy the non-solid pore-space. Only the fluid P_1 can contain dissolved particles that can precipitate on the solid P_3 . The reverse reaction is also possible, that is solid particles of P_3 can dissolve in P_1 . The concentration of particles in P_1 is variable, due to precipitation and diffusion, whereas it is zero in P_2 and one in P_3 .

A pore-scale phase-field model is established that approximates in the limit, for the width of the phase-transition regions tending to zero, a suitable sharp-interface model. Well-posedness is shown for the phase-field equations with given sufficiently regular concentration. The analysis of the coupled problem is part of future research. By homogenization a two-scale model is derived. It is suitable for settings where the dissolved particles in P_1 diffuse on the Darcy-scale.

Numerical solutions of the upscaled problem demonstrate the interdependence of the evolution of the three phases and the evolution of the concentration of the dissolved particles in P_1 .

5.1 Introduction

This section introduces a model that describes a precipitation or rather dissolution process in a porous medium. The medium's pore-space is occupied by three substances: two immiscible, incompressible fluids and a solid. Let P_1 denote water, P_2 oil and P_3 solid. The motivating background is the observation that the pore-space of a porous medium is usually occupied by many different substances like water, oil, air, Some substances can contain dissolved particles, others not. For example salt can dissolve in water but not in air or oil. Therefore, if a crystalline solid of salt is surrounded by water on the one side and oil on the other, then the salt can only dissolve in the water. Thus, in contact with water the solid can recede, but nothing happens when it is in contact with oil. The reverse reaction is also possible: dissolved particles in the water can precipitate on the solid or on the grain – the boundary of the pore-space. The concentration of particles is constantly equal to zero in the oil and to one in the solid. On contrary, due to precipitation, dissolution and transport, it is variable in the water.

The combination of several modern modeling techniques results in an upscaled model that allows for an efficient numerical solution. Firstly, a pore-scale phase-field model is developed. The model describes the evolution of three phase-fields and the evolution of the concentration of the dissolved particles in the water. Besides by precipitation and dissolution, the evolution of the concentration is also influenced by diffusion. Motivated by the Diffuse Domain Approximation (DDA) method introduced in [44], each phase-field is treated as a smooth approximation to the characteristic function – in the sharp-interface sense – of one of the three substances involved: water, oil and solid. Within a small phase-transition region a phase-field varies smoothly from 1 inside a region occupied by one of the substances to 0 inside the regions occupied by the two other substances. A

formal asymptotic analysis shows that the solution of the phase-field model approximates in the limit, that is for the width $\xi > 0$ of the phase-transition regions tending to zero, the solution of a suitable sharp-interface model. Secondly, considering a situation with periodically distributed grains and solids with a period of scale $\epsilon > 0$, the application of a formal periodic homogenization technique to the pore-scale model yields in the limit for $\epsilon \rightarrow 0$ a two-scale model. It is suitable for settings where the dissolved particles in the water diffuse on the Darcy-scale. It consists of a macroscopic homogenized diffusion equation for the concentration of particles in the water, and, for each point of the macroscopic domain, of local cell problems for the evolution of the three phases. The variables on the different scales depend continuously on each other: the growth of the microscopic solid is influenced by the macroscopic concentration of the dissolved particles in the water, and vice versa the change of the pore structure influences the evolution of the concentration. Thirdly, based on the adaptive strategy of Section 3, exploiting these continuous inter-scale dependencies, an adaptive discrete solution scheme is developed that allows for an efficient numerical solution.

The reason behind the preference of a phase-field model to e.g. a sharp-interface model, is its simpler manageability in terms of mathematical analysis, upscaling and numerical discretization. The developed pore-scale phase-field model bears a slight resemblance to a model introduced in [54]: both models utilize a pore-scale phase-field formulation describing a precipitation process in a porous medium. However, there are considerable differences. Firstly, the [54]-model considers only two substances, one solid and one liquid containing dissolved particles. Secondly, due to the complicated structure of the evolution equation for the concentration of the particles in [54], homogenization seems to be at least very challenging if not impossible, whereas it is quite straightforward for this article's model. Thirdly, the same holds for the generalizability to more than three substances. Whereas it is questionable whether it is at all possible to generalize the [54]-model to three substances, a generalization to more than three substances is straightforward for this article's model. Section 5.5 hints at how to generalize.

This section is organized as follows. Section 5.2 introduces the pore-scale phase-field model and shows that its solution approximates in the limit the solution of a suitable sharp-interface model. Well-posedness is shown for the phase-field equations for a given sufficiently regular concentration. Section 5.3 develops the upscaled model as well as the proposed discrete efficient adaptive solution scheme. Finally, Section 5.4 presents numerical results of the upscaled model in two spatial dimensions that document the interdependence of the concentration of the dissolved particles on the Darcy-scale and the change of the pore structure.

5.2 The pore-scale model

This section briefly discusses the sharp-interface model that is approximated by the proposed pore-scale phase-field model. Next, it develops the pore-scale phase-field model and shows that the model describes a perfect mixture almost everywhere in the time-space cylinder – a perfect mixture in the sense that the sum of the three phase-fields equals one and that each phase-field is greater or equal to zero. Finally, this section shows that the solution of the phase-field model approximates in the limit for the width of the phase transition regions tending to zero the solution of the sharp-interface model.

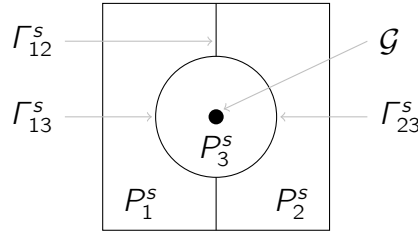


Figure 5.1: The considered pore-scale situation. The domain Ω consists of the pore-space \mathcal{P} , the grain \mathcal{G} , which is located in the center of Ω , and the grain-boundary $\Gamma_{\mathcal{G}} = \partial\mathcal{G}$. The boundary $\Gamma_{\mathcal{P}}$ of the pore-space \mathcal{P} satisfies $\Gamma_{\mathcal{P}} = \Gamma_{\Omega} \cup \Gamma_{\mathcal{G}}$, where $\Gamma_{\Omega} = \partial\Omega$ denotes the outer-boundary of Ω . The pore-space is occupied by the two immiscible and incompressible fluids P_1 in P_1^s and P_2 in P_2^s , the solid P_3 in P_3^s , and their interfaces Γ_{12}^s , Γ_{13}^s and Γ_{23}^s . The solid P_3 is attached to the boundary $\Gamma_{\mathcal{G}}$ of the grain \mathcal{G} . The fluid P_1 occupies the left and the fluid P_2 the right part of the non-solid pore-space.

5.2.1 The sharp-interface model

Consider a time-interval $J(T) := (0, T]$, $T > 0$, with $\overline{J(T)} = [0, T]$, and a spatial domain $\Omega \subset \mathbb{R}^d$, $d \in \{2, 3\}$, with a boundary $\Gamma_{\Omega} = \partial\Omega$. Ω is subdivided into the pore-space \mathcal{P} , a grain \mathcal{G} and the boundary $\Gamma_{\mathcal{G}}$ of the grain, that is $\Omega = \mathcal{P} \cup \mathcal{G} \cup \Gamma_{\mathcal{G}}$. The boundary $\Gamma_{\mathcal{P}}$ of the pore-space \mathcal{P} equals $\Gamma_{\Omega} \cup \Gamma_{\mathcal{G}}$. Let $n_{\mathcal{P}}$ be the outer-normal to $\Gamma_{\mathcal{P}}$. The pore-space \mathcal{P} is occupied by three substances P_i , $i \in I := \{1, 2, 3\}$: two immiscible, incompressible fluids P_1 (e.g. water) and P_2 (e.g. oil) and a solid P_3 . The substances occupy three disjoint time-dependent a priori unknown regions $P_1^s(t)$, $P_2^s(t)$ and $P_3^s(t)$. These regions are separated by the moving interfaces $\Gamma_{ij}^s(t) = \partial P_i^s(t) \cap \partial P_j^s(t)$, $i, j \in I$ and $j > i$, where the normal n_{ij} to $\Gamma_{ij}^s(t)$ points into the domain $P_j^s(t)$. Therefore,

$$\mathcal{P} = P_1^s(t) \cup P_2^s(t) \cup P_3^s(t) \cup \Gamma_{12}^s(t) \cup \Gamma_{13}^s(t) \cup \Gamma_{23}^s(t). \quad (5.1)$$

Throughout this section it is assumed that, as depicted in Figure 5.1, the solid P_3 surrounds the grain which is located in the center of the pore-space \mathcal{P} , and that P_3 is initially fully surrounded by the two fluids P_1 and P_2 , where P_1 occupies the left and P_2 the right part of the non-solid domain $\mathcal{P} \setminus P_3^s(t)$ of the pore-space.

The fluid P_1 in $P_1^s(t)$ contains dissolved particles that can precipitate on the P_1 -part $\partial P_1^s(t) \cap \Gamma_{\mathcal{G}}$ of the grain-boundary $\Gamma_{\mathcal{G}}$ as well as on the boundary $\Gamma_{13}^s(t)$. The domains $P_2^s(t)$ resp. $P_3^s(t)$ are occupied by the fluid P_2 resp. P_3 . The concentration u of particles is fixed in these regions. By assumption, P_2 does not contain particles, hence $u = 0$ in $P_2^s(t)$. Furthermore, let $\rho > 0$ be the fixed concentration of particles in the solid region $P_3^s(t)$. The following sharp-interface model accounts for the diffusion process of the dissolved particles' concentration u in $P_1^s(t)$, for mass conservation at the moving interfaces and for the precipitation process.

Problem 5.1. Given the constant diffusion coefficient $D > 0$, the normal velocity v_{12}^n of the moving interface $\Gamma_{12}^s(t)$ and the normal velocity v_{13}^n of $\Gamma_{13}^s(t)$, the concentration $\rho > 0$ of particles in the solid P_3 , and the initial condition $u_0 : P_1^s(0) \rightarrow \mathbb{R}$, find the concentration

u satisfying

$$\begin{aligned}
\partial_t u - D\Delta u &= 0 && \text{in } J(T) \times P_1^s(t), \\
-D\nabla u \cdot n &= 0 && \text{on } J(T) \times (\partial P_1^s(t) \cap \Gamma_{\mathcal{P}}), \\
-D\nabla u \cdot n_{12} &= v_{12}^n u && \text{on } J(T) \times \Gamma_{12}^s(t), \\
-D\nabla u \cdot n_{13} &= v_{13}^n (u - \rho) && \text{on } J(T) \times \Gamma_{13}^s(t), \\
u(0, x) &= u_0(x) && \text{in } P_1^s(0).
\end{aligned} \tag{5.2}$$

The Rankine-Hugoniot conditions in (5.2), that is the third and the fourth equation, ensure the conservation of mass at the moving interfaces of $P_1^s(t)$, due to $u = 0$ in $P_2^s(t)$ and $u = \rho$ in $P_3^s(t)$.

The a-priori unknown normal velocities are prescribed by the following kinetic conditions

$$\begin{aligned}
v_{12}^n &= -\sigma \kappa_{12} \text{ on } J(T) \times \Gamma_{12}^s(t), \\
v_{13}^n &= -\sigma \kappa_{13} - f(u) \text{ on } J(T) \times \Gamma_{13}^s(t), \\
v_{23}^n &= -\sigma \kappa_{23} \text{ on } J(T) \times \Gamma_{23}^s(t),
\end{aligned} \tag{5.3}$$

with the constant surface tension $\sigma > 0$ and the mean curvatures κ_{ij} of the interfaces $\Gamma_{ij}^s(t)$, $i, j \in I$, $j > i$. In order to ensure that the interfaces do not leave the pore-space, the following conditions are imposed

$$\begin{aligned}
v_{12}^n &= \min(0, -\sigma \kappa_{12}) \text{ on } J(T) \times (\Gamma_{12}^s(t) \cap \Gamma_{\mathcal{P}}), \\
v_{13}^n &= \min(0, -\sigma \kappa_{13} - f(u)) \text{ on } J(T) \times (\Gamma_{13}^s(t) \cap \Gamma_{\mathcal{P}}), \\
v_{23}^n &= \min(0, -\sigma \kappa_{23}) \text{ on } J(T) \times (\Gamma_{23}^s(t) \cap \Gamma_{\mathcal{P}}),
\end{aligned} \tag{5.4}$$

where v_{ij}^n denotes in this case the velocity of the moving interface $\Gamma_{ij}^s(t)$ into the outer-normal direction $n_{\mathcal{P}}$. It is assumed that an initial configuration $P_1^s(0)$, $P_2^s(0)$ and $P_3^s(0)$ is given.

The rate function $f(u)$ drives the precipitation process. Many examples of rate functions for precipitation can be found in the literature, as for example in [55, 39]. The function used here is a simple linear function

$$f(u) = c_{u,0}(u - c_{u,1}), \tag{5.5}$$

with a constant slope $0 < c_{u,0} < \infty$ and a constant threshold $0 < c_{u,1} < \rho$ separating precipitation and dissolution. If the concentration is larger than the threshold, then dissolved particles precipitate and the solid increases. Vice versa it recedes in case that the concentration is below the threshold.

Remark 5.2. *In general, the surface tension of a solid is anisotropic because of the crystalline structure. For simplicity only constant isotropic tensions are considered. Hence, the numerical results do not show dendritic growth. In two spatial dimensions, since the surface tensions σ are assumed to be equal, Young's law*

$$\frac{\sin(\Theta_1)}{\sigma} = \frac{\sin(\Theta_2)}{\sigma} = \frac{\sin(\Theta_3)}{\sigma}, \tag{5.6}$$

where Θ_1 , Θ_2 and Θ_3 denote the angles between the interfaces as depicted in Figure 5.3 on page 89, yields that if the three interfaces $\Gamma_{12}^s(t)$, $\Gamma_{13}^s(t)$ and $\Gamma_{23}^s(t)$ meet, then they meet at an angle of 120° .

Remark 5.3. From the physical point of view, the boundary $\Gamma_{23}^s(t)$ separating oil and solid should be immobile, and the boundary $\Gamma_{13}^s(t)$ separating water and solid should only be affected by precipitation. However, this sharp-interface model is modeled so that its solution is approximated by the solution of the phase-field model developed below. Since the evolution of a phase-field model type diffuse interface is always affected by the interface's curvature, the mean curvatures of the sharp-interfaces $\Gamma_{13}^s(t)$ and $\Gamma_{23}^s(t)$ affect their evolution. Further details are presented in Section 5.2.3.

5.2.2 The phase-field model

The aim is to develop an upscaled model that allows for an efficient numerical solution. Because it is usually much easier to deal with phase-field instead of sharp-interface models when it comes to numerical simulations as well as upscaling, the sharp interface model of the previous subsection is approximated by a phase-field model. According to the three considered pure states P_1 , P_2 and P_3 , three phase-fields are invented. For $i \in I$, the phase-field $\phi_i(t, x)$ is treated as a smooth approximation to the characteristic function $\chi_i(t, x)$ of the sharp-interface domain $P_i^s(t)$.

At first, this subsection develops a system of three evolution equations for the three phase-fields. Thereafter, motivated by the Diffuse Domain Approximation (DDA) method in [44], the sharp-interface model's evolution equation in (5.2), which models the diffusion process for the concentration u of particles in the fluid region $P_1^s(t)$, is transformed into an equation that is valid in the whole pore-space \mathcal{P} . Additional source terms approximate the Rankine-Hugoniot condition at the interfaces $\Gamma_{12}^s(t)$ and $\Gamma_{13}^s(t)$. Without going into details here, the phase-field ϕ_1 plays a crucial role in the transformed equation due to the fact that it approximates the characteristic function of the fluid region $P_1^s(t)$.

For ease of the presentation the development of the phase-field model is subdivided into two parts. Firstly, the evolution equations for the phase-fields are developed for a given concentration. Secondly, for a given phase-field, the equation for the concentration is developed. Clearly, the two parts are coupled in the end.

5.2.2.1 The evolution equations for the phase-fields $\Phi = (\phi_1, \phi_2, \phi_3)$

For $i \in I$, the phase-field $\phi_i(t, x)$ is treated as a smooth approximation to the characteristic function $\chi_i(t, x)$ of the sharp-interface domain $P_i^s(t)$. Therefore, it must satisfy $0 \leq \phi_i \leq 1$, and the sum of the phase-fields has to equal one. Consequently, the admissible states of $\Phi = (\phi_1, \phi_2, \phi_3)$ belong to

$$\mathcal{S} := \{V = (v_1, v_2, v_3) \in [0, 1]^3 \mid \sum_{i \in I} v_i = 1\}. \quad (5.7)$$

The Allen-Cahn type equations developed in the following guarantee that if the initial state $\Phi(0, x) \in \mathcal{S}$ for a.e. $x \in \mathcal{P}$ then the solution $\Phi(t, x) \in \mathcal{S}$ for a.e. $(t, x) \in J(T) \times \mathcal{P}$. The evolution of the system is driven by the gradient of a free energy $U(\Phi)$ and, additionally, the diffuse interface region $\Gamma_{13}^d(t)$ separating the liquid domain $P_1^d(t)$ and the solid $P_3^d(t)$ is driven by the precipitation process.

The free energy $U(\Phi)$ is given by

$$U(\Phi) = \int_{\mathcal{P}} 3W(\Phi(t, x)) + \frac{3}{8}\xi^2 \sum_{i \in I} |\nabla \phi_i(t, x)|^2 dx. \quad (5.8)$$

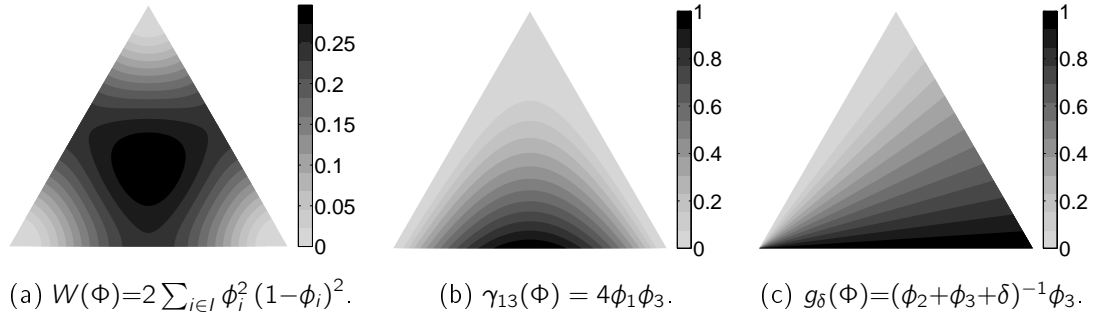


Figure 5.2: Contour plots in barycentric coordinates for $\Phi = (\phi_1, \phi_2, \phi_3) \in \mathcal{S}$. The bottom left corner represents the pure fluid \bar{P}_1^d , that is $\Phi = (1, 0, 0)$, the top corner the fluid \bar{P}_2^d and the bottom right corner the solid \bar{P}_3^d . The Figure (a) depicts the contour plot of the potential W , (b) of the indicator γ_{13} of the diffuse interface $\bar{\Gamma}_{13}^d$ separating the fluid \bar{P}_1^d and the solid \bar{P}_3^d , and (c) of the interpolation function g_δ with $\delta = 1e-6$.

The potential $W = W(\Phi)$,

$$W(\Phi) = 2 \sum_{i \in I} \phi_i^2 (1 - \phi_i)^2, \quad (5.9)$$

with the partial derivatives

$$\partial_{\phi_i} W(\Phi) = 4(\phi_i - 3\phi_i^2 + 2\phi_i^3) \text{ for } i \in I, \quad (5.10)$$

is non-convex in \mathcal{S} and minimal for the pure states \bar{P}_i^d ,

$$\bar{P}_i^d := \{\Phi \in \mathcal{S} \mid \phi_i = 1\}. \quad (5.11)$$

It is maximal for $\Phi = (\frac{1}{3}, \frac{1}{3}, \frac{1}{3})$. In sub-domains where only two phases are present it coincides with a potential that is suitable for a setting with only two phases. Both W and $\partial_{\phi_i} W$ are Lipschitz in \mathcal{S} , since for $\Phi_1, \Phi_2 \in \mathcal{S}$ it follows

$$\begin{aligned} |W(\Phi_1) - W(\Phi_2)| &\leq 18 \sum_{i \in I} |\phi_{1,i} - \phi_{2,i}|, \\ |\partial_{\phi_i}(W(\Phi_1) - W(\Phi_2))| &\leq 42 |\phi_{1,i} - \phi_{2,i}|. \end{aligned} \quad (5.12)$$

Figure 5.2a depicts a contour plot of W in \mathcal{S} . Both, U resp. W are special cases of a free energy resp. a potential developed in [6, 7]. The authors also propose the handling of W utilized in the following: besides the derivative $\partial_{\phi_i} W$ also the derivatives $\partial_{\phi_j} W$ for $j \in I \setminus \{i\}$ appear in the evolution equation for the phase-field ϕ_i . This yields $\phi_1 + \phi_2 + \phi_3 = 1$ almost everywhere. In [6, 7] a Cahn-Hilliard flow model is developed. Unlike Cahn-Hilliard equations, Allen-Cahn type equations guarantee the property $\phi_i \in [0, 1]$ for $i \in I$. As it is shown below, it is fundamental to the well-posedness of the evolution equation for the concentration that $\phi_1 \in [0, 1]$. Therefore, Allen-Cahn type equations are preferred.

The idea of phase-field modeling is to replace sharp interfaces by diffuse ones. The diffuse interface regions $\Gamma_{ij}^d(t)$ approximating the sharp-interfaces $\Gamma_{ij}^s(t)$, for $i, j \in I$ with $i < j$, are characterized by

$$\Gamma_{ij}^d(t) := \{x \in \mathcal{P} \mid \Phi(t, x) \in \bar{\Gamma}_{ij}^d\}, \text{ for } t \in \overline{J(T)}, \quad (5.13)$$

with the diffuse interface states

$$\overline{\Gamma}_{ij}^d := \{\Phi \in \mathcal{S} \mid \phi_i + \phi_j = 1, \phi_i, \phi_j \in (0, 1)\}. \quad (5.14)$$

For example within the diffuse interface $\Gamma_{12}^d(t)$ separating the pure sub-domains $P_1^d(t)$ and $P_2^d(t)$, where for $i \in I$

$$P_i^d(t) := \{x \in \mathcal{P} \mid \Phi(t, x) \in \overline{P}_i^d\}, \text{ for } t \in \overline{J(\overline{T})}, \quad (5.15)$$

the phase-field ϕ_1 varies smoothly from 1 in $P_1^d(t)$ to 0 in $P_2^d(t)$. Vice versa, since ϕ_2 approximates the characteristic function of $P_2^d(t)$, ϕ_2 varies smoothly from 0 in $P_1^d(t)$ to 1 in $P_2^d(t)$.

The force f_1 , that models the precipitation process of the dissolved particles in $P_1^d(t)$ on the boundary of $P_3^d(t)$, must vanish in the sub-domains where ϕ_1 or ϕ_3 vanish. This is in the diffuse interfaces $\Gamma_{12}^d(t)$ and $\Gamma_{23}^d(t)$ and in the pure regions $P_1^d(t)$, $P_2^d(t)$ and $P_3^d(t)$. A suitable choice is

$$f_1 : \mathcal{S} \times \mathbb{R} \rightarrow \mathbb{R}, \quad f_1(\Phi, u) = \alpha \xi \gamma_{13}(\Phi) f(u), \quad (5.16)$$

where $f(u)$ is the rate-function defined in (5.5) of the precipitation process and the function γ_{13} ,

$$\gamma_{13} : \mathcal{S} \rightarrow [0, 1], \quad \gamma_{13}(\Phi) = 4 \phi_1 \phi_3, \quad (5.17)$$

vanishes in

$$\overline{\Gamma}_{12} \cup \overline{\Gamma}_{23} \cup \overline{P}_1 \cup \overline{P}_2 \cup \overline{P}_3. \quad (5.18)$$

Therefore, the indicator $\gamma_{13} \geq 0$ vanishes everywhere in the pore-space except for the regions where both ϕ_1 and ϕ_3 do not vanish. It is maximal for $\Phi = (\frac{1}{2}, 0, \frac{1}{2})$, that is exactly in the middle of $\Gamma_{13}^d(t)$. Figure 5.2b depicts a contour plot of $\gamma_{13}(\Phi)$ in \mathcal{S} . The parameters α and ξ are parameters of the evolution equation to be given in the following.

Since the diffuse interfaces $\Gamma_{12}^d(t)$ and $\Gamma_{23}^d(t)$ are not driven by precipitation, and since the effect of the precipitation in the interface region $\Gamma_{13}^d(t)$ on ϕ_1 must be contrary to the effect on ϕ_3 , the driving forces f_2 and f_3 are defined by

$$\begin{aligned} f_2(\Phi, u) &= 0, \\ f_3(\Phi, u) &= -f_1(\Phi, u) = -\alpha \xi \gamma_{13}(\Phi) f(u). \end{aligned} \quad (5.19)$$

Furthermore, define

$$G_i(\Phi, u) = \left(\sum_{j \in I \setminus \{i\}} (\partial_{\phi_i} - \partial_{\phi_j}) W(\Phi) \right) + f_i(\Phi, u) \text{ for } i \in I. \quad (5.20)$$

The forces f_i are locally Lipschitz. Especially, if $\Phi_1, \Phi_2 \in \mathcal{S}$ and $|u_1|, |u_2| \leq d < \infty$ then

$$\begin{aligned} &|f_1(\Phi_1, u_1) - f_1(\Phi_2, u_2)| \\ &\leq 4\alpha\xi (|u_1 - u_2| + c_{u,0}(d + c_{u,1}) \sum_{j=1,3} |\phi_{1j} - \phi_{2j}|). \end{aligned} \quad (5.21)$$

Hence, the equations (5.12) and (5.21) yield Lipschitz estimates for the functions G_i , $i \in I$, in $\mathcal{S} \times [-d, d]$.

The considerations from above result in the following problem for the unknown phase-fields in dependence on a given sufficiently regular concentration u .

Problem 5.4. Given the parameters $\alpha, \xi > 0$, the concentration $u : \overline{J(T)} \times \mathcal{P} \rightarrow \mathbb{R}$, the functions $G_i(\Phi, u)$ defined by (5.20), the potential $W(\Phi)$ defined by (5.9), the driving forces $f_i(\Phi, u)$ defined by (5.16) and (5.19), and the initial condition $\Phi_0 = (\phi_{1,0}, \phi_{2,0}, \phi_{3,0}) : \mathcal{P} \rightarrow \mathcal{S}$, find the phase-fields $\Phi = (\phi_1, \phi_2, \phi_3)$ satisfying

$$\begin{aligned} \alpha \xi^2 \partial_t \phi_i - \frac{3}{4} \xi^2 \Delta \phi_i + G_i(\Phi, u) &= 0 \text{ in } J(T) \times \mathcal{P}, \\ - \frac{3}{4} \xi^2 \nabla \phi_i \cdot n_{\mathcal{P}} &= 0 \quad \text{on } J(T) \times \Gamma_{\mathcal{P}}, \\ \Phi(0, x) &= \Phi_0(x) \quad \text{in } \mathcal{P}. \end{aligned} \tag{5.22}$$

The parameter $\alpha > 0$ defines a time relaxation parameter that equals $\frac{3}{4\sigma}$ with the constant surface tension $\sigma > 0$ (see Section 5.2.3). Since the width of the diffuse interface regions is determined by a competition between the Laplacian term in (5.22) and the sum of the derivatives of the potential (see (5.20)), it is proportional to the parameter $\xi > 0$.

Section 5.2.2.4 proves that a weak solution Φ to the Problem 5.4 indeed satisfies $\Phi \in \mathcal{S}$ almost everywhere in $J(T) \times \mathcal{P}$ if $\Phi_0(x) \in \mathcal{S}$ almost everywhere in the pore-space. Furthermore, Section 5.2.3 shows that the limit-interfaces $\Gamma_{ij}^\ell(t)$ of $\Gamma_{ij}^d(t)$ for $\xi \rightarrow 0$ evolve with normal velocities that satisfy the kinetic conditions (5.3) of the sharp-interface model.

5.2.2.2 The evolution equation for the concentration u

In the following, the sharp-interface model's evolution equation in (5.2) in $J(T) \times P_1(t)$, which models the diffusion process for the concentration u of particles in the fluid P_1 , is transformed into an equation that is valid in the whole pore-space $J(T) \times \mathcal{P}$. The transformation is motivated by the Diffuse Domain Approximation (DDA) method introduced in [42, 44]. Additional source terms approximate the Rankine-Hugoniot conditions on the sharp interfaces $\Gamma_{12}^s(t)$ and $\Gamma_{13}^s(t)$, that is on the interfaces separating the regions occupied by $P_1^s(t)$ and $P_2^s(t)$ as well as by $P_1^s(t)$ and $P_3^s(t)$. It is assumed that the phase-fields are given and that they are always in an admissible state, that is $\Phi \in \mathcal{S}$ in $\overline{J(T)} \times \mathcal{P}$.

Remark 5.5. Let $M_1(t) \subset M \subset \mathbb{R}^d$, $t \in [0, T]$, let $\phi : [0, T] \times M \rightarrow [0, 1]$ be a smooth approximation to the characteristic function $\chi(t)$ of $M_1(t)$, and let n_M resp. n_{M_1} be the outward-normal to ∂M resp. ∂M_1 . In [44] a matched asymptotic expansion shows that the solution u_d of the DDA model

$$\begin{aligned} \partial_t((\phi + \delta)u_d) - \nabla \cdot ((\phi + \delta)\nabla u_d) - g_d |\nabla \phi| &= 0 \text{ in } (0, T] \times M, \\ - (\phi + \delta)\nabla u_d \cdot n_M &= 0 \quad \text{on } (0, T] \times \partial M, \end{aligned} \tag{5.23}$$

converges to the solution u_s of the sharp-interface model

$$\begin{aligned} \partial_t u_s - \Delta u_s &= 0 \quad \text{in } (0, T] \times M_1(t), \\ - \nabla u_s \cdot n_{M_1} &= v^n u_s - g_s \text{ on } (0, T] \times \partial M_1(t), \end{aligned} \tag{5.24}$$

for the width $\xi > 0$ of the interface region in the the DDA model tending to zero. In the sharp-interface setting, v^n denotes the outward normal velocity of the evolving boundary $\partial M_1(t)$, and the function $g_s : (0, T] \times \partial M_1(t) \rightarrow \mathbb{R}$ is defined only on $\partial M_1(t)$. In the DDA model, the function $g_d : (0, T] \times M \rightarrow \mathbb{R}$ is an extension of g_s to the whole space. The parameter $\delta > 0$ appears in the DDA-model in order to ensure well-posedness. This regularization is necessary since ϕ might vanish somewhere in M . For the matched asymptotic expansions in [44] it is $\delta = \xi$.

Let $\Phi : \overline{J(\mathcal{T})} \times \mathcal{P} \rightarrow \mathcal{S}$ be given and sufficiently regular. Motivated by the DDA method, the phase-field $\phi_1 : J(\mathcal{T}) \times \mathcal{P} \rightarrow [0, 1]$ is treated as a smooth approximation to the characteristic function $\chi_1(t)$ of the region $P_1^s(t)$ occupied by the fluid P_1 in the sharp-interface setting (5.2). In order to approximate the two Rankine-Hugoniot conditions in (5.2) on the sharp-interface $\Gamma_{12}^s(t)$ and $\Gamma_{13}^s(t)$, a function $\bar{g} : J(\mathcal{T}) \times \mathcal{P} \rightarrow \mathbb{R}$ is defined that interpolates between them. This interpolation procedure is necessary because, as depicted in the Figures 5.1 on page 77 and 5.3 on page 89, the considered sharp-interface setting allows for the existence of triple junctions $\Gamma_{123}^s(t)$ in which the three sharp-interfaces $\Gamma_{12}^s(t)$, $\Gamma_{13}^s(t)$ and $\Gamma_{23}^s(t)$ meet. In the diffuse setting, the sharp interfaces $\Gamma_{ij}^s(t)$ are approximated by the diffuse interfaces $\Gamma_{ij}^d(t)$ characterized in (5.13). In the diffuse triple junctions $\Gamma_{123}^d(t)$, approximating $\Gamma_{123}^s(t)$, all three phase-fields ϕ_1 , ϕ_2 and ϕ_3 exist. Hence,

$$\Gamma_{123}^d(t) = \{x \in \mathcal{P} \mid \Phi(t, x) \in \overline{\Gamma}_{123}^d\}, \text{ for } t \in \overline{J(\mathcal{T})}, \quad (5.25)$$

where

$$\overline{\Gamma}_{123}^d = \{\Phi \in \mathcal{S} \mid \phi_1, \phi_2, \phi_3 \in (0, 1)\}. \quad (5.26)$$

An interpolation is required only in these diffuse triple junctions.

For $\delta \geq 0$ define

$$g_\delta : \mathcal{S} \rightarrow [0, 1], \quad g_\delta(\Phi) = \begin{cases} 1 & \text{if } \delta = 0 \text{ and } \Phi = (1, 0, 0), \\ \frac{\phi_3}{\phi_2 + \phi_3 + \delta} = \frac{\phi_3}{1 - \phi_1 + \delta} & \text{else.} \end{cases} \quad (5.27)$$

Recall that $\Phi \in \mathcal{S}$ yields $\phi_1 + \phi_2 + \phi_3 = 1$ and $\phi_i \geq 0$ for $i \in I$. Therefore, g_δ is defined everywhere in \mathcal{S} . For a fixed $\phi_1 \in [0, 1)$, the function g_{0, ϕ_1} ,

$$g_{0, \phi_1} : [0, 1 - \phi_1] \rightarrow [0, 1], \quad g_{0, \phi_1}(\phi_3) = g_0(\phi_1, 1 - \phi_1 - \phi_3, \phi_3) \quad (5.28)$$

interpolates linearly between 0 for $\phi_3 = 0$ and 1 for $\phi_3 = 1 - \phi_1$. The closer ϕ_1 gets to 1, the steeper the slope of g_{ϕ_1} . For a fixed $1 \leq p \leq \infty$, the function

$$g_{0, p} : [0, 1) \rightarrow [0, 1], \quad g_{0, p}(\phi_1) = \begin{cases} g_0(\phi_1, \frac{1-\phi_1}{p}, \frac{(p-1)(1-\phi_1)}{p}) = \frac{p-1}{p} & \text{if } p < \infty, \\ g_0(\phi_1, 0, 1 - \phi_1) = 1 & \text{else,} \end{cases} \quad (5.29)$$

is constant.

For $i \in I$, define the diffuse phase boundaries

$$\Gamma_i^d(t) := \{x \in \mathcal{P} \mid \Phi(t, x) \in \overline{\Gamma}_i^d\}, \text{ for } t \in \overline{J(\mathcal{T})}, \quad (5.30)$$

where

$$\overline{\Gamma}_i^d := \{\Phi \in \mathcal{S} \mid \phi_i \in (0, 1)\}. \quad (5.31)$$

Assuming that the phase-fields Φ are smooth and that $\nabla \phi_2 = -\frac{1}{p} \nabla \phi_1$ and $\nabla \phi_3 = -\frac{p-1}{p} \nabla \phi_1$ in the diffuse phase boundary $\Gamma_1^d(t)$, then the interpolation function g_0 is constant on every path through $\Gamma_1^d(t)$ that is orthogonal to the level curves of ϕ_1 . This means, in particular, that the interpolation function g_0 is equivalent to 1 in $\Gamma_{13}^d(t)$ and to 0 in

$\Gamma_{12}^d(t)$. Figure 5.2c on page 80 depicts a contour plot of g_δ on \mathcal{S} , where g_δ is a smooth approximation to g_0 if $\delta > 0$.

The diffuse phase interface $\Gamma_1^d(t)$ of the pure phase $P_1^d(t)$ moves with the normal velocity $v_1^n = \frac{\partial_t \phi_1}{|\nabla \phi_1|}$ into the direction of the outer-normal $n_1 = -\frac{\nabla \phi_1}{|\nabla \phi_1|}$. Therefore, the function \bar{g} , finally defined by

$$\bar{g} : J(T) \times \mathcal{P} \rightarrow \mathbb{R}, \quad \bar{g}(t, x) = \rho v_1^n g_0(\Phi(t, x)), \quad (5.32)$$

interpolates between the two Rankine-Hugoniot interface conditions of the sharp-interface model (5.2). Multiplying \bar{g} and $|\nabla \phi_1|$ results in

$$\bar{g}|\nabla \phi_1| = \rho v_1^n g_0(\Phi)|\nabla \phi_1| = \rho \frac{\partial_t \phi_1}{|\nabla \phi_1|} g_0(\Phi)|\nabla \phi_1| = \rho g_0(\Phi) \partial_t \phi_1. \quad (5.33)$$

In sum, for given phase-fields $\Phi \in \mathcal{S}$, these considerations yield the following DDA model for the concentration u .

Problem 5.6. *Given the constant diffusion coefficient $D > 0$, the smooth phase-fields $\Phi : \overline{J(T)} \times \mathcal{P} \rightarrow \mathcal{S}$, the regularization parameter $\delta > 0$, the concentration $\rho > 0$ of particles in the solid P_3 , the interpolation-function $g_0(\Phi)$ defined by (5.27), and the initial condition $u_0 : \mathcal{P} \rightarrow \mathbb{R}$, find the concentration u satisfying*

$$\begin{aligned} \partial_t((\phi_1 + \delta)u) - D\nabla \cdot ((\phi_1 + \delta)\nabla u) - \rho g_0(\Phi)\partial_t \phi_1 &= 0 \text{ in } J(T) \times \mathcal{P}, \\ -D(\phi_1 + \delta)\nabla u \cdot n_{\mathcal{P}} &= 0 \text{ on } J(T) \times \Gamma_{\mathcal{P}} \\ u(0, x) &= u_0(x) \text{ in } \mathcal{P}. \end{aligned} \quad (5.34)$$

For the upscaling in Section 5.3, the numerical simulations in Section 5.4 and for the analysis of Problem 5.6, the interpolation-function $g_0(\Phi)$ in the evolution equation (5.34) is substituted by the continuous approximation $g_\delta(\Phi)$.

It is important to note that though the unknown concentration u is determined in the whole domain, it describes only the concentration of particles in the region $P_1^d(t)$ occupied by the fluid P_1 . Contrarily, the function $\tilde{u}(\Phi, u, \rho) = \phi_1 u + \phi_3 \rho$ describes the concentration in the whole pore-space, that is $\tilde{u} = u$ in $P_1^d(t)$, $\tilde{u} = 0$ in $P_2^d(t)$ and $\tilde{u} = \rho$ in $P_3^d(t)$.

Remark 5.7. *In case that the fluid P_2 is non-existent, that is if $\phi_2 \equiv 0$ in $\overline{J(T)} \times \mathcal{P}$, then the evolution equation of the Problem 5.6 is equivalent to*

$$\partial_t((\phi_1 + \delta)(u - \rho)) - D\nabla \cdot ((\phi_1 + \delta)\nabla u) = 0, \quad (5.35)$$

since $g_0(\Phi) \equiv 1$ if $\phi_2 \equiv 0$. This equation is of the same structure as a substitute of the diffusion equation for the concentration of particles in a phase-field model introduced in [54] describing a precipitation process as well. The substitute reads

$$0 = \partial_t((k(\phi) + \delta)(u - \rho)) - D\nabla \cdot ((k(\phi) + \delta)\nabla u). \quad (5.36)$$

The unknown $u = \frac{c-\rho}{k(\phi)+\delta} + \rho$ substituted the original unknown concentration c , the phase-field ϕ varies smoothly from -1 for liquid to 1 for solid, $k(\phi)$ varies smoothly from 1 for liquid to 0 for solid. Consequently, $k(\phi)$ is the counterpart of the present function ϕ_1 – both of them indicate the fluid phase in which the particles can dissolve. The main distinguishing feature compared to the [54]-model is that the present model deals with three instead of only two phases. Therefore, the present model is classifiable as an extension of the two-phase model in [54] to a multi-phase setting.

5.2.2.3 The combined pore-scale phase-field model

The Problems 5.4 and 5.6 assume that either the phase-fields Φ or the concentration u are given. Their coupling results in the following problem.

Problem 5.8. *Given the parameters $\alpha, \xi, D, \delta, \rho > 0$, the functions $G_i(\Phi, u)$ defined by (5.20), the potential $W(\Phi)$ defined by (5.9), the driving forces $f_i(\Phi, u)$ defined by (5.16) and (5.19), the interpolation-function $g_0(\Phi)$ defined by (5.27), and the initial conditions $\Phi_0 = (\phi_{1,0}, \phi_{2,0}, \phi_{3,0}) : \mathcal{P} \rightarrow \mathcal{S}$ and $u_0 : \mathcal{P} \rightarrow \mathbb{R}$, find the phase-fields $\Phi = (\phi_1, \phi_2, \phi_3)$ and the concentration u satisfying*

$$\begin{aligned}
\alpha \xi^2 \partial_t \phi_i - \frac{3}{4} \xi^2 \Delta \phi_i + G_i(\Phi, u) &= 0 && \text{in } J(T) \times \mathcal{P}, \\
\partial_t((\phi_1 + \delta)u) - D \nabla \cdot ((\phi_1 + \delta) \nabla u) - \rho g_0(\Phi) \partial_t \phi_1 &= 0 && \text{in } J(T) \times \mathcal{P}, \\
-\frac{3}{4} \xi^2 \nabla \phi_i \cdot n_{\mathcal{P}} &= 0 && \text{on } J(T) \times \Gamma_{\mathcal{P}}, \\
-D(\phi_1 + \delta) \nabla u \cdot n_{\mathcal{P}} &= 0 && \text{on } J(T) \times \Gamma_{\mathcal{P}}, \\
\Phi(0, x) &= \Phi_0(x) && \text{in } \mathcal{P}, \\
u(0, x) &= u_0(x) && \text{in } \mathcal{P}.
\end{aligned} \tag{5.37}$$

5.2.2.4 Analysis of the Problem 5.4

In this subsection it is proven that, firstly, the subspace \mathcal{S} of the admissible states of Φ is an invariant subspace of the solution operator $\Phi_0 \mapsto \Phi$ of Problem 5.4, secondly, if a classical solution Φ to Problem 5.4 exists and the given data u is bounded, then the increase of the system's free energy U (defined in (5.8)) is bounded as well.

Let $\langle \cdot, \cdot \rangle_{\mathcal{P}}$ denote the dual pairing in $H^1(\mathcal{P})$. Using standard notation, define the function-spaces

$$\begin{aligned}
\mathcal{V}(T) &:= L_2(J(T); H^1(\mathcal{P})) \cap H^1(J(T); H^1(\mathcal{P})^*), \\
\mathcal{W}(T) &:= \{V = (v_1, v_2, v_3) \in (L_\infty(J(T) \times \mathcal{P}))^3 \mid \\
&\quad V(t, x) \in \mathcal{S} \text{ for a.e. } (t, x) \in J(T) \times \mathcal{P}\},
\end{aligned} \tag{5.38}$$

and the abbreviations

$$\begin{aligned}
\langle v, w \rangle &= \langle v, w \rangle_{J(T) \times \mathcal{P}} = \int_{J(T)} \langle v, w \rangle_{\mathcal{P}} dt, \\
(v, w) &= (v, w)_{J(T) \times \mathcal{P}} = \int_{J(T) \times \mathcal{P}} v w dx dt, \\
\| \cdot \|_{r, T} &= \| \cdot \|_{L_r(J(T) \times \mathcal{P})} \text{ for } 1 \leq r \leq \infty.
\end{aligned} \tag{5.39}$$

The Problem 5.4 has the following weak formulation.

Problem 5.9. *Given the parameters $\alpha, \xi > 0$, the concentration $u \in L_\infty(J(T) \times \mathcal{P})$, the functions $G_i(\Phi, u)$ defined by (5.20), the potential $W(\Phi)$ defined by (5.9), the driving forces $f_i(\Phi, u)$ defined by (5.16) and (5.19), and the initial condition $\Phi_0 = (\phi_{1,0}, \phi_{2,0}, \phi_{3,0}) \in \mathcal{S}$ for a.e. $x \in \mathcal{P}$, find the phase-fields $\Phi = (\phi_1, \phi_2, \phi_3) \in \mathcal{V}(T)^3$ such that the initial condition is satisfied and such that the three equations*

$$\langle \alpha \xi^2 \partial_t \phi_i, v_i \rangle + \left(\frac{3}{4} \xi^2 \nabla \phi_i, \nabla v_i \right) + (G_i(\Phi, u), v_i) = 0 \tag{5.40}$$

hold true for all test-functions $v_i \in L_2(J(T); H^1(\mathcal{P}))$.

Theorem 5.10. *The Problem 5.9 is uniquely solvable. The unique weak solution Φ satisfies*

$$\Phi \in \mathcal{V}(T)^3 \cap C(\overline{J(T)}; L_2(\mathcal{P}))^3 \cap \mathcal{W}(T). \quad (5.41)$$

Proof. This proof follows the outline of the proof of Theorem 2 in Section 9.2 of [28]. It aims at applying Banach's fixed point theorem to the solution operator \mathcal{T} of a linearized version of the weak Problem 5.9 in the space

$$X_T := C(\overline{J(T)}; L_2(\mathcal{P}))^3 \cap \mathcal{W}(T) \quad (5.42)$$

with the norm

$$\|V\|_{X_T} := \sum_{i \in I} \max_{t \in \overline{J(T)}} \|v_i(t)\|_{L_2(\mathcal{P})}, \quad V = (v_1, v_2, v_3) \in X_T. \quad (5.43)$$

Step one. Instead of the non-linear system (5.40), consider the linear system

$$\langle \alpha \xi^2 \partial_t \phi_i, v_i \rangle + \left(\frac{3}{4} \xi^2 \nabla \phi_i, \nabla v_i \right) + (L \phi_i, v_i) = (L \hat{\phi}_i, v_i) - (G_i(\hat{\Phi}, u), v_i) \quad (5.44)$$

with the initial condition and the given concentration $u \in L_\infty(J(T) \times \mathcal{P})$ of the weak Problem 5.9, prescribed input data $\hat{\Phi} = (\hat{\phi}_1, \hat{\phi}_2, \hat{\phi}_3) \in \mathcal{W}(T)$, and a constant $L > 0$ which is specified in the following. Since $G_i(\hat{\Phi}, u) \in L_2(J(T) \times \mathcal{P})$, Theorem 10.3 and Lemma 10.4 of [51] (or Lemma 7.3 of [52]) imply that a unique weak solution $\phi_i \in \mathcal{V}(T) \cap C(\overline{J(T)}; L_2(\mathcal{P}))$ of (5.44) exists for $i \in I$.

Step two. This step shows that the solution $\Phi = (\phi_1, \phi_2, \phi_3)$ satisfies $\Phi \in \mathcal{W}(T)$. Summing up the three equations (5.44) with the test-functions $v_i = v \chi_{t_0} = (\phi_1 + \phi_2 + \phi_3 - 1) \chi_{t_0}$ with the indicator-function χ_{t_0} of the time-interval $J(t_0) = (0, t_0] \subseteq (0, T] = J(T)$ yields, since $v(0) = 0$, $\sum_{i \in I} (\hat{\phi}_i, v) = 1$ and $\sum_{i \in I} (G_i(\hat{\Phi}, u), v) = 0$,

$$\begin{aligned} 0 &= \sum_{i \in I} \langle \alpha \xi^2 \partial_t \phi_i, v \rangle + \sum_{i \in I} \left(\frac{3}{4} \xi^2 \nabla \phi_i, \nabla v \right) + \sum_{i \in I} (L \phi_i, v) \\ &\quad - \sum_{i \in I} (L \hat{\phi}_i, v) + \sum_{i \in I} (G_i(\hat{\Phi}, u), v) \\ &= \frac{\alpha \xi^2}{2} \left(\|v(t_0)\|_{L_2(\mathcal{P})}^2 - \|v(0)\|_{L_2(\mathcal{P})}^2 \right) + \frac{3}{4} \xi^2 \|\nabla v\|_{2, t_0}^2 \\ &\quad + \sum_{i \in I} (L \phi_i, v) - (L, v) \\ &= \frac{\alpha \xi^2}{2} \|v(t_0)\|_{L_2(\mathcal{P})}^2 + \frac{3}{4} \xi^2 \|\nabla v\|_{2, t_0}^2 + L \|v\|_{2, t_0}^2. \end{aligned} \quad (5.45)$$

Hence, $\sum_{i \in I} \phi_i(t, x) = 1$ for a.e. $(t, x) \in J(T) \times \mathcal{P}$.

Define the cut-off function $[\cdot]_- : x \mapsto [x]_- = \min(0, x)$ and fix

$$L \geq 12 + 4\alpha \xi c_{u,0} (\|u\|_{\infty, T} + c_{u,1}). \quad (5.46)$$

Since $\hat{\Phi} \in \mathcal{S}$ it is

$$\begin{aligned} &\sum_{j \in I \setminus \{i\}} (\partial_{\phi_i} - \partial_{\phi_j}) W(\hat{\Phi}) \\ &= 8(\hat{\phi}_i - 3\hat{\phi}_i^2 + 2\hat{\phi}_i^3) - 4(\hat{\phi}_j - 3\hat{\phi}_j^2 + 2\hat{\phi}_j^3) \\ &\quad - 4((1 - \hat{\phi}_i - \hat{\phi}_j) - 3(1 - \hat{\phi}_i - \hat{\phi}_j)^2 + 2(1 - \hat{\phi}_i - \hat{\phi}_j)^3) \\ &= 8(\hat{\phi}_i - 3\hat{\phi}_i^2 + 2\hat{\phi}_i^3) - 4(\hat{\phi}_j - 3\hat{\phi}_j^2 + 2\hat{\phi}_j^3) \\ &\quad - 4(-\hat{\phi}_i + 3\hat{\phi}_i^2 - 2\hat{\phi}_i^3 - \hat{\phi}_j + 3\hat{\phi}_j^2 - 2\hat{\phi}_j^3 + 6\hat{\phi}_i \hat{\phi}_j - 6\hat{\phi}_i^2 \hat{\phi}_j - 6\hat{\phi}_i \hat{\phi}_j^2) \\ &= 12(\hat{\phi}_i - 3\hat{\phi}_i^2 + 2\hat{\phi}_i^3 - 2\hat{\phi}_i \hat{\phi}_j + 2\hat{\phi}_i^2 \hat{\phi}_j + 2\hat{\phi}_i \hat{\phi}_j^2) \\ &= 12 \hat{\phi}_i \underbrace{(1 - 3\hat{\phi}_i + 2\hat{\phi}_i^2)}_{\leq 1} + 2\hat{\phi}_j \underbrace{(-1 + \hat{\phi}_i + \hat{\phi}_j)}_{\leq 0}, \end{aligned} \quad (5.47)$$

and since $\phi_i(0) \geq 0$, the following inequality holds true

$$\begin{aligned}
& \frac{\alpha\xi^2}{2} \|\llbracket \phi_i(t_0) \rrbracket_-\|_{L_2(\mathcal{P})}^2 + \frac{3}{4}\xi^2 \|\nabla \llbracket \phi_i \rrbracket_-\|_{2,t_0}^2 + L \|\llbracket \phi_i \rrbracket_-\|_{2,t_0}^2 \\
&= \langle \alpha\xi^2 \partial_t \phi_i, \llbracket \phi_i \rrbracket_-\chi_{t_0} \rangle + \left(\frac{3}{4}\xi^2 \nabla \phi_i, \nabla \llbracket \phi_i \rrbracket_-\chi_{t_0} \right) + (L\phi_i, \llbracket \phi_i \rrbracket_-\chi_{t_0}) \\
&= (L\hat{\phi}_i - G_i(\hat{\Phi}, u), \llbracket \phi_i \rrbracket_-\chi_{t_0}) \\
&= \left(-L\hat{\phi}_i + \left(\sum_{j \in I \setminus \{i\}} (\partial_{\phi_i} - \partial_{\phi_j}) W(\hat{\Phi}) \right) + f_i(\hat{\Phi}, u), \llbracket \phi_i \rrbracket_-\chi_{t_0} \right) \\
&\leq (\hat{\phi}_i(-L + 12 + 4\alpha\xi|f(u)|), \llbracket \phi_i \rrbracket_-\chi_{t_0}) \\
&\leq (\hat{\phi}_i(-L + 12 + 4\alpha\xi c_{u,0}(\|u\|_{\infty,T} + c_{u,1})), \llbracket \phi_i \rrbracket_-\chi_{t_0}) \\
&\leq 0.
\end{aligned} \tag{5.48}$$

Hence, $\phi_i(t, x) \geq 0$ for a.e. $(t, x) \in J(T) \times \mathcal{P}$.

In summary, $\Phi = (\phi_1, \phi_2, \phi_3) \in \mathcal{W}(T)$.

Step three. Define the solution operator

$$\mathcal{T} : X_T \rightarrow X_T, \quad \mathcal{T}(\hat{\Phi}) = \Phi, \tag{5.49}$$

with the solution $\Phi = (\phi_1, \phi_2, \phi_3)$ of the linear system (5.44) to the input data $\hat{\Phi}$. The following considerations prove that \mathcal{T} is a strict contraction if $T > 0$ is small enough. Using for $i \in I$ the test-functions $v_i = (\phi_{1,i} - \phi_{2,i})\chi_{t_0}$ in (5.44) for the solution $\Phi_1 = (\phi_{1,1}, \phi_{1,2}, \phi_{1,3})$ to the input data $\hat{\Phi}_1 = (\hat{\phi}_{1,1}, \hat{\phi}_{1,2}, \hat{\phi}_{1,3})$, Φ_0 and u , and correspondingly $-v_i$ for the solution $\Phi_2 = (\phi_{2,1}, \phi_{2,2}, \phi_{2,3})$ to the input data $\hat{\Phi}_2 = (\hat{\phi}_{2,1}, \hat{\phi}_{2,2}, \hat{\phi}_{2,3})$, Φ_0 and u , defining $\bar{\phi}_i := \phi_{1,i} - \phi_{2,i}$ and $\hat{\bar{\phi}}_i := \hat{\phi}_{1,i} - \hat{\phi}_{2,i}$, and summing up the six equations yields

$$\begin{aligned}
& \sum_{i \in I} (\alpha\xi^2 \langle \partial_t \bar{\phi}_i, \bar{\phi}_i \chi_{t_0} \rangle + \frac{3}{4}\xi^2 (\nabla \bar{\phi}_i, \nabla \bar{\phi}_i \chi_{t_0}) + L (\bar{\phi}_i, \bar{\phi}_i \chi_{t_0})) \\
&= \sum_{i \in I} L (\hat{\bar{\phi}}_i, \bar{\phi}_i \chi_{t_0}) - \sum_{i=1,3} (f_i(\hat{\Phi}_1, u) - f_i(\hat{\Phi}_2, u), \bar{\phi}_i \chi_{t_0}) \\
&\quad - \sum_{i \in I} \sum_{j \in I \setminus \{i\}} ((\partial_{\phi_i} - \partial_{\phi_j}) (W(\hat{\Phi}_1) - W(\hat{\Phi}_2)), \bar{\phi}_i \chi_{t_0}).
\end{aligned} \tag{5.50}$$

The equality of the initial conditions and of the input data u , the Lipschitz continuities (5.12) of $\partial_{\phi_i} W(\Phi)$ and (5.21) of $f_i(\Phi, u)$, and Hölder's and Young's inequality for an arbitrary $\eta > 0$ yield

$$\begin{aligned}
& \sum_{i \in I} \left(\alpha\xi^2 \|\bar{\phi}_i(t_0)\|_{L_2(\mathcal{P})}^2 + \frac{3}{4}\xi^2 \|\nabla \bar{\phi}_i\|_{2,t_0}^2 + L \|\bar{\phi}_i\|_{2,t_0}^2 \right) \\
&\leq L \sum_{i \in I} \|\hat{\bar{\phi}}_i\|_{2,t_0} \|\bar{\phi}_i\|_{2,t_0} \\
&\quad + 4\alpha\xi c_{u,0}(\|u\|_{\infty,t_0} + c_{u,1}) \sum_{i,j=1,3} \|\hat{\bar{\phi}}_j\|_{2,t_0} \|\bar{\phi}_i\|_{2,t_0} \\
&\quad + 42 \sum_{i \in I} \sum_{j \in I \setminus \{i\}} \left(\|\hat{\bar{\phi}}_i\|_{2,t_0} + \|\hat{\bar{\phi}}_j\|_{2,t_0} \right) \|\bar{\phi}_i\|_{2,t_0} \\
&\leq C(L, 4\alpha\xi c_{u,0}(\|u\|_{\infty,t_0} + c_{u,1}), 42, \eta) \sum_{i \in I} \|\hat{\bar{\phi}}_i\|_{2,t_0}^2 + \eta \sum_{i \in I} \|\bar{\phi}_i\|_{2,t_0}^2.
\end{aligned} \tag{5.51}$$

Fixing $\eta \leq L$ results in

$$\begin{aligned}
\sum_{i \in I} \|\bar{\phi}_i(t_0)\|_{L_2(\mathcal{P})}^2 &\leq C \sum_{i \in I} \|\hat{\bar{\phi}}_i\|_{2,t_0}^2 \\
&\leq CT \sum_{i \in I} \max_{t \in \overline{J(T)}} \|\hat{\bar{\phi}}_i(t)\|_{L_2(\mathcal{P})}^2
\end{aligned} \tag{5.52}$$

for each $t_0 \in \overline{J(T)}$. The constant $C > 0$ is independent of the initial condition Φ_0 , the solutions Φ_1 and Φ_2 and the input data $\hat{\Phi}_1$ and $\hat{\Phi}_2$. Maximizing the left-hand side with respect to t_0 yields

$$\|\mathcal{T}(\hat{\Phi}_1) - \mathcal{T}(\hat{\Phi}_2)\|_{X_T} = \|\Phi_1 - \Phi_2\|_{X_T} \leq \sqrt{CT} \|\hat{\Phi}_1 - \hat{\Phi}_2\|_{X_T}. \quad (5.53)$$

Consequently, the solution operator \mathcal{T} is a strict contraction as long as $T > 0$ is so small such that $\sqrt{CT} < 1$.

Step four. Fix $t_0 \in J(T)$ such that $\sqrt{CT_0} < 1$ and hence $\mathcal{T} : X_{t_0} \rightarrow X_{t_0}$ is a strict contraction. Banach's fixed-point theorem proves the existence of a solution to the non-linear weak Problem 5.9 in the time-space cylinder $J(t_0) \times \mathcal{P}$. Since the choice of t_0 is independent of the solution and the initial data, this argumentation is repeatable if necessary. That is if $t_0 < T$. A solution exists not only on $(0, t_0] \times \mathcal{P}$ but also on $(t_0, 2t_0] \times \mathcal{P}, \dots, ([T/t_0] t_0, T] \times \mathcal{P}$, where the solution in the end of a preceding time-interval defines the initial condition of a subsequent time-interval. Therefore, a solution to the weak Problem 5.9 exists in the space $\mathcal{W}(T) \cap \mathcal{V}(T)^3 \cap C(\overline{J(T)}; L_2(\mathcal{P}))^3$. The solution's uniqueness follows from the application of Gronwall's inequality to (5.51). \square

The previous theorem proved that the solution Φ of the weak Problem 5.9 is in an admissible state almost everywhere in the time-space cylinder. The following theorem shows that if a classical solution Φ to the Problem 5.4 exists, then the increase of the system's free energy U defined in (5.8) has a bounded increase.

Theorem 5.11. *For a classical solution $\Phi = (\phi_1, \phi_2, \phi_3)$ of the Problem 5.4, the increase of the system's free energy U defined in (5.8) is limited,*

$$\frac{d}{dt} U(\Phi) \leq \begin{cases} -C_0 \sum_{i \in I} \|\partial_t \phi_i\|_{L_2(\mathcal{P})}^2 \\ \quad \text{if } (u = c_{u,1} \wedge \phi_1 \phi_3 = 0) \forall (t, x) \in J(T) \times \mathcal{P}, \\ C_1 \|\phi_1 \phi_3 (u - c_{u,1})\|_{L_2(\mathcal{P})}^2 - C_2 \sum_{i \in I} \|\partial_t \phi_i\|_{L_2(\mathcal{P})}^2 \quad \text{else,} \end{cases} \quad (5.54)$$

with constants $C_0, C_1, C_2 > 0$.

Proof. The evolution equation of the Problem 5.4, $\partial_t(\phi_1 + \phi_2 + \phi_3) = \partial_t 1 = 0$, the definition of the driving forces (5.16) and (5.19), and Young's inequality for an arbitrary $\eta > 0$ yield

$$\begin{aligned} \frac{d}{dt} U(\Phi) &= \frac{d}{dt} \int_{\mathcal{P}} 3W(\Phi) + \frac{3}{8} \xi^2 \sum_{i \in I} |\nabla \phi_i|^2 dx \\ &= \int_{\mathcal{P}} 3\partial_t W(\Phi) + \frac{3}{8} \xi^2 \sum_{i \in I} \partial_t |\nabla \phi_i|^2 dx \\ &= \int_{\mathcal{P}} \sum_{i \in I} (3\partial_{\phi_i} W(\Phi) \partial_t \phi_i + \frac{3}{4} \xi^2 \nabla \phi_i \cdot \nabla (\partial_t \phi_i)) dx \\ &= \int_{\mathcal{P}} \sum_{i \in I} (\partial_{\phi_i} W(\Phi) (2\partial_t \phi_i - \partial_t \phi_j - \partial_t \phi_k) + \frac{3}{4} \xi^2 \nabla \phi_i \cdot \nabla (\partial_t \phi_i)) dx \\ &= \int_{\mathcal{P}} \sum_{i \in I} ((2\partial_{\phi_i} - \partial_{\phi_j} - \partial_{\phi_k}) W(\Phi) - \frac{3}{4} \xi^2 \Delta \phi_i) \partial_t \phi_i dx \\ &= \int_{\mathcal{P}} \sum_{i \in I} (-f_i(\Phi, u) \partial_t \phi_i - \alpha \xi^2 (\partial_t \phi_i)^2) dx \\ &= \int_{\mathcal{P}} 4\alpha \xi \phi_1 \phi_3 f(u) \partial_t (\phi_3 - \phi_1) + \sum_{i \in I} -\alpha \xi^2 (\partial_t \phi_i)^2 dx \\ &\leq \frac{1}{4\eta} \|4\phi_1 \phi_3 f(u)\|_{L_2(\mathcal{P})}^2 - (\alpha - \eta \alpha^2) \xi^2 \sum_{i \in I} \|\partial_t \phi_i\|_{L_2(\mathcal{P})}^2 \\ &\leq \frac{c_{u,0}}{4\eta} \|u - c_{u,1}\|_{L_2(\mathcal{P})}^2 - (\alpha - \eta \alpha^2) \xi^2 \sum_{i \in I} \|\partial_t \phi_i\|_{L_2(\mathcal{P})}^2. \end{aligned} \quad (5.55)$$

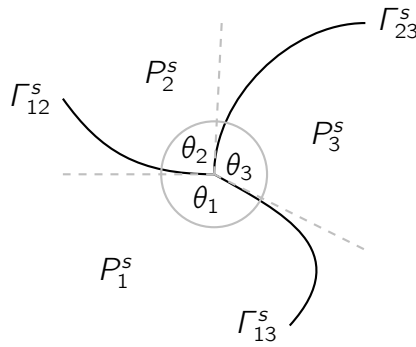


Figure 5.3: The three phases and their interfaces.

Consequently, if $0 < \eta \leq \alpha^{-1}$, the boundedness of u results in an upper bound for the free energy's increase. In particular, if $f(u) = 0$ that is if $u = c_{u,1}$ in regions of \mathcal{P} where $\phi_1\phi_3 > 0$ then the free energy decreases monotonically. \square

Remark 5.12. *The analysis of Problem 5.6 for the concentration u with given phase-fields and of the combined problem 5.8 is a part of future research.*

5.2.3 The asymptotic behavior for $\xi \rightarrow 0$

In this subsection the formal asymptotic limit of Problem 5.8 for the parameter $\xi \rightarrow 0$ is analyzed. Since ξ is proportional to the width of the interface regions in Problem 5.8, the matched asymptotic expansion method describes the transition from the phase-field model to its sharp interface limit. As usual in the literature, e.g. [8], the method realizes a spatial decomposition: firstly, the outer regions far away from the interfaces, secondly, the inner regions near the interfaces of two phases far away from the other interfaces and, thirdly, the inner regions near triple junctions where three interfaces meet. Figure 5.3 illustrates the situation. The variables are expanded in powers of ξ in each region. In a region where two expansions are valid, the expansions are matched.

Let $(\Phi_\xi, u_\xi) = (\phi_{1,\xi}, \phi_{2,\xi}, \phi_{3,\xi}, u_\xi)$ be a sufficiently smooth solution to Problem 5.8 with the parameter $\xi > 0$ and with $\delta = \xi$. The following considerations show that if $\xi \rightarrow 0$ then the pore-space is subdivided into regions where $\Phi_\xi \approx \bar{P}_1^d = (1, 0, 0)$, $\bar{P}_2^d = (0, 1, 0)$ or $\bar{P}_3^d = (0, 0, 1)$, that is into regions occupied by an approximately pure fluid P_1 , by an approximately pure fluid P_2 and into regions occupied by an approximately pure solid P_3 . In the limit, the interfaces $\Gamma_{12}^d(t)$ and $\Gamma_{23}^d(t)$ evolve with speed equal to their mean curvature. The evolution of interface $\Gamma_{13}^d(t)$ is influenced by the precipitation reaction. It evolves with the normal velocity $-\sigma\kappa_{13} - f(c)$. Hence, these limit-interfaces evolve with normal velocities that fulfill the kinetic conditions (5.3) in the sharp-interface setting. Due to the fact that the potential $W(\Phi)$ is symmetric, and consequently the surface tensions of the three interfaces are equal, [8] shows that the angles between the limit-interfaces in triple junctions must be of 120° in a two-dimensional spatial setting. Furthermore, it is shown that the limit-solution u_ξ satisfies in the region occupied by the approximately pure fluid P_1 the evolution equation, and on the limit-interfaces the Rankine-Hugoniot conditions of the sharp-interface problem 5.1.

5.2.3.1 The expansions and their matching conditions

The outer expansions (Φ^{out}, u^{out}) to the solution (Φ_ξ, u_ξ) are given by

$$\begin{aligned}\Phi^{out}(t, x) &= (\phi_1^{out}(t, x), \phi_2^{out}(t, x), \phi_3^{out}(t, x)) \\ &= (\sum_{i=0}^{\infty} \xi^i \phi_{1,i}^{out}(t, x), \sum_{i=0}^{\infty} \xi^i \phi_{2,i}^{out}(t, x), \sum_{i=0}^{\infty} \xi^i \phi_{3,i}^{out}(t, x)), \\ u^{out}(t, x) &= \sum_{i=0}^{\infty} \xi^i u_i^{out}(t, x).\end{aligned}\quad (5.56)$$

Near an interface far away from the other interfaces, the coordinates $x \in \mathcal{P}$ are transformed into local curvilinear coordinates. The transformation is derived from the level sets $\Gamma_{i,\xi}^d(t)$, $i \in I$,

$$\Gamma_{i,\xi}^d(t) = \{x \in \mathcal{P} \mid \phi_{i,\xi}(x) = 0.5\}.\quad (5.57)$$

It is assumed that the level sets $\Gamma_{i,\xi}^d(t)$ are sufficiently smooth and for $\xi \rightarrow 0$ smoothly approach limit-interfaces $\Gamma_i^\ell(t)$, where the index ℓ denotes 'limit' as s denotes 'sharp' and d 'diffuse'. Exemplarily considered is the situation for the interface $\Gamma_{13}^d(t)$ that separates the two fluids $P_1^d(t)$ and $P_3^d(t)$ and that is far away from the other interfaces. It is assumed that $\Gamma_{13,\xi}^d(t) = \Gamma_{1,\xi}^d(t) = \Gamma_{3,\xi}^d(t) \rightarrow \Gamma_{13}^\ell(t)$ smoothly for $\xi \rightarrow 0$. For $x \in \mathcal{P}$, let $r(t, x)$ denote the signed distance from x to $\Gamma_{13,\xi}^d(t)$, where r is negative for x in P_1 and positive in P_3 . In addition, let s be a measure of arc length from some fixed point, and let $y_\xi(t, s)$ be the point on $\Gamma_{13,\xi}^d(t)$ at arc length s . Then (r, s) is a local orthogonal coordinate system and any point x in a neighborhood of $\Gamma_{13,\xi}^d(t)$ is representable by

$$x = y_\xi(t, s) + r n_\xi(t, s),\quad (5.58)$$

where $n_\xi(t, s)$ is the normal to $\Gamma_{13,\xi}^d(t)$ in $y_\xi(t, s)$ pointing into $P_3^d(t)$. [12] shows that the coordinates $(r, s) = (r, s)(t, x)$ satisfy

$$|\nabla r| = 1, \quad \nabla r \cdot \nabla s = 0, \quad \partial_t r = -v^n, \quad \Delta r = \frac{\kappa + 2\Pi r}{1 + \kappa r + \Pi r^2},\quad (5.59)$$

where v^n , κ and Π denote the normal velocity, the mean and the Gaussian curvature of the moving interface $\Gamma_{13,\xi}^d(t)$. It is assumed that the normal velocity v^n and the mean curvature κ satisfy the expansions

$$v^n = v_0^n + \mathcal{O}(\xi), \quad \kappa = \kappa_0 + \mathcal{O}(\xi),\quad (5.60)$$

where v_0^n and κ_0 denote the normal velocity and the mean curvature of $\Gamma_{13}^\ell(t)$. Finally introduce the coordinates $z = \xi^{-1}r$ and the inner expansions ϕ_1^{in} of $\phi_{1,\xi}$ and u^{in} of u_ξ ,

$$\begin{aligned}\phi_1^{in}(t, z, s) &= \sum_{i=0}^{\infty} \xi^i \phi_{1,i}^{in}(t, z, s), \\ u^{in}(t, z, s) &= \sum_{i=0}^{\infty} \xi^i u_i^{in}(t, z, s).\end{aligned}\quad (5.61)$$

In an overlapping region the inner and the outer expansions shall describe the same function. This is realized by matching conditions. For that purpose, the outer expansions are written in terms of the local coordinates (t, z, s) , where the outer normal $n_\xi(t, s)$ and the point $y_\xi(t, s)$ (see (5.58)) are expanded as follows

$$\begin{aligned}n_\xi(t, s) &= \sum_{i=0}^{\infty} \xi^i n_i(t, s), \\ y_\xi(t, s) &= \sum_{i=0}^{\infty} \xi^i n_{i-1}(t, s) y_i(t, s), \quad n_{-1} \equiv 1.\end{aligned}\quad (5.62)$$

Let $y_{-1/2}$ denote the limit at the free interface $\Gamma_{13,\xi}^d(t)$ from the side of P_1 ($r, z < 0$) and $y_{+1/2}$ the one on the right ($r, z > 0$), that is on the side of P_3 . In [12] it is shown that equating the inner- and the outer-expansions yields the following matching conditions

$$\begin{aligned} \lim_{z \rightarrow \pm\infty} \phi_{1,0}^{in}(t, z, s) &= \phi_{1,0}^{out}(t, y_{\pm 1/2}), \\ \lim_{z \rightarrow \pm\infty} (\phi_{1,1}^{in}(t, z, s) - (\nabla \phi_{1,0}^{out}(t, y_{\pm 1/2}) \cdot n_0)(y_1 + z)) &= \phi_{1,1}^{out}(t, y_{\pm 1/2}), \\ \lim_{z \rightarrow \pm\infty} \partial_z \phi_{1,0}^{in}(t, z, s) &= 0, \\ \lim_{z \rightarrow \pm\infty} \partial_z \phi_{1,1}^{in}(t, z, s) &= \nabla \phi_{1,0}^{out}(t, y_{\pm 1/2}) \cdot n_0, \end{aligned} \quad (5.63)$$

and

$$\begin{aligned} \lim_{z \rightarrow \pm\infty} u_0^{in}(t, z, s) &= u_0^{out}(t, y_{\pm 1/2}), \\ \lim_{z \rightarrow \pm\infty} (u_1^{in}(t, z, s) - (\nabla u_0^{out}(t, y_{\pm 1/2}) \cdot n_0)(y_1 + z)) &= u_1^{out}(t, y_{\pm 1/2}), \\ \lim_{z \rightarrow \pm\infty} \partial_z u_0^{in}(t, z, s) &= 0, \\ \lim_{z \rightarrow \pm\infty} \partial_z u_1^{in}(t, z, s) &= \nabla u_0^{out}(t, y_{\pm 1/2}) \cdot n_0. \end{aligned} \quad (5.64)$$

For the inner expansions $w^{in}(t, z, s)$, $w^{in} \in \{\phi_1^{in}, \phi_2^{in}, \phi_3^{in}, u^{in}\}$, the following relations hold

$$\begin{aligned} \partial_t w^{in} &= -\frac{1}{\xi} v^n \partial_z w^{in} + (\partial_t + \partial_t s \cdot \nabla_s) w^{in}, \\ \nabla_x \cdot (K \nabla_x w^{in}) &= \frac{1}{\xi^2} \partial_z \cdot (K \partial_z w^{in}) + \frac{1}{\xi} (\Delta_x r) K \partial_z w^{in} + \mathcal{O}(1), \end{aligned} \quad (5.65)$$

where $\Delta_x r = \kappa_0 + \mathcal{O}(\xi^1)$ holds in a small neighborhood of $\Gamma_{13,\xi}^d(t)$, and where K is a sufficiently smooth diffusion tensor.

5.2.3.2 The outer expansions

Substituting the outer expansions (5.56) into the first evolution equation of (5.37) of Problem 5.8 yields a sequence of problems. For $i \in I$ the $\mathcal{O}(1)$ problem consists of the equation

$$\sum_{j \in I \setminus \{i\}} (\partial_{\phi_i} - \partial_{\phi_j}) W(\phi_{1,0}^{out}, \phi_{2,0}^{out}, \phi_{3,0}^{out}) = 0 \text{ in } J(T) \times \mathcal{P}. \quad (5.66)$$

The solutions that are considered are

$$\Phi_0^{out} = (\phi_{1,0}^{out}, \phi_{2,0}^{out}, \phi_{3,0}^{out}) \in \{\bar{P}_1^d, \bar{P}_2^d, \bar{P}_3^d\} = \{(1, 0, 0), (0, 1, 0), (0, 0, 1)\}. \quad (5.67)$$

The zeros \bar{P}_i^d , $i \in I$, minimize the potential in (5.66). The remaining zeros $\tilde{\Phi}$, as e.g. $(\frac{1}{2}, \frac{1}{2}, 0)$ and $(\frac{1}{3}, \frac{1}{3}, \frac{1}{3})$, are not considered because they are unstable due to

$$\partial_{\phi_i} \sum_{j \in I \setminus \{i\}} (\partial_{\phi_i} - \partial_{\phi_j}) W(\tilde{\Phi}) < 0 \text{ for } i \in I. \quad (5.68)$$

Therefore, substituting the outer expansions into the first evolution equation of (5.37) subdivides the pore-space \mathcal{P} into P_{1-} , P_{2-} and P_{3-} regions.

The problem at $\mathcal{O}(\xi^1)$ for $i \in I$ reads

$$\begin{aligned} &8\phi_{i,1}^{out} (1 - 6\phi_{i,0}^{out} + 6(\phi_{i,0}^{out})^2) - 4 \sum_{\ell \in I \setminus \{i\}} \phi_{\ell,1}^{out} (1 - 6\phi_{\ell,0}^{out} + 6(\phi_{\ell,0}^{out})^2) \\ &= \begin{cases} -4\alpha \phi_{1,0}^{out} \phi_{3,0}^{out} f(u_0^{out}), & \text{if } i = 1, \\ 0, & \text{if } i = 2, \\ 4\alpha \phi_{1,0}^{out} \phi_{3,0}^{out} f(u_0^{out}), & \text{if } i = 3. \end{cases} \end{aligned} \quad (5.69)$$

If $\Phi_0^{out} \in \{\overline{P}_1^d, \overline{P}_2^d, \overline{P}_3^d\}$, the left-hand side is equal to $8\phi_{i,1}^{out} - 4\sum_{\ell \in I \setminus \{i\}} \phi_{\ell,1}^{out}$ and the right-hand side vanishes. Consequently, if $\Phi_0^{out} \in \{\overline{P}_1^d, \overline{P}_2^d, \overline{P}_3^d\}$ then the three equations yield $\phi_{1,1}^{out} = \phi_{2,1}^{out} = \phi_{3,1}^{out}$. The condition $\sum_{j=0}^{\infty} \xi^j \sum_{i \in I} \phi_{i,j}^{out} = 1$ yields at $\mathcal{O}(\xi^1)$ the condition $\sum_{i \in I} \phi_{i,1}^{out} = 0$. In summary, if $\Phi_0^{out} \in \{\overline{P}_1^d, \overline{P}_2^d, \overline{P}_3^d\}$, these considerations yield $\phi_{1,1}^{out}, \phi_{2,1}^{out}, \phi_{3,1}^{out} = 0$.

Define

$$P_i^{out}(t) := \{x \in \mathcal{P} \mid \Phi_0^{out}(t, x) \in \overline{P}_i^d\}, \text{ for } t \in \overline{J(\overline{T})}. \quad (5.70)$$

As already shown in [44], if $\Phi_0^{out} = \overline{P}_1^d$, that is if $\phi_{1,0}^{out} = 1$, substituting the outer expansions into the second evolution equation of (5.37) yields, since $\delta = \xi$, at $\mathcal{O}(\xi^0)$ the equation

$$\partial_t u_0^{out} - D\Delta u_0^{out} = 0 \text{ in } J(T) \times P_1^{out}(t), \quad (5.71)$$

due to $\partial_t \phi_{1,0}^{out} = 0$ and $g_0(1, 0, 0) = 1$. Hence, the sharp-interface model's evolution equation in (5.2) for the concentration in $J(T) \times P_1^s(t)$ is recovered.

If $\Phi_0^{out} \in \{\overline{P}_2^{out}, \overline{P}_3^{out}\}$, no equation at $\mathcal{O}(\xi^0)$ results from the substitution, since $\phi_{1,0}^{out} = 0$. At $\mathcal{O}(\xi^1)$ the problem reads

$$\partial_t u_0^{out} - D\Delta u_0^{out} = 0 \text{ in } J(T) \times P_2^{out}(t) \text{ and in } J(T) \times P_3^{out}(t), \quad (5.72)$$

since $\delta = \xi$ and due to the fact that $\phi_{1,0}^{out}, \phi_{1,1}^{out} = 0$ if $\Phi_0^{out} \in \{\overline{P}_2^d, \overline{P}_3^d\}$.

5.2.3.3 The inner expansions ϕ_i^{in} at $\mathcal{O}(\xi^0)$ near $\Gamma_{12,\xi}^d(t)$, $\Gamma_{13,\xi}^d(t)$ and $\Gamma_{23,\xi}^d(t)$

Near the interface of $\Gamma_{13,\xi}^d(t)$ that separates $P_1^{out}(t)$ and $P_3^{out}(t)$ in a region far away from the remaining interface regions $\Gamma_{12,\xi}^d(t)$, $\Gamma_{23,\xi}^d(t)$ and $\Gamma_{123,\xi}^d(t)$, it is assumed that $\phi_2^{in} = 0$. Consequently, substituting the inner expansions (5.61) into the first evolution equation of (5.37) results for $i = 1$ in an equation that is, due to $\phi_2^{in} = 0$ and hence $\phi_3^{in} = 1 - \phi_1^{in}$, equivalent to

$$\alpha \xi^2 \partial_t \phi_1^{in} - \frac{3}{4} \xi^2 \Delta \phi_1^{in} + 6\rho'(\phi_1^{in}) + 4\xi \alpha \sqrt{\rho(\phi_1^{in})} f(u) = 0, \quad (5.73)$$

where $\rho(\phi) = \phi^2(1 - \phi)^2$. Following the argumentation in [54], that is substituting the inner expansions (5.61) into (5.73) and collecting the terms of order ξ^0 yields the second-order ordinary differential equation

$$-\frac{3}{4} \partial_z^2 \phi_{1,0}^{in} + 6\rho'(\phi_{1,0}^{in}) = 0. \quad (5.74)$$

Due to the first matching condition in (5.63), equation (5.74) is supplemented by the interface conditions

$$\phi_{1,0}^{in}(t, -\infty, s) = 1, \quad \phi_{1,0}^{in}(t, \infty, s) = 0. \quad (5.75)$$

Due to the condition $\phi_1^{in}(t, 0, s) = \frac{1}{2}$ and the assumption that $\Gamma_{13,\xi}^d(t)$ converges for $\xi \rightarrow 0$ to $\Gamma_{13}^d(t)$, $\phi_{1,0}^{in}(t, 0, s) = \frac{1}{2}$ as well. Since $\rho(\frac{1}{2} + z) = \rho(\frac{1}{2} - z)$ and since ρ is non-negative, $\frac{3}{8} \partial_z (\partial_z \phi_{1,0}^{in})^2 = 6\partial_z \rho(\phi_{1,0}^{in})$, and due to the first and the third matching conditions in (5.63), the second-order problem (5.74) reduces to the initial value problem

$$\partial_z \phi_{1,0}^{in} = -4\sqrt{\rho(\phi_{1,0}^{in})} = -4\phi_{1,0}^{in} (1 - \phi_{1,0}^{in}), \quad \phi_{1,0}^{in}(0) = \frac{1}{2}. \quad (5.76)$$

Separation of variables yields the unique, strictly decreasing solution

$$\phi_{1,0}^{in}(t, z, s) = \phi_{1,0}^{in}(z) = \frac{1}{1 + \exp(4z)}. \quad (5.77)$$

As a consequence,

$$\phi_{3,0}^{in}(t, z, s) = 1 - \phi_{1,0}^{in}(t, z, s) = \frac{1}{1 + \exp(-4z)}. \quad (5.78)$$

Similar calculations can be carried out near the remaining two interfaces $\Gamma_{12,\xi}^d(t)$ and $\Gamma_{23,\xi}^d(t)$. They result in equivalent expressions for $\phi_{i,0}^{in}(t, z, s)$ and $\phi_{j,0}^{in}(t, z, s)$ near $\Gamma_{ij,\xi}^d(t)$.

5.2.3.4 The inner expansions u^{in} at $\mathcal{O}(\xi^{-2})$ near $\Gamma_{12,\xi}^d(t)$ and $\Gamma_{13,\xi}^d(t)$

The following argumentation holds in the neighborhood of $\Gamma_{12,\xi}^d(t)$ as well as in the one of $\Gamma_{13,\xi}^d(t)$. For $i \in \{2, 3\}$ fixed, substituting the inner expansions (5.61) in the neighborhood of $\Gamma_{i,\xi}^d(t)$ into the second evolution equation of (5.37) results at $\mathcal{O}(\xi^{-2})$ in the equation

$$\partial_z (\phi_{1,0}^{in} \partial_z u_0^{in}) = 0. \quad (5.79)$$

As already shown in [44], integration from $-\infty$ to $z \in \mathbb{R}$, the condition $\phi_{1,0}^{in}(t, z, s) > 0 \forall z \in \mathbb{R}$, and the third matching condition in (5.64) yield

$$\partial_z u_0^{in} = 0. \quad (5.80)$$

5.2.3.5 The inner expansions ϕ_i^{in} at $\mathcal{O}(\xi^1)$ near $\Gamma_{12,\xi}^d(t)$, $\Gamma_{13,\xi}^d(t)$ and $\Gamma_{23,\xi}^d(t)$

Following the argumentation in [54], that is substituting the inner expansions (5.61) near the interface $\Gamma_{13,\xi}^d(t)$ into (5.73) and collecting the terms of order ξ^1 yields the equation

$$\underbrace{\left(-\frac{3}{4}\partial_z^2 + 6p''(\phi_{1,0}^{in})\right)}_{=:L(\phi_{1,0}^{in})=L} \phi_{1,1}^{in} = \underbrace{(\alpha v_0^n + \frac{3}{4}\kappa_0)\partial_z \phi_{1,0}^{in} - 4\alpha \phi_{1,0}^{in}(1 - \phi_{1,0}^{in})f(u_0^{in})}_{=:A(\phi_{1,0}^{in})}. \quad (5.81)$$

The equation is supplemented by the condition that $\phi_1(\pm\infty)$ is bounded because of the second matching condition (5.63). The operator L is a Fredholm operator of index zero. Therefore, the Fredholm alternative yields that the equation has a solution iff $A(\phi_{1,0}^{in})$ is orthogonal to the finite-dimensional kernel of L . Because $\partial_z \phi_{1,0}^{in} \in \ker(L)$ (see (5.74)), because $\partial_z \phi_{1,0}^{in} = -4\phi_{1,0}^{in}(1 - \phi_{1,0}^{in})$ holds true, and because v_0^n , κ_0 and u_0^{in} are independent of z , the solvability condition implies

$$\begin{aligned} 0 &= \int_{-\infty}^{\infty} A(\phi_{1,0}^{in}) \partial_z \phi_{1,0}^{in} dz \\ &= (\alpha v_0^n + \frac{3}{4}\kappa_0) \int_{-\infty}^{\infty} (\partial_z \phi_{1,0}^{in})^2 dz - 4\alpha f(u_0^{in}) \int_{-\infty}^{\infty} \phi_{1,0}^{in}(1 - \phi_{1,0}^{in}) \partial_z \phi_{1,0}^{in} dz \\ &= -4(\alpha v_0^n + \frac{3}{4}\kappa_0 + \alpha f(u_0^{in})) \int_{-\infty}^{\infty} \phi_{1,0}^{in}(1 - \phi_{1,0}^{in}) \partial_z \phi_{1,0}^{in} dz \\ &= -4(\alpha v_0^n + \frac{3}{4}\kappa_0 + \alpha f(u_0^{in})) \int_1^0 x(1-x) dx \\ &= \frac{2}{3}(\alpha v_0^n + \frac{3}{4}\kappa_0 + \alpha f(u_0^{in})). \end{aligned} \quad (5.82)$$

Set

$$\alpha := \frac{3}{4}\sigma^{-1}, \quad (5.83)$$

where $\sigma > 0$ describes the surface tension in the sharp-interface problem 5.1 with the kinetic conditions (5.3) of the moving interfaces. The linear growth of the rate-function f and the first matching condition in (5.64) yield

$$v_0^n = -\sigma\kappa_0 - f(u_0^{out}(t, y_{-1/2})) \text{ for } z \rightarrow -\infty. \quad (5.84)$$

Near the interfaces $\Gamma_{12,\xi}^d(t)$ and $\Gamma_{23,\xi}^d(t)$ a similar argumentation leads to the equation

$$\left(-\frac{3}{4}\partial_z^2 + 6p''(\phi_{2,0}^{in})\right)\phi_{2,1}^{in} = (\alpha v_0^n + \frac{3}{4}\kappa_0)\partial_z\phi_{2,0}^{in} \quad (5.85)$$

for $\phi_{2,1}^{in}$. Consequently,

$$v_0^n = -\sigma\kappa_0. \quad (5.86)$$

Therefore, the moving interfaces' kinetic conditions (5.3) of the sharp-interface model are recovered at $\mathcal{O}(\xi^1)$.

5.2.3.6 The inner expansions u^{in} at $\mathcal{O}(\xi^{-1})$ near $\Gamma_{12,\xi}^d(t)$ and $\Gamma_{13,\xi}^d(t)$

Substituting the inner expansions (5.61) in the neighborhood of $\Gamma_{13,\xi}^d(t)$ into the second evolution equation of (5.37) results at $\mathcal{O}(\xi^{-1})$ in the equation

$$-D\partial_z \cdot (\phi_{1,0}^{in}\partial_z u_1^{in}) = v_0^n(u_0^{in} - \rho)\partial_z\phi_{1,0}^{in}, \quad (5.87)$$

since $\partial_z u_0^{in} = 0$, and since $g(\Phi_0^{in}) = 1$ due to $\phi_{2,0}^{in} = 0$. As already shown in [44], since v_0^n , u_0^{in} and ρ are independent of z , integrating from $-\infty$ to ∞ , and the first matching condition in (5.63) imply

$$-D\partial_z u_1^{in} = v_0^n(u_0^{in} - \rho). \quad (5.88)$$

The first and the fourth matching condition in (5.64) yield

$$-D\nabla u_0^{out}(t, y_{-1/2}) \cdot n_0 = v_0^n(u_0^{out}(t, y_{-1/2}) - \rho). \quad (5.89)$$

Since $g(\Phi_0^{in}) = 0$ in the neighborhood of $\Gamma_{12,\xi}^d(t)$, a similar argumentation as in the neighborhood of $\Gamma_{13,\xi}^d(t)$ yields in the neighborhood of $\Gamma_{12,\xi}^d(t)$ the equation

$$-D\nabla u_0^{out}(t, y_{-1/2}) \cdot n_0 = v_0^n u_0^{out}(t, y_{-1/2}). \quad (5.90)$$

Thus, the sharp-interface model's Rankine-Hugoniot conditions in (5.2) at $\Gamma_{12}^s(t)$ and $\Gamma_{13}^s(t)$ are recovered at $\mathcal{O}(\xi^{-1})$.

5.2.3.7 Conclusion

The asymptotic analysis showed that the solution to the limit problem 5.8 for $\xi \rightarrow 0$ approximates the solution of the sharp-interface problem 5.1 with the kinetic conditions (5.3) for the moving interfaces. The analysis of the asymptotic behavior of the solution u_ξ near the interface $\Gamma_{23,\xi}^d(t)$ as well as near triple junctions is a part of future research.

5.3 Upscaling

The pore-scale phase-field Problem 5.8 established in the previous section is able to describe the evolution of the three phases and the diffusion process of the concentration on an arbitrarily large domain with an arbitrary number of phase transition regions. However, from the numerical point of view, the model is not suitable for situations with a large number of phase transition regions. This is due to the fact that in a numerical discretization such a phase transition region needs to be resolved by a very fine computational mesh. This leads to an increasing number of unknowns for an increasing number of phase transition regions. In order to develop a suitable model, a homogenization technique is applied to the Problem 5.8.

For that purpose, the idealized situation with periodically distributed grains and phases in the pore-space with a period of scale $\epsilon > 0$ is considered. The homogenization technique aims at constructing a limit problem for $\epsilon \rightarrow 0$ for a sequence of problems on a varying scale ϵ . This limit problem is used as an approximation to the Problem 5.8 for situations with small but non-vanishing scale ϵ . It bridges the gap between the pore-scale and the scale of the diffusion process

5.3.1 The perforated spatial domain

Let $\epsilon > 0$ be a small positive parameter. The spatial domain $\Omega \subset \mathbb{R}^d$, $d \in \{2, 3\}$, with boundary $\Gamma_\Omega = \partial\Omega$, includes no longer only one perforation but many. The grains – these perforations – are small of scale ϵ . Therefore, the ration of the scale of the microstructure and the scale of the diffusion process is of order ϵ .

The grains are periodically distributed with a period of scale ϵ . In order to model such a situation, it is assumed that Ω is a finite union of cubes with edge-length ϵ . Thereto, let Y be a unit cell of dimension d with volume 1 – for simplicity it is assumed that $Y = (0, 1)^d$ holds – and let W_Ω be the unique subset of \mathbb{Z}^d that satisfies

$$\Omega = \cup_{w \in W_\Omega} \{\epsilon(w + Y)\}. \quad (5.91)$$

Let n_Ω denote the outer-normal to Γ_Ω . The unit cube Y is subdivided into two regions, the grain \mathcal{G} , located in the center of Y , and the pore-space \mathcal{P} . The grain-boundary $\Gamma_\mathcal{G}$ separates \mathcal{G} and \mathcal{P} and ∂Y is the outer boundary of Y , that is

$$Y = \mathcal{G} \cup \Gamma_\mathcal{G} \cup \mathcal{P}. \quad (5.92)$$

Let $n_\mathcal{G}$ be the normal to $\Gamma_\mathcal{G}$ that points into the grain. The total pore-space \mathcal{P}^ϵ of the porous medium is given by

$$\mathcal{P}^\epsilon = \cup_{w \in W_\Omega} \{\epsilon(w + \mathcal{P})\}. \quad (5.93)$$

Its outer-boundary coincides with the boundary Γ_Ω of Ω , whereas its inner-boundaries coincide with the total grain surface, that is

$$\Gamma_{\mathcal{P}^\epsilon} = \Gamma_\Omega \cup (\cup_{w \in W_\Omega} \{\epsilon(w + \Gamma_\mathcal{G})\}). \quad (5.94)$$

Let $n_{\mathcal{P}^\epsilon}$ denote the outer normal to $\Gamma_{\mathcal{P}^\epsilon}$.

5.3.2 The sequence of problems with varying scale ϵ

Define

$$G_{\epsilon,i}(\Phi, u) = \left(\sum_{j \in I \setminus \{i\}} (\partial_{\phi_i} - \partial_{\phi_j}) W(\Phi) \right) + \epsilon f_i(\Phi, u) \text{ for } i \in I. \quad (5.95)$$

The scaling of f_i is explained below.

The following problem on scale $\epsilon > 0$ is a slight modification of the Problem 5.8.

Problem 5.13. *Given the fixed scale $\epsilon > 0$, the parameters $\alpha, \xi, D, \delta, \rho > 0$, the functions $G_{\epsilon,i}(\Phi, u)$ defined by (5.95), the potential $W(\Phi)$ defined by (5.9), the driving forces $f_i(\Phi, u)$ defined by (5.16) and (5.19), the interpolation-function $g_\delta(\Phi)$ defined by (5.27), and the periodic initial conditions $\Phi_{\epsilon,0} = (\phi_{\epsilon,1,0}, \phi_{\epsilon,2,0}, \phi_{\epsilon,3,0}) : \mathcal{P}^\epsilon \rightarrow \mathcal{S}$ and $u_{\epsilon,0} : \mathcal{P}^\epsilon \rightarrow \mathbb{R}$, find the phase-fields $\Phi_\epsilon = (\phi_{1,\epsilon}, \phi_{2,\epsilon}, \phi_{3,\epsilon})$ and the concentration u_ϵ satisfying*

$$\begin{aligned} \alpha \xi^2 \partial_t \phi_{i,\epsilon} - \frac{3}{4} \xi^2 \Delta \phi_{i,\epsilon} + G_{\epsilon,i}(\Phi_\epsilon, u_\epsilon) &= 0 && \text{in } J(T) \times \mathcal{P}^\epsilon, \\ \partial_t((\phi_{1,\epsilon} + \delta)u_\epsilon) - D \nabla \cdot ((\phi_{1,\epsilon} + \delta) \nabla u_\epsilon) - \rho g_\delta(\Phi_\epsilon) \partial_t \phi_{1,\epsilon} &= 0 && \text{in } J(T) \times \mathcal{P}^\epsilon, \\ - \frac{3}{4} \xi^2 \nabla \phi_{i,\epsilon} \cdot n_{\mathcal{P}^\epsilon} &= 0 && \text{on } J(T) \times \Gamma_{\mathcal{P}^\epsilon}, \\ - D(\phi_{1,\epsilon} + \delta) \nabla u_\epsilon \cdot n_{\mathcal{P}^\epsilon} &= 0 && \text{on } J(T) \times \Gamma_{\mathcal{P}^\epsilon}, \\ \Phi_\epsilon(0, x) &= \Phi_{\epsilon,0}(x) && \text{in } \mathcal{P}^\epsilon, \\ u_\epsilon(0, x) &= u_{\epsilon,0}(x) && \text{in } \mathcal{P}^\epsilon. \end{aligned} \quad (5.96)$$

Let $C_\#^0(Y)$ denote the set that contains all periodic continuous functions in \mathbb{R}^d with periodicity cell Y . The periodicity of the initial data is generated by the conditions

$$\phi_{\epsilon,i,0}(x) = \phi_{0,i,0}(x, \frac{x}{\epsilon}) \text{ for } i \in I \text{ and } u_{\epsilon,0}(x) = u_{0,0}(x, \frac{x}{\epsilon}) \quad (5.97)$$

with functions $\phi_{0,i,0}, u_{0,0} \in L_2(\mathcal{P}^\epsilon; C_\#^0(Y))$.

In order to obtain a suitable asymptotic limit problem for $\epsilon \rightarrow 0$, it is fundamental to scale certain parameters in dependence of ϵ . Let

$$\xi = \epsilon \xi_0 \text{ and } \alpha = \epsilon^{-2} \alpha_0 \text{ with } \xi_0, \alpha_0 > 0. \quad (5.98)$$

Since the volume of a grain is proportional to ϵ^d , the volume of a surrounding solid phase is proportional to ϵ^d . Consequently, the width ξ of the diffuse interface regions must be proportional to ϵ . The relaxation parameter α is scaled such that the product $\alpha \xi^2$ remains constant. Recalling (5.16), (5.19) and (5.95), the functions $f_1(\Phi_\epsilon, u_\epsilon)$ and $f_3(\Phi_\epsilon, u_\epsilon)$ appearing in the first equation of (5.96) are scaled by ϵ such that

$$\epsilon f_1(\Phi_\epsilon, u_\epsilon) = -\epsilon f_3(\Phi_\epsilon, u_\epsilon) = \epsilon \alpha \xi \gamma_{13}(\Phi_\epsilon) f(u_\epsilon) = \alpha_0 \xi_0 \gamma_{13}(\Phi_\epsilon) f(u_\epsilon). \quad (5.99)$$

The function $f_2(\Phi_\epsilon, u_\epsilon) = 0$. The regularized interpolation-function $g_\delta(\Phi)$ substituted $g_0(\Phi)$ in the second equation of (5.96) such that Taylor expansions of the interpolation-function exist.

5.3.3 The formal asymptotic expansions

Let $(\Phi_\epsilon, u_\epsilon) = (\phi_{1,\epsilon}, \phi_{2,\epsilon}, \phi_{3,\epsilon}, u_\epsilon)$ be the unique solution to the Problem 5.13 of scale ϵ . In order to study the limit $\epsilon \rightarrow 0$, the existence of asymptotic expansions

$$\begin{aligned} \phi_{i,\epsilon}(t, x) &= \sum_{j=0}^{\infty} \epsilon^j \phi_{i,j}(t, x, \frac{x}{\epsilon}) \text{ for } i \in I, \\ u_\epsilon(t, x) &= \sum_{j=0}^{\infty} \epsilon^j u_j(t, x, \frac{x}{\epsilon}), \end{aligned} \quad (5.100)$$

of the solution is assumed. Please note that the existence of such an expansion is not guaranteed. It is a part of future research to justify the assumption.

Employing the asymptotic expansions, Taylor expansions with the expansion point $(\phi_{1,0}, \phi_{2,0}, \phi_{3,0}, u_0)$ for the functions depending on the solution $(\phi_{1,\epsilon}, \phi_{2,\epsilon}, \phi_{3,\epsilon}, u_\epsilon)$, as well as the formal relation

$$\nabla v \left(x, \frac{x}{\epsilon} \right) = \nabla_x v \left(x, \frac{x}{\epsilon} \right) + \frac{1}{\epsilon} \nabla_y v \left(x, \frac{x}{\epsilon} \right), \quad (5.101)$$

where $\nabla_x v$ and $\nabla_y v$ denote the gradients with respect to the first and the second variable of a function $v = v(x, y)$, into (5.96) on the scale ϵ , comparing the coefficients of different powers of ϵ and letting the scale parameter ϵ tend to 0, results in the following problems on the different scales.

5.3.3.1 The ϵ^{-2} -problem and the ϵ^{-1} -condition on the boundary

The $\mathcal{O}(\epsilon^{-2})$ -terms in the evolution equations and the $\mathcal{O}(\epsilon^{-1})$ -terms in the boundary conditions of (5.96) give

$$\begin{aligned} -D\nabla_y \cdot ((\phi_{1,0} + \delta)\nabla_y u_0) &= 0 \text{ in } J(T) \times \Omega \times \mathcal{P}, \\ -D(\phi_{1,0} + \delta)\nabla_y u_0 \cdot n_G &= 0 \text{ on } J(T) \times \Omega \times \Gamma_G, \end{aligned} \quad (5.102)$$

where u_0 is Y -periodic with respect to y . This implies that the solution $u_0 = u_0(t, x)$ is independent of y .

5.3.3.2 The ϵ^{-1} -problem and the ϵ^0 -condition on the boundary

Since $u_0 = u_0(t, x)$, the $\mathcal{O}(\epsilon^{-1})$ -terms in the evolution equations and the $\mathcal{O}(\epsilon^0)$ -terms in the boundary conditions of (5.96) give

$$\begin{aligned} -D\nabla_y \cdot ((\phi_{1,0} + \delta)\nabla_y u_1) &= D\nabla_y(\phi_{1,0} + \delta) \cdot \nabla_x u_0 \text{ in } J(T) \times \Omega \times \mathcal{P}, \\ -D(\phi_{1,0} + \delta)\nabla_y u_1 \cdot n_G &= D(\phi_{1,0} + \delta)\nabla_x u_0 \cdot n_G \text{ on } J(T) \times \Omega \times \Gamma_G, \end{aligned} \quad (5.103)$$

where u_1 is Y -periodic with respect to y . Because of the linear structure of the problem, the solution u_1 can be expressed in terms of $\partial_{x_j} u_0$, that is

$$u_1(t, x, y) = \tilde{u}_1(t, x) + \sum_{j=1}^d w_j(t, x, y) \partial_{x_j} u_0(t, x), \quad (5.104)$$

with an arbitrary function $\tilde{u}_1(t, x)$ which plays no role in the final form of the limit problem, and with the unique solutions w_j of the cell problems (for $j = 1, \dots, d$)

$$\begin{aligned} -D\nabla_y \cdot ((\phi_{1,0} + \delta)\nabla_y w_j) &= D\nabla_y(\phi_{1,0} + \delta) \cdot e_j \text{ in } J(T) \times \Omega \times \mathcal{P}, \\ -D(\phi_{1,0} + \delta)\nabla_y w_j \cdot n_G &= D(\phi_{1,0} + \delta)e_j \cdot n_G \text{ on } J(T) \times \Omega \times \Gamma_G, \end{aligned} \quad (5.105)$$

where w_j is Y -periodic with respect to y and its average in \mathcal{P} vanishes, and e_j is the j -th unit vector of \mathbb{R}^d .

5.3.3.3 The ϵ^0 -problem and the ϵ^1 -condition on the boundary

The $\mathcal{O}(\epsilon^0)$ -terms in the evolution equations and the $\mathcal{O}(\epsilon^1)$ -terms in the boundary conditions of (5.96) give

$$\begin{aligned} & \alpha_0 \xi_0^2 \partial_t \phi_{i,0} - \frac{3}{4} \xi_0^2 \Delta_y \phi_{i,0} + \left(\sum_{j \in I \setminus \{i\}} (\partial_{\phi_i} - \partial_{\phi_j}) W(\Phi_0) \right) \\ & = -\tilde{f}_i(\Phi_0, u_0) = - \begin{cases} \alpha_0 \xi_0 \gamma_{13}(\Phi_0) f(u_0) & \text{if } i = 1, \\ 0 & \text{if } i = 2, \\ -\alpha_0 \xi_0 \gamma_{13}(\Phi_0) f(u_0) & \text{if } i = 3, \end{cases} \quad \text{in } J(T) \times \Omega \times \mathcal{P}, \end{aligned} \quad (5.106)$$

$$\begin{aligned} & \partial_t((\phi_{1,0} + \delta)u_0) - \rho g_\delta(\Phi_0) \partial_t \phi_{1,0} - \\ & - D \nabla_x \cdot ((\phi_{1,0} + \delta)(\nabla_x u_0 + \nabla_y u_1)) - D \nabla_y \cdot \mathcal{A} = 0 \quad \text{in } J(T) \times \Omega \times \mathcal{P}, \\ & - \frac{3}{4} \xi_0^2 \nabla_y \phi_{i,0} \cdot n_G = 0 \quad \text{on } J(T) \times \Omega \times \Gamma_G, \\ & - D \mathcal{A} \cdot n_G = 0 \quad \text{on } J(T) \times \Omega \times \Gamma_G, \end{aligned}$$

where

$$\mathcal{A} = (\phi_{1,0} + \delta)(\nabla_x u_1 + \nabla_y u_2) + \phi_{1,1}(\nabla_x u_0 + \nabla_y u_1), \quad (5.107)$$

and where $\phi_{i,0}$ and u_2 are Y -periodic with respect to y . In order to dispose of the term $-D \nabla_y \cdot \mathcal{A}$ in the second evolution equation, the equation is integrated over the domain \mathcal{P} . Since u_0 is independent of y , the periodicity of $\phi_{1,0}$, $\phi_{1,1}$, u_1 and u_2 yields the homogenized equation

$$\partial_t \left(\overline{\phi_{1,0} + \delta}^{\mathcal{P}} u_0 \right) - D \nabla_x \cdot (K(\phi_{1,0} + \delta) \nabla_x u_0) - \overline{\rho g_\delta(\Phi_0) \partial_t \phi_{1,0}}^{\mathcal{P}} = 0 \quad (5.108)$$

in $J(T) \times \Omega$, where for all functions $v : \overline{J(T)} \times \Omega \times \mathcal{P} \rightarrow \mathbb{R}$

$$\overline{v(t, x, \cdot)}^{\mathcal{P}} = \frac{1}{|\mathcal{P}|} \int_{\mathcal{P}} v(t, x, y) dy \quad (5.109)$$

and

$$(K(v(t, x, \cdot)))_{ij} := \frac{1}{|\mathcal{P}|} \int_{\mathcal{P}} v(t, x, y) (\delta_{ij} + \partial_y w_j(t, x, y)) dy \quad \text{for } 1 \leq i, j \leq d. \quad (5.110)$$

Remark 5.14. In [32] it is proven that the effective diffusion tensor $K(\phi_{1,0} + \delta)$ is symmetric, elliptic and bounded.

5.3.4 The two-scale model

The limit problem is a two-scale one, which is used as approximation of the pore-scale Problem 5.8 for situations with small but non-vanishing scale parameter ϵ . It bridges the gap between the pore-scale and the scale of the diffusion process. For ease of the presentation the subscript 0 referring to the scale ϵ^0 is omitted in the following. The two-scale model consists of a macroscopic homogenized equation that describes the evolution of the macroscopic concentration $u = u(t, x)$ of the dissolved particles in the fluid P_1 , and at each point of the macroscopic domain of microscopic cell problems with periodic boundary conditions that describe the evolution of the microscopic phase-fields $\Phi = \Phi(t, x, y)$. The

variables on the two scales are coupled: the macroscopic equation depends on averaged values of the solution of the local cell problems and, vice versa, the macroscopic concentration appears in the driving forces of the phase-field equations in the local cell problems. What is important to note is that the microscopic problems in different macroscopic nodes do not influence each other directly. Therefore, they can be computed in parallel.

The macroscopic problem and the family of microscopic cell problems have the following formulation.

Problem 5.15. *Given the parameters $\alpha, \xi, D, \delta, \rho > 0$, the functions $G_i(\Phi, u)$ defined by (5.20), the potential $W(\Phi)$ defined by (5.9), the driving forces $f_i(\Phi, u)$ defined by (5.16) and (5.19), the interpolation-function $g_\delta(\Phi)$ defined by (5.27), the averaging $\overline{u}^{\mathcal{P}}$ of functions $u : J(T) \times \Omega \times \mathcal{P} \rightarrow \mathbb{R}$ defined by (5.109), the effective diffusion coefficient $K(\phi_1 + \delta)$ defined by (5.110), and the initial conditions $\Phi_0 = (\phi_{1,0}, \phi_{2,0}, \phi_{3,0}) : \Omega \times \mathcal{P} \rightarrow \mathcal{S}$ and $u_0 : \Omega \rightarrow \mathbb{R}$. Find the macroscopic concentration u satisfying*

$$\begin{aligned} \partial_t \left(\overline{\phi_1 + \delta}^{\mathcal{P}} u \right) - D \nabla_x \cdot (K(\phi_1 + \delta) \nabla_x u) - \overline{\rho g_\delta(\Phi) \partial_t \phi_1}^{\mathcal{P}} &= 0 \text{ in } J(T) \times \Omega, \\ - D K(\phi_1 + \delta) \nabla_x u \cdot n_\Omega &= 0 \text{ on } J(T) \times \Gamma_\Omega. \\ u(0, x) &= u_0(x) \text{ in } \Omega. \end{aligned} \quad (5.111)$$

For every $x \in \Omega$ find the Y -periodic microscopic phase-fields Φ satisfying for $i \in I$

$$\begin{aligned} \alpha \xi^2 \partial_t \phi_i - \frac{3}{4} \xi^2 \Delta_y \phi_i + G_i(\Phi, u) &= 0 \text{ in } J(T) \times \mathcal{P}, \\ - \frac{3}{4} \xi^2 \nabla_y \phi_i \cdot n_{\mathcal{G}} &= 0 \text{ on } J(T) \times \Gamma_{\mathcal{G}}. \end{aligned} \quad (5.112)$$

For every $x \in \Omega$ and for $j = 1, \dots, d$ find the Y -periodic microscopic solution w_j with vanishing average in the pore-space \mathcal{P} satisfying

$$\begin{aligned} - D \nabla_y \cdot ((\phi_1 + \delta) \nabla_y w_j) &= D \nabla_y \phi_1 \cdot e_j \text{ in } J(T) \times \mathcal{P}, \\ - D(\phi_1 + \delta) \nabla_y w_j \cdot n_{\mathcal{G}} &= D(\phi_1 + \delta) e_j \cdot n_{\mathcal{G}} \text{ on } J(T) \times \Gamma_{\mathcal{G}}. \end{aligned} \quad (5.113)$$

5.3.5 An adaptive discretization of the two-scale problem 5.15

Problem 5.15 is discretized explicitly in time. The spatial derivatives are discretized by standard second-order finite differences on uniform rectangular grids Ω_{h_g} and Y_{h_ℓ} , where $h_g > 0$ denotes the macroscopic and $h_\ell > 0$ the microscopic space-increment. The discrete pore-space \mathcal{P}_{h_ℓ} as well as the physical and numerical constants are specified in the Section 5.4 presenting the results of numerical computations. The time-increment Δt must, owing to the CFL-condition and the multiplier of u in (5.111), satisfy

$$\Delta^n t \leq c(D) \left(\delta + \min_{x \in \Omega_{h_g}} \overline{\phi_1(t_{n-1}, x)}^{\mathcal{P}_{h_\ell}} \right) h_g^2, \quad (5.114)$$

where t_n denotes the discrete time in step n and the constant $c(D) > 0$ depends on the diffusion coefficient D . The Figure 5.4 illustrates the macro-micro configuration.

It is demanding to compute the microscopic parameters for the macroscopic problem in every grid point of the macroscopic domain. The solution of a microscopic problem depends continuously on the evolution of the macroscopic concentration. Exploiting this property, the two-scale model is solved adaptively in the sense of the strategy of Section

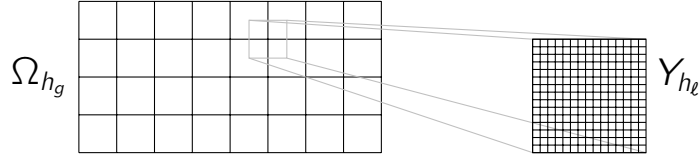


Figure 5.4: The macroscopic Ω_{h_g} and the local microscopic grid Y_{h_l} .

3. A metric d_E measures the distance of two concentration evolutions $u(\cdot, x)$ and $u(\cdot, \tilde{x})$ on the time-interval $\overline{J(T)}$ in two macroscopic nodes $x, \tilde{x} \in \Omega_{h_g}$,

$$d_E(u(\cdot, x), u(\cdot, \tilde{x}); t, \lambda) := \int_0^t e^{-\lambda(t-s)} |u(s, x) - u(s, \tilde{x})| ds, \quad (5.115)$$

where $\lambda \geq 0$ is a parameter. A microscopic problem is solved for active macroscopic nodes only, the microscopic data of inactive macroscopic nodes is interpolated between the microscopic data of active nodes. Initially, the set of active nodes contains only one macroscopic node. It is updated in course of the simulation. That is, it is refined if necessary, that is if the minimal d_E -distance between an inactive and all active nodes exceeds an upper bound. Vice versa, it is coarsened if possible, that is if the d_E -distance between two active nodes falls below a lower limit. The interested reader is referred to Section 3 for more details on the strategy.

The following algorithm solves the adaptive discrete problem.

1. Set $n = n + 1$ and $t_n = t_{n-1} + \Delta^n t$.
2. Adjust the set A^n of the active macroscopic nodes.
3. For every node in A^n solve (5.112) for ϕ_2^n and ϕ_3^n and set $\phi_1^n = 1 - \phi_2^n - \phi_3^n$.
4. For every node in A^n solve (5.113) for w_1^n and w_2^n .
5. Approximate the microscopic parameters $\overline{\phi_1 + \delta}^P$, $K(\phi_1 + \delta)$ and $\overline{g_\delta(\Phi) \partial_t \phi_1}^P$ in Ω_{h_g} .
6. Solve the macroscopic problem (5.111) for u^n .
7. Restart if $t_n < T$.

Fundamental to the adaptive strategy is that the initial conditions of the microscopic problems are at least very similar. Therefore, as it is in some of the settings considered in the Section 5.4, if these initial conditions differ, then the set of macroscopic nodes must be subdivided into subsets with respect to these initial conditions. That is, for M initial conditions of the microscopic problems M subsets $\Omega_{h_g}^{(m)}$, $m = 1, \dots, M$, of macroscopic nodes Ω_{h_g} are constructed. For each of the subsets one adaptive solution strategy is applied for.

For completeness, the parameters of the adaptive strategy are specified as follows, see Section 3: $\lambda = 0.1$, $c_{\text{tol}_c} = 0.2$, $c_{\text{tol}_e} = 0.01$, $\text{RU} = 0$, $eC = 1$, $M_A = 2$, IT-CA, the initial set of active nodes contains one node of every subset $\Omega_{h_g}^{(m)}$, the Copy Method, and the refining tolerance is defined as

$$\text{tol}_r(t) := c_{\text{tol}_r} \max_{m=1, \dots, M} \max_{x, \tilde{x} \in \Omega_{h_g}^{(m)}} \{d_E(u(\cdot, x), u(\cdot, \tilde{x}); t, \lambda)\}, \quad (5.116)$$

where $c_{\text{tol}_r} = 10^{-3/2}$ if not stated otherwise.

5.4 Numerical results

This section presents numerical solutions of the two-scale Problem 5.15 in two spatial dimensions. To begin with, it presents results that document that the free energy $U(\Phi)$

test	T	H_{g_1}	H_{g_2}	u_0	D	G	H_ℓ	M	$r_{0,1}$	$\phi_{2,0,0}$	c_{u_0}
E	15.5						200	2	20	1	0
A	10.5	8	8	0.3	$5e+2$	0.1	100	2	10	1	100
S_1	15.5	50	25	0.5	$2e+4$	0.5	200	1	20	0	100
S_2				0.5				1		1	
S_3				0.5				2		1	
S_3				0.3				2		1	

Table 5.1: The varying parameters of the different tests. The test E refers to the test that examines the evolution of the free energy $U(\Phi)$. Since only the microscopic problems are regarded in E , the macroscopic parameters are not specified. The test A refers to the tests demonstrating the accuracy of the adaptive strategy's results. The four tests S_1 , S_2 , S_3 and S_4 differ from each other only in the parameters that are specified for all of them.

in the microscopic pore-space decreases monotonically if the driving forces vanish. Next it demonstrates the accuracy of the adaptive strategy's results. Finally, it presents the results of four tests S_1, \dots, S_4 that expose the interdependence of the change of the pore structure and of the evolution of the macroscopic concentration of the dissolved particles in P_1 .

Table 5.1 specifies the varying parameters of the different test settings E , A , S_1 , S_2 , S_3 and S_4 . The test E refers to the test that examines the evolution of the free energy $U(\Phi)$, and A refers to the tests demonstrating the accuracy of the adaptive strategy's results. The discrete time-interval $J_{\Delta^nt}(T)$ ranges from 0 to T , where the time-increment $\Delta^nt = 0.001(\delta + \min_{x \in \Omega_{h_g}} \overline{\phi_1(t_{n-1}, x)^{\mathcal{P}_{h_\ell}}})$ is time-dependent. The microscopic domain Y_{h_ℓ} is perforated by a small spherical grain \mathcal{G}_{h_ℓ} of radius h_ℓ , where $h_\ell = 0.1$ defines the microscopic space-increment h_ℓ . Let H_ℓ denote the number of the microscopic nodes in both space dimensions. Then, the microscopic domain Y_{h_ℓ} and the pore-space \mathcal{P}_{h_ℓ} are given by

$$Y_{h_\ell} = \{y_{h_\ell} = (k_1 h_\ell, k_2 h_\ell) \mid k_1, k_2 \in \{0, 1, \dots, H_\ell\}\}, \quad \mathcal{P}_{h_\ell} = Y_{h_\ell} \setminus \mathcal{G}_{h_\ell}. \quad (5.117)$$

The grain is located in the center of Y_{h_ℓ} , that is

$$\mathcal{G}_{h_\ell} = \{y_{h_\ell} \in Y_{h_\ell} \mid \|y_{h_\ell} - 2^{-1}H_\ell\|_2 < h_\ell\}, \quad (5.118)$$

where $\|\cdot\|_2$ denotes the Euclidean norm. Therefore, the pore-space \mathcal{P}_{h_ℓ} consists of $H_\ell^2 - 1$ nodes, due to the periodic boundary conditions. The edge-length $h_g = H_\ell h_\ell$ of Y_{h_ℓ} defines the macroscopic space-increment h_g . The macroscopic domain Ω_{h_g} ,

$$\Omega_{h_g} = \{x_{h_g} = (k_1 h_g, k_2 h_g) \mid k_1 \in \{0, 1, \dots, H_{g,1}\}, k_2 \in \{0, 1, \dots, H_{g,2}\}\} \quad (5.119)$$

consists of $(H_{g,1} + 1)(H_{g,2} + 1)$ nodes. On the macroscopic scale, the initial condition u_0 of the concentration is constant, the diffusion coefficient D is constant and the following Neumann-boundary condition on $J_{\Delta^nt}(T) \times \partial\Omega_{h_g}$ is prescribed,

$$D K(\phi_1 + \delta) \nabla_x u \cdot n_{\Omega_{h_g}} = \begin{cases} G & \text{if } x_1 = H_{g,1} h_g, \\ \frac{G}{2} & \text{if } x_2 = H_{g,2} h_g, \\ 0 & \text{elsewhere,} \end{cases} \quad (5.120)$$

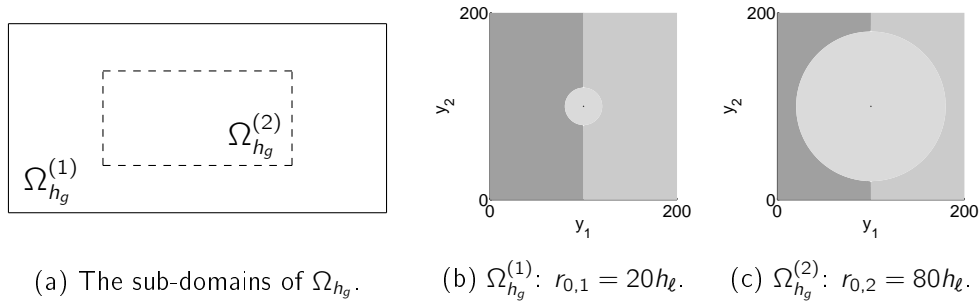


Figure 5.5: The initial phase configurations for the parameters $M = 2$ and $\phi_{2,0,0} = 1$ in the microscopic pore-space \mathcal{P}_{h_ℓ} in the two sub-domains $\Omega_{h_g}^{(1)}$ and $\Omega_{h_g}^{(2)}$ of the macroscopic domain Ω_{h_g} . The black points in the very center of \mathcal{P}_{h_ℓ} in (b) and (c) represent the small spherical grains \mathcal{G}_{h_ℓ} . Each grain is surrounded by a solid P_3 (light-gray). To a solid's left is a fluid P_1 (dark-gray) and to its right a fluids P_2 . The radii $r_{0,m}$ of the initial solids are constant in both sub-domains $\Omega_{h_g}^{(m)}$ for $m = 1, 2$. They are related to each other via $r_{0,2} = 4r_{0,1}$. The colored phase domains P_i are separated by the boundaries $\phi_i = \frac{1}{2}$ for $i \in I$.

where $G > 0$ is constant and $n_{\Omega_{h_g}}$ is the outer-normal to $\partial\Omega_{h_g}$. Therefore, across two parts of the boundary dissolved particles are transported into Ω_{h_g} . The remaining two parts are isolated. The regularization parameter satisfies $\delta = 1e-4$. The microscopic physical parameters are specified as follows: the time relaxation coefficient $\alpha = 100$, the to the width of the phase-transition regions proportional parameter $\xi = 0.25$, and the concentration ρ of particles in the solid P_3 satisfies constantly $\rho = 1$. The parameters of the rate-function f , defined in (5.5), appearing in G_i in the first evolution equation of the Problem 5.15, satisfy $c_{u,1} = 0.5$ defining the threshold and the slope c_{u_0} is constant.

What remains to be specified is the initial configuration of the phase-fields. The grain is surrounded by a spherical solid P_3 . If the parameter $\phi_{2,0,0} = 0$ then the non-solid pore-space is completely occupied by the fluid P_1 . Contrarily, if $\phi_{2,0,0} = 1$ then only the left part of the non-solid pore-space is occupied by the fluid P_1 and the right one by the fluid P_2 . If the parameter $M = 1$, then all solids have the same initial radius $r_{0,1}$. Contrarily, if $M = 2$, then the domain Ω_{h_g} is subdivided into the two sub-domains $\Omega_{h_g}^{(1)} = \Omega_{h_g} \setminus \Omega_{h_g}^{(2)}$ and $\Omega_{h_g}^{(2)}$, where

$$\Omega_{h_g}^{(2)} = \left\{ x_{h_g} \in \Omega_{h_g} \mid x_{h_g} \in \left[\left\lfloor \frac{H_{g,1}}{4} \right\rfloor h_g, 3 \left\lfloor \frac{H_{g,1}}{4} \right\rfloor h_g \right] \times \left[\left\lfloor \frac{H_{g,2}}{4} \right\rfloor h_g, 3 \left\lfloor \frac{H_{g,2}}{4} \right\rfloor h_g \right] \right\}, \quad (5.121)$$

with the floor function $x \mapsto \lfloor x \rfloor = \max\{k \in \mathbb{Z} \mid k \leq x\}$. If $M = 2$ then the solids in $\Omega_{h_g}^{(1)}$ are initially of radius $r_{0,1}$, and in $\Omega_{h_g}^{(2)}$ they are initially of radius $r_{0,2} = 4r_{0,1}$. The initial configuration for $M = 2$ and $\phi_{2,0,0} = 1$ is illustrated in Figure 5.5. Please note, that if $\phi_{2,0,0} = 0$ then the fluid P_2 does not emerge out of nothing, that is if $\phi_{2,0,0} = 0$ then $\phi_2 \equiv 0$ in $J_{\Delta t}^n(T) \times \Omega_{h_g} \times \mathcal{P}_{h_\ell}$. The phase-fields are initialized by $\Phi_0 = (\phi_{1,0}, \phi_{2,0}, \phi_{3,0})$, which is in accordance with the equation (5.77).

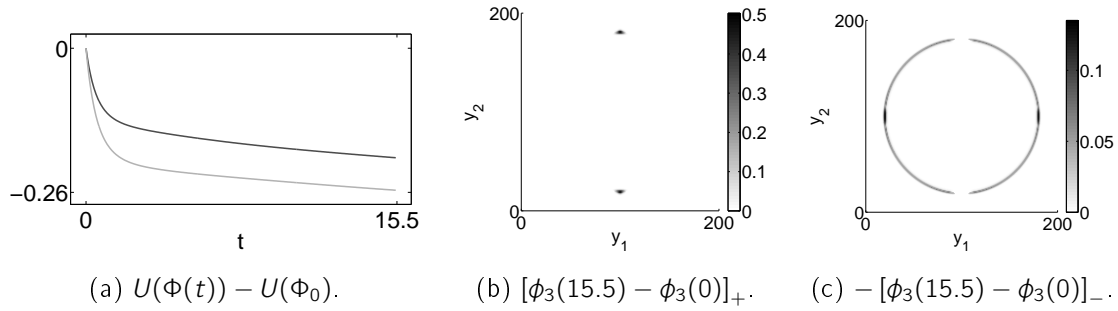


Figure 5.6: Results of test E with vanishing driving forces on the time-interval $J_{\Delta^n t}(15.5)$. Figure (a) depicts the evolution of the free energy difference $U(\Phi(t)) - U(\Phi_0)$ in dark-gray (resp. light-gray) for the microscopic problems in the sub-domain $\Omega_{h_g}^{(1)}$ (resp. $\Omega_{h_g}^{(2)}$) of the macroscopic domain Ω_{h_g} . The initial free energy satisfies $U(\Phi_0) = 11.36$ everywhere in $\Omega_{h_g}^{(1)}$ and $U(\Phi_0) = 17.48$ in $\Omega_{h_g}^{(2)}$. The Figures (b) and (c) depict the positive and the negative portion of the difference $\phi_3(15.5) - \phi_3(0)$ for the microscopic problems in $\Omega_{h_g}^{(2)}$, where $[\cdot]_+ : x \mapsto [x]_+ = \max(0, x)$ and $[\cdot]_- : x \mapsto [x]_- = \min(0, x)$.

5.4.1 Test E : the evolution of the free energy

Figure 5.6a illustrates for test E the evolution of the free energy $U(\Phi)$, defined in (5.8), for the microscopic problems in the two sub-domains $\Omega_{h_g}^{(1)}$ and $\Omega_{h_g}^{(2)}$. The driving forces are constantly equal to zero, since $c_{u,0} = 0$ (see (5.5)). In both sub-domains the free energy decreases monotonically in $J_{\Delta^n t}(15.5)$. Their rapid decreases in the beginning are the result of presumably slightly non-compatible initial conditions Φ_0 ; non-compatible in the sense that the initial phase transition regions differ slightly from the regions that result from the evolution equations. However, the monotonous decrease matches the expectation of a dissipative free energy that was raised by Theorem 5.11. The Figures 5.6b and 5.6c show that the initial spherical phase P_3 converges to its equilibrium state, that is towards a lense between the two fluids. Because the surface tensions σ of the three phases are equal, the three interfaces meet at an angle of 120° in equilibrium according to Young's law and according to the results presented in Section 5.2.3.

5.4.2 Test A : the quality of the adaptive strategy

The results of test A presented in Figure 5.7 show that the adaptive solution converges to the non-adaptive solution for the refining tolerance parameter c_{tol_r} of (5.116) tending to zero. The parameters of test A are similar to the parameters of test S_4 . However, since the microscopic problem of every macroscopic node has to be solved for the non-adaptive solution, test A solves the Problem 5.15 in a much smaller time-space cylinder than S_4 . Since, the adaptive result converges rapidly to the non-adaptive result, and since $c_{\text{tol}_r} = 10^{-3/2}$ for the tests S_1, \dots, S_4 , the results of S_1, \dots, S_4 are trustworthy.

Moreover, these results show that it is indeed not efficient to compute the microscopic parameters for the macroscopic problem in every macroscopic node.

Without going further into details here, Figure 5.11d depicts the distribution of the adaptive strategy's active macroscopic nodes in the macroscopic domain Ω_{h_g} .

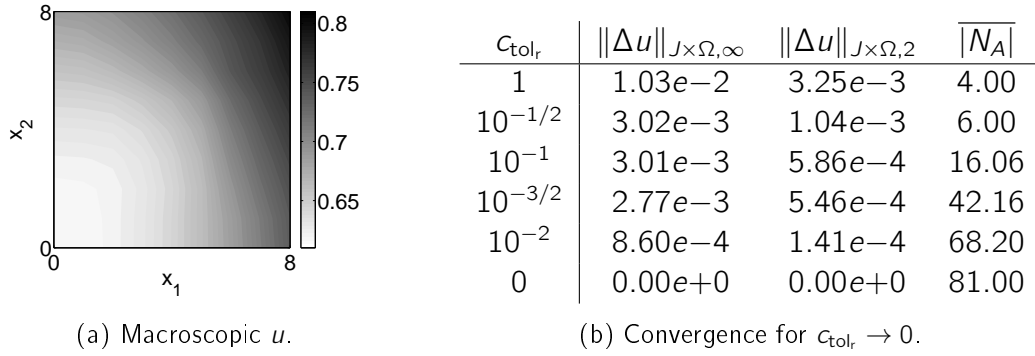


Figure 5.7: Convergence of the adaptive solution to the non-adaptive solution of test A for the parameter c_{tol_r} of the refining tolerance (5.116) tending to zero. The Figure (a) depicts the macroscopic concentration of the non-adaptive solution in the end of the time-interval $J_{\Delta^n t}(10.5)$. The table's first column denotes the parameter c_{tol_r} . The second resp. the third column present the L_∞ - resp. L_2 -norm of the difference Δu of the adaptive and the non-adaptive macroscopic concentration solution in the discrete time-space cylinder $J_{\Delta^n t}(10.5) \times \Omega_{h_g}$. In addition, the fourth column presents the average number $\overline{N_A}$ of active nodes in $J_{\Delta^n t}(10.5)$.

5.4.3 The tests S_1 , S_2 , S_3 and S_4

The tests S_1 , S_2 , S_3 and S_4 solve the two-scale Problem 5.15 on a large time-space cylinder $J_{\Delta^n t}(15.5) \times \Omega_{h_g} \times \mathcal{P}_{h_\ell}$. The macroscopic domain $\Omega_{h_g} = [0, 49h_g] \times [0, 24h_g]$ consists of 1,250 nodes, each of them governs one microscopic problem in \mathcal{P}_{h_ℓ} consisting of 40,000 nodes. Consequently, the product $\Omega_{h_g} \times \mathcal{P}_{h_\ell}$ consists of $5e+7$ nodes. Since it is very demanding to solve these tests non-adaptively, the adaptive strategy is applied with $c_{\text{tol}_r} = 10^{-3/2}$.

The tests differ in the following parameters: in the initial constant macroscopic concentration u_0 of the dissolved particles in the initial fluid P_1 ; in the parameter M , that is in the condition whether the macroscopic domain is subdivided into two sub-domains $\Omega_{h_g}^{(1)}$ and $\Omega_{h_g}^{(2)}$ due to two initial radii of the initial solids in the microscopic problems; and in the parameter $\phi_{2,0,0}$, that is in the condition whether the fluid P_2 exists. The initial volume fraction $\overline{\phi_{3,0}^{\mathcal{P}}}$ of the spherical initial solid P_3 of radius $r_0 = 20h_\ell$ equals 0.0314, and $\overline{\phi_3^{\mathcal{P}}} = 0.5028$ if $r_0 = 80h_\ell$.

5.4.3.1 The test S_1

Figure 5.8 illustrates the results of test S_1 . Since $\phi_{2,0,0} = 0$ the fluid P_2 is not existent at any time at any location. Due to $M = 1$ all initial solids are of radius $r_{0,1} = 20h_\ell$, that is the initial solids' volume fraction of the pore-space volume equals 0.0314. The initial concentration $u_0 = 0.5$ matches the threshold $c_{u,1} = 0.5$ of the rate-function in (5.5). Therefore, the existing phases P_1 and P_3 are almost constant in the very beginning of $J_{\Delta^n t}(15.5)$, because whether precipitation nor dissolution reactions take place.

The concentration u is never smaller than the threshold and never larger than 0.9 in $J_{\Delta^n t}(15.5) \times \Omega_{h_g}$. Due to the transport of particles into Ω_{h_g} across the right and across the upper boundary (5.120), the macroscopic node $(49, 24)^\top$ records all the time the

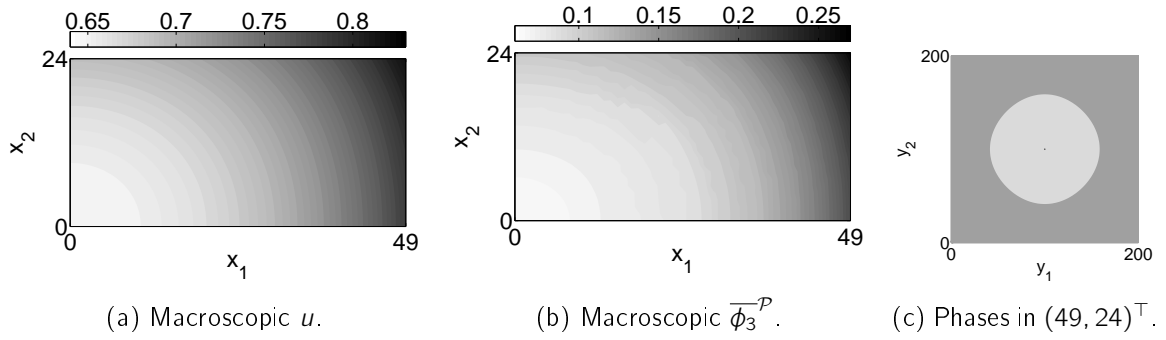


Figure 5.8: Results of test S_1 in the end of the time-interval $J_{\Delta n_t}(15.5)$. The Figure (a) depicts the macroscopic concentration u , (b) displays the macroscopic ratio $\overline{\phi_3^P}$ of the solid's volume in the local pore-space, and (c) illustrates the configuration of the phases in the pore-space in the macroscopic node $(49, 24)^\top$. Since the fluid P_2 is not existent in the beginning and hence at any time, only the fluid P_1 and the solid P_3 show up.

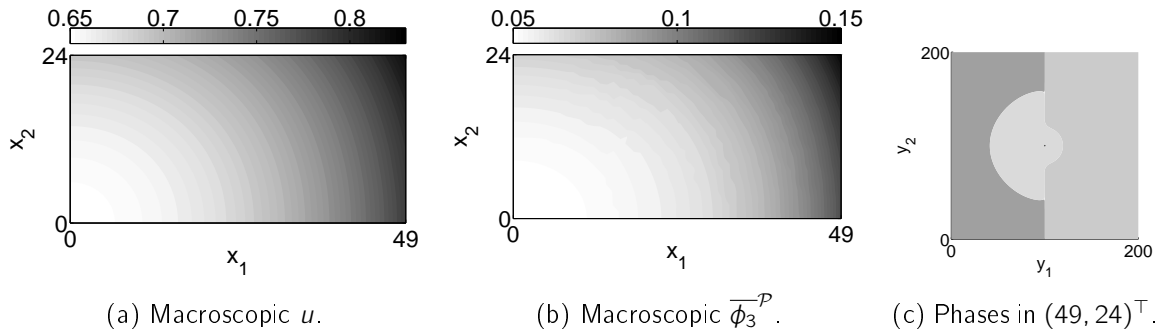


Figure 5.9: Results of test S_2 in the end of $J_{\Delta n_t}(15.5)$.

highest concentration, and $(0, 0)^\top$ the lowest. Consequently, due to the fact that the more dissolved particles in the fluid P_1 precipitate on the solid P_3 the higher the particles concentration u is in P_1 , the microscopic solid region advances most quickly in $(49, 24)^\top$ and most slowly in $(0, 0)^\top$. Since the solids P_3 are completely surrounded by the fluids P_1 , the solids advance uniformly in all spatial directions. In the end of $J_{\Delta n_t}(15.5)$, the volume of the solid in $(49, 24)^\top$ is around eight times as much as the initial solid's volume, whereas the volume of the solid in $(0, 0)^\top$ is only around twice as much. Thus, the macroscopic fields u and $\overline{\phi_3^P}$ increase smoothly and monotonically on Ω_{hg} from the left to the right and from the bottom to the top. The little perturbations in the $\overline{\phi_3^P}$ -field result from the adaptive solution.

5.4.3.2 The test S_2

Figure 5.9 depicts the results of test S_2 . Test S_2 differs from S_1 only in the parameter $\phi_{2,0,0}$: the fluid P_2 is existent in S_2 but not in S_1 . The same qualitative macroscopic results of the concentration u and of the volume fraction $\overline{\phi_3^P}$ hold for the two tests. However, since the fluid P_2 is existent in S_2 , and due to the fact that only the fluid P_1 contains dissolved particles that can precipitate on a solid P_3 , a solid advances as a result of precipitation only in contact with the fluid P_1 .

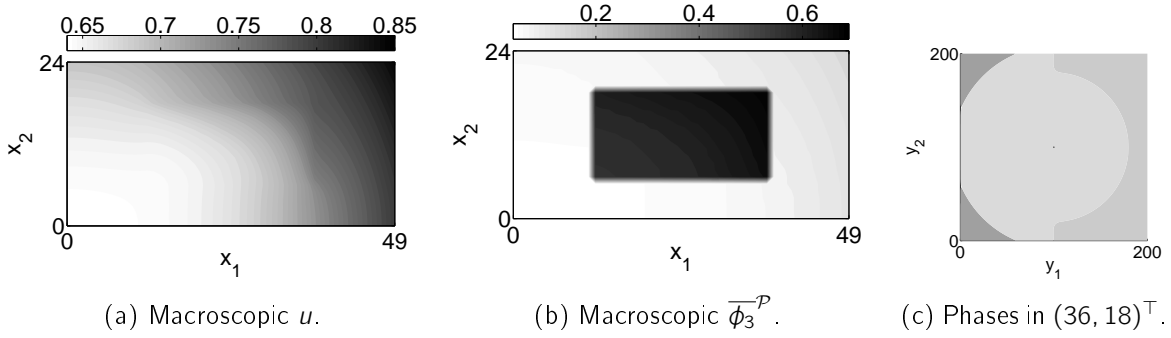


Figure 5.10: Results of test S_3 in the end of $J_{\Delta n_t}(15.5)$.

Besides precipitation, the evolution of a diffuse interface $\Gamma_{13}^d(t)$ is influenced by its mean curvature. Whereas the diffuse interfaces $\Gamma_{12}^d(t)$ and $\Gamma_{23}^d(t)$ evolve exclusively with mean curvature flow. Since the mean curvature of an interface $\Gamma_{12}^d(t)$ is zero, the interfaces $\Gamma_{12}^d(t)$ remain constant. Due to $\alpha = 100$, the surface tensions σ of the three phases are very small, that is $\sigma = \frac{3}{4\alpha} = 0.0075$ according to (5.83). Consequently, the evolution of the diffuse interface $\Gamma_{13}^d(t)$ is dominated by the precipitation process. The diffuse interface $\Gamma_{23}^d(t)$ is almost constant. As a result, the change of the phases P_2 is not worth mentioning.

5.4.3.3 The test S_3

The results of test S_3 are presented in Figure 5.10. Test S_3 differs from S_2 only in the parameter M . That is, in S_3 the macroscopic domain Ω_{h_g} is subdivided into the two sub-domains $\Omega_{h_g}^{(1)} = \Omega_{h_g} \setminus \Omega_{h_g}^{(2)}$ and $\Omega_{h_g}^{(2)}$ as depicted in Figure 5.5, where

$$\Omega_{h_g}^{(2)} = \{x_{h_g} \in \Omega_{h_g} \mid x_{h_g} \in [12h_g, 36h_g] \times [6h_g, 18h_g]\}. \quad (5.122)$$

The initial solid is of small radius $20h_\ell$ in $\Omega_{h_g}^{(1)}$ and of large radius $80h_\ell$ in $\Omega_{h_g}^{(2)}$. Therefore, $\overline{\phi}_{3,0}^{\mathcal{P}} = 0.0314$ in $\Omega_{h_g}^{(1)}$ and $\overline{\phi}_3^{\mathcal{P}} = 0.5028$ in $\Omega_{h_g}^{(2)}$.

Since the initially constant concentration u increases most quickly in the macroscopic node $(49, 24)^\top$, due to the Neumann boundary condition (5.120), the solid region in $(49, 24)^\top$ advances most quickly. Nevertheless, the largest solid is all the time located in $(36, 18)^\top$. Because the volume fraction of the fluid P_1 in $\Omega_{h_g}^{(2)}$ is significantly smaller than in $\Omega_{h_g}^{(1)}$, the diffusion of the concentration u is significantly weaker in $\Omega_{h_g}^{(2)}$ than in $\Omega_{h_g}^{(1)}$. The Figure 5.10a depicts an edge in the concentration field in Ω_{h_g} exactly where the Figure 5.10b depicts an edge in the volume fraction field $\overline{\phi}_3^{\mathcal{P}}$. An edge in $\overline{\phi}_3^{\mathcal{P}}$ corresponds to an edge in the volume fraction field $\overline{\phi}_1^{\mathcal{P}}$ of the fluid P_1 . This is due to

$$\overline{\phi}_1^{\mathcal{P}} = 1 - \overline{\phi}_2^{\mathcal{P}} - \overline{\phi}_3^{\mathcal{P}} \quad (5.123)$$

and $\overline{\phi}_2^{\mathcal{P}}$ is almost constant in $J_{\Delta n_t}(15.5) \times \Omega_{h_g}$. This observation of stronger and weaker diffusion is of importance, because it matches the following real world phenomena. If the pore-space is clogged, clogged in the sense that the volume fraction of the fluid P_1 is very small, then the dissolved particles in P_1 cannot diffuse on a macroscopic length scale.

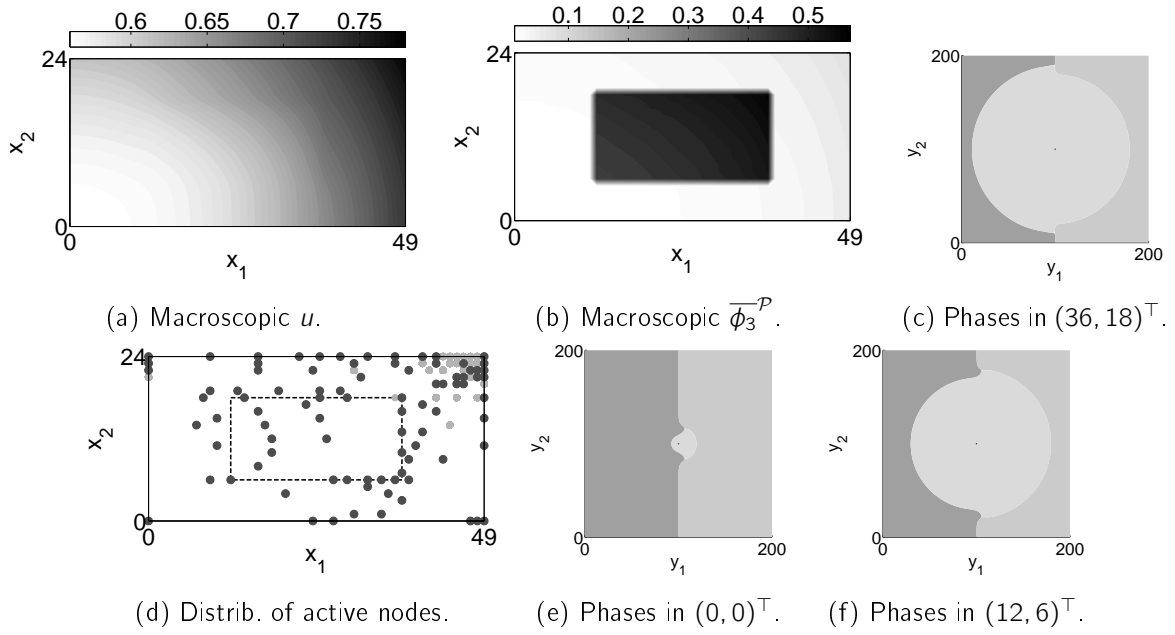


Figure 5.11: Results of test S_4 in the end of $J_{\Delta n_t}(15.5)$. Figure (d) illustrates the distribution of the adaptive strategy's active nodes on the macroscopic domain: a dark dot denotes an active node in the end of $J_{\Delta n_t}(15.5)$, and a light dot signals that a node was active but became inactive in course of the simulation. The dashed line marks the sub-domain $\Omega_{h_g}^{(2)}$.

5.4.3.4 The test S_4

Finally, Figure 5.11 presents the results of test S_4 . Test S_4 differs from S_3 only in the parameter u_0 . In S_4 the initial concentration $u_0 = 0.3$ of dissolved particles in P_1 is below the threshold $c_{u,1} = 0.5$ of the rate-function f defined in (5.5). Consequently, the solids recede in the beginning of $J_{\Delta n_t}(15.5)$, that is solid particles of P_3 dissolve in the fluid P_1 . Due to the dissolution and the transport of particles across the boundary of Ω_{h_g} the concentration u in P_1 increases. From the moment the concentration exceeds the threshold, the solid regions advance again as a result of precipitation. The edges in the concentration field and in the volume fraction field $\overline{\phi}_3^{\mathcal{P}}$ in Ω_{h_g} are not as distinct as in S_3 . This is due to the initial retreat of the solids in S_4 and the resulting larger volume fractions $\overline{\phi}_1^{\mathcal{P}}$. The larger $\overline{\phi}_1^{\mathcal{P}}$ the stronger the diffusion.

What is also depicted in Figure 5.11 is the distribution of the active macroscopic nodes of the adaptive strategy. Only the microscopic problems in active macroscopic nodes are solved. Most of them are located in the areas of Ω_{h_g} with steep slopes in the concentration field, since steep slopes yield (in general) outstanding concentration evolutions. The evolutions of the concentrations in the areas of Ω_{h_g} with moderate slopes are usually very similar. On average 85.57, that is only around 7%, of the 1,250 macroscopic nodes are active in $J_{\Delta n_t}(15.5)$.

5.5 Conclusion and outlook

The combination of, firstly, three pore-scale Allen-Cahn type equations modeling the evolution of three phase-fields that are treated as a smooth approximation to the characteristic functions of the three sub-domains of the pore-space that are occupied by three different substances – two immiscible and incompressible fluids P_1 and P_2 and a solid P_3 that is attached to the grain – in a sharp-interface model, secondly, a pore-scale Diffuse Domain Approximation (DDA) [Li *et al.*, Commun. Math. Sci. 7(1), 81-107, 2009] equation approximating with the help of the phase-fields – in their role as a smooth approximation to the characteristic functions – a sharp-interface model's evolution equation describing the concentration of dissolved particles in the fluid P_1 as well as the Rankine-Hugoniot condition on the moving sharp interface of P_1 , thirdly, the application of a homogenization technique to the pore-scale model, and finally, the adaptive solution strategy of Section 3, resulted in a numerically efficiently solvable two-scale tri-phase phase-field model for precipitation in a porous medium with three phases.

This section proved that, if the initial condition of the phase-fields represents a perfect mixture, in the sense that the sum of the phase-fields equals one and each phase-field is greater or equal to zero, then the Allen-Cahn type equations model a perfect mixture as well. A formal asymptotic analysis showed that the pore-scale phase-field model approximates in the limit, that is for the width of the phase-transition regions tending to zero, a suitable sharp-interface model. The presented numerical results of the upscaled model demonstrate the interdependence of the change of the pore structure and of the evolution of the macroscopic concentration of the dissolved particles in P_1 . In addition, they show that the smaller the volume fraction of the fluid P_1 of the pore-space the weaker the diffusion of the particles in P_1 on a macroscopic length-scale.

In order to generalize the model to a situation with $N > 3$ phases, the following parts of the model need to be adjusted. N Allen-Cahn equations are required to model the evolution of N phase-fields that smoothly approximate the N characteristic functions in a suitable sharp-interface model, the potential $W(\Phi)$ needs to have N minima, and the function $\bar{g}(\Phi)$ must interpolate the Rankine-Hugoniot conditions on the $N - 1$ parts $(\partial P_1(t) \cap \partial P_2(t)), \dots, (\partial P_1(t) \cap \partial P_N(t))$ of the moving boundary of the fluid P_1 . Whereas this generalization is straightforward, including fluid flow into the model is tricky. Since Allen-Cahn equations are not mass conservative, it is possible that if the fluids flow through the pore-space that one of them is fully absorbed by the the solid. On the contrary, Cahn-Hilliard equations ensure the conservation of mass, but it is well known that they cannot guarantee that the phase-fields stay within the bounds zero and one. However, it is fundamental to the DDA method that the phase-fields stay within these bounds.

Besides the inclusion of fluid flow into the problem, an analysis for the pore-scale as well as for the upscaled phase-field model is a major part of future research. Furthermore, future research aims at analyzing the interpolation of the Rankine-Hugoniot conditions in the diffuse triple junctions.

Acknowledgment

The results presented in this section result from joint work with I. Sorin Pop and Christian Rohde.

6 Conclusion and outlook

This dissertation dealt with three topics. Section 3 and Section 4 were devoted to the development of numerical schemes that allow for an efficient solution of two-scale models. On contrary, the aim of the research presented in Section 5 was to model and simulate a pore-scale precipitation process and a Darcy-scale diffusion process of in a fluid dissolved particles in a porous medium. This process is of great interest for e.g. prognoses of soil salinization.

The numerical results presented in the sections 3 and 4 show the efficiency of both established solution schemes. In comparison to a direct discretization, both schemes enable to accelerate a two-scale model's solution significantly and nevertheless to obtain accurate results. What is important to note is that the results presented in the sections 4 and 5 show that, as it was claimed in Section 3, the developed adaptive solution strategy is not only applicable to the sample two-scale model but also directly to other ones on condition that the variables on the different scales are continuously interdependent. What simply has to be adjusted is the metric that compares the evolution of the macroscopic fields.

Whereas the research on the two numerical schemes is in principle concluded, it is in full progress on the precipitation model. Promising future directions of research are, firstly, a theoretical analysis of the coupled pore-scale problem 5.8 on page 85, secondly, the analysis of the asymptotic behavior of the concentration u of the pore-scale problem 5.8 in the diffuse interfaces that separate oil and solid as well as in the diffuse triple junctions where all three phases are existent, thirdly, a theoretical analysis of the upscaled problem 5.15 on page 99, fourthly, the inclusion of fluid-flow into the model, fifthly, the increase of the number of the phases that occupy the pore-space, and, sixthly, the adaption of the model reduction scheme proposed in Section 4 to the upscaled problem 5.15, just to mention a few.

Acknowledgment

First of all I would like to thank Prof. Dr. Christof Eck for providing me the opportunity to work on this dissertation. Him having been my diploma thesis supervisor at the University of Bielefeld, he also became my supervisor at the University of Stuttgart. The results presented in Section 3 as well as the article [49] result from our joint work. Unfortunately, he passed away far too early in 2011.

Furthermore, I would like to thank Prof. Dr. Christian Rohde who made it possible for me to continue this work. Also, I want to thank him for his support. And I want to thank Prof. Dr. Sorin Pop for the nice and fruitful time we had on my two visits to Eindhoven. The results presented in Section 5 result from the joint work of the three of us.

Also I want to thank Jun.-Prof. Dr. Bernard Haasdonk for working with me on my second publication [50]. These results are presented in Section 4.

I would like to thank the German Research Foundation (DFG) for financial support of my project within the Cluster of Excellence in Simulation Technology (EXC 310/1) and within the International Research Training Group “Non-linearities and Upscaling in Porous Media” (NUPUS, IRTG 1398), both at the University of Stuttgart.

Moreover, I would like to thank all my colleagues at IANS, especially Ingrid Bock, Brit Steiner and Sylvia Zur for solving all the non-mathematical problems, and especially Michael Kutter and Christian Winkel for the fruitful discussions we had, that lasted many, many times until far into the night.

Last but not least, I want to thank Aylin Deveci and Arnulf Dahlmeier, as well as Josef, Brigitte, Barbara und Donata Redeker.

A promise is a promise.

References

- [1] F. Albrecht, B. Haasdonk, S. Kaulmann, and M. Ohlberger. The localized reduced basis multiscale method. In A. Handlovičová, Z. Minarechová, and D. Ševčovič, editors, *Algorithmy 2012 - Proceedings of contributed papers and posters*, volume 1, pages 393–403. Publishing House of STU, 2012.
- [2] M. Barrault, Y. Maday, N. C. Nguyen, and A. T. Patera. An 'empirical interpolation' method: application to efficient reduced-basis discretization of partial differential equations. *C. R. Acad. Sci. Paris Series I*, 339:667–672, 2004.
- [3] J. Bergh and J. Löfström. *Interpolation Spaces, an Introduction*. Springer, Berlin, 1976.
- [4] O. Besov, V. P. Il'yin, and S. M. Nikol'skii. *Integral Transformations of Functions and Embedding Theorems*, volume 2. V. H. Winston and Sons, Washington D.C., 1979.
- [5] S. Boyaval. Reduced-basis approach for homogenization beyond the periodic setting. *Multiscale Model. Simul.*, 7(1):466–494, 2008.
- [6] F. Boyer and C. Lapuerta. Study Of A Three Component Cahn-Hilliard Flow Model. *ESAIM: M2AN*, 40(4):653–687, 2006.
- [7] F. Boyer, C. Lapuerta, S. Minjeaud, B. Piar, and M. Quintard. Cahn-Hilliard/Navier-Stokes Model for the Simulation of Three-Phase Flow. *Transp Porous Med*, 82:463–483, 2010.
- [8] L. Bronsard and F. Reitich. On Three-Phase Boundary Motion and the Singular Limit of a Vector-Valued Ginzburg-Landau Equation. *Arch. Rational Mech. Anal.*, 124:355–379, 1993.
- [9] G. Caginalp. An analysis of a phase field model of a free boundary. *Arch. Ration. Mech. Anal.*, 92:205–245, 1986.
- [10] G. Caginalp. Stefan and Hele-Shaw type models as asymptotic limits of the phase-field equations. *Phys. Rev. A*, 39(11):5887–5896, 1989.
- [11] G. Caginalp and X. Chen. Convergence of the phase field model to its sharp interface limits. *Euro. Jnl of Applied Mathematics*, 9:417–445, 1998.
- [12] G. Caginalp and P. Fife. Dynamics of Layered Interfaces Arising from Phase Boundaries. *SIAM J. Appl. Math.*, 48(3):506–518, 1988.
- [13] G. Caginalp and W. Xie. An analysis of phase-field alloys and transition layers. *Arch. Ration. Mech. Anal.*, 142:293–329, 1998.
- [14] S. Chaturantabut and D. C. Sorensen. Discrete empirical interpolation for nonlinear model reduction. *SIAM J. Sci. Comput.*, 32(5):2737–2764, 2010.
- [15] D. Cioranescu and P. Donato. *An Introduction to Homogenization*. Oxford University Press, New York, 1999.
- [16] S. Davis. *Theory of Solidification*. Cambridge University Press, Cambridge, 2001.
- [17] M. Dihlmann, M. Drohmann, and B. Haasdonk. Model reduction of parametrized evolution problems using the reduced basis method with adaptive time-partitioning. In *Proc. of ADMOS 2011*, 2011.
- [18] M. Drohmann, B. Haasdonk, and M. Ohlberger. Reduced basis approximation for nonlinear parametrized evolution equations based on empirical operator interpolation. *SIAM J. Sci. Comput.*, 34(2)(2):A937–A969, 2012.
- [19] W. E and B. Engquist. The heterogeneous multiscale method. *Commun. Math. Sci.*, 1:87–123, 2003.
- [20] C. Eck. Analysis of a two-scale phase field model for liquid-solid phase transitions with equiaxed dendritic microstructure. *Multiscale Model. Simul.*, 3:28–49, 2004.
- [21] C. Eck. Homogenization of a phase field model for binary mixtures. *Multiscale Model. Simul.*, 3:1–27, 2004.
- [22] C. Eck. A two-scale phase field model for liquid-solid phase transitions of binary mixtures with dendritic microstructure. Professorial dissertation, Naturwissenschaftliche

Fakultäten der Universität Erlangen-Nürnberg, July 2004.

- [23] C. Eck. Error estimates for a finite element discretization of a two-scale phase field model. *Multiscale Model. Sim.*, 6:1–26, 2007.
- [24] C. Eck and H. Emmerich. A two-scale phase field model for liquid phase epitaxy. *Math. Meth. Appl. Sci.*, 32:12–40, 2009.
- [25] J. L. Eftang, D. Knezevic, and A. Patera. An hp certified reduced basis method for parametrized parabolic partial differential equations. *Math. Comp. Model Dyn.*, 17:4:395–422, 2011.
- [26] J.L. Eftang, A.T. Patera, and E.M. Rønquist. An hp certified reduced basis method for parametrized elliptic partial differential equations. *SIAM J. Sci Comp*, 32(6):3170–3200, 2010.
- [27] J.L. Eftang and B. Stamm. Parameter multi-domain "hp" empirical interpolation. *Internat. J. Numer. Methods Engrg.*, 90(4):412–428, 2012.
- [28] L.C. Evans. *Partial Differential Equations*. Graduate studies in mathematics. American Mathematical Society, 2010.
- [29] B. Haasdonk. Convergence rates of the POD-Greedy method. *M2AN Math. Model. Numer. Anal.*, 47:859–873, 2013.
- [30] B. Haasdonk, M. Dihlmann, and M. Ohlberger. A training set and multiple basis generation approach for parametrized model reduction based on adaptive grids in parameter space. *Math. Comp. Model Dyn.*, 17:423–442, 2012.
- [31] B. Haasdonk and M. Ohlberger. Reduced basis method for finite volume approximations of parametrized linear evolution equations. *Math. Model. Numer. Anal.*, 42(2):277–302, 2008.
- [32] U. Hornung, editor. *Homogenization and Porous Media*. Springer, New York, 1997.
- [33] T. Y. Hou and X.-H. Wu. A multiscale finite element method for elliptic problems in composite materials and porous media. *J. Comput. Phys.*, 134:169–189, 1997.
- [34] V. V. Jikov, S. M. Kozlov, and O. A. Oleinik. *Homogenization of Differential Operators and Integral Functionals*. Springer, Berlin, 1994.
- [35] I. T. Jolliffe. *Principal Component Analysis*. Springer-Verlag, 2002.
- [36] A. Karma. Phase-field formulation for quantitative modeling of alloy solidification. *Physical Review Letters*, 87, 2001.
- [37] A. Karma and W.-J. Rappel. Quantitative phase-field modeling of dendritic growth in two and three dimensions. *Physical Review E*, 57(4):4323–4349, 1998.
- [38] S. Kaulmann, M. Ohlberger, and B. Haasdonk. A new local reduced basis discontinuous galerkin approach for heterogeneous multiscale problems. *Comptes Rendus Mathematique*, 349(23-24):1233–1238, 2011.
- [39] P. Knabner, C.J. Van Duijn, and S. Hengst. An analysis of crystal dissolution fronts in flows through porous media. Part 1: Compatible boundary conditions. *Adv. Water Resour.*, 18(3):171–185, 1995.
- [40] D. J. Knezevic and A. T. Patera. A certified reduced basis method for the fokker–planck equation of dilute polymeric fluids: Fene dumbbells in extensional flow. *SIAM J. Sci. Comput.*, 32(2):793–817, 2010.
- [41] R. Kobayashi. Modeling and numerical simulations of dendritic crystal growth. *Physica D: Nonlinear Phenomena*, 63:410–423, 1993.
- [42] J. Kockelkoren, H. Levine, and W.-J. Rappel. Computational approach for modeling intra- and extracellular dynamics. *Phys. Rev. E*, 68:037702, 2003.
- [43] W. Kurz and D. J. Fisher. *Fundamentals of Solidification*. TransTech Publications, Switzerland, 1998.
- [44] X. Li, J. Lowengrub, A. Rätz, and A. Voigt. Solving PDEs In Complex Geometries: A Diffuse Domain Approach. *Commun. Math. Sci.*, 7:81–107, 2009.
- [45] N. C. Nguyen. A multiscale reduced-basis method for parametrized elliptic par-

- tial differential equations with multiple scales. *Journal of Computational Physics*, 227(23):9807–9822, 2008.
- [46] M. Patra and M. Karttunen. Stencils with isotropic discretization error for differential operators. *Wiley InterScience*, pages 936–953, 2005.
- [47] B. Peherstorfer, D. Butnaru, K. Willcox, and H. Bungartz. Localized Discrete Empirical Interpolation Method. Technical Report TR-13-1, Aerospace Computational Design Lab, Dept. of Aeronautics & Astronautics, MIT, June 2013.
- [48] J. C. Ramirez, C. Beckermann, A. Karma, and H. J. Diepers. Phase-field modeling of binary alloy solidification with coupled heat and solute diffusion. *Physical Review E*, 69, 2004.
- [49] M. Redeker and C. Eck. A fast and accurate adaptive solution strategy for two-scale models with continuous inter-scale dependencies. *J. Comp. Phys.*, 240:268–283, 2013.
- [50] M. Redeker and B. Haasdonk. A POD-EIM reduced two-scale model for crystal growth. Preprint, <http://www.simtech.uni-stuttgart.de/publikationen/prints.php?ID=785>, accepted for publication on 4 June 2014 by *Adv. Comput. Math.*
- [51] M. Renardy and R.C. Rogers. *An Introduction to Partial Differential Equations*. Springer, 2004.
- [52] T. Roubicek. *Nonlinear partial differential equations with applications*. Springer, 2005.
- [53] L. Tan and N. Zabaras. Multiscale modeling of alloy solidification using a database approach. *J. Comput. Phys.*, 227:728–754, 2007.
- [54] T.L. van Noorden and C. Eck. Phase field approximation of a kinetic moving-boundary problem modelling dissolution and precipitation. *Interfaces and Free Boundaries*, 13:29–55, 2011.
- [55] T.L. van Noorden and I.S. Pop. A Stefan problem modelling crystal dissolution and precipitation. *IMA J. Appl. Math.*, 73(2):393–411, 2008.
- [56] H. H. Viet and C. Schwab. High-dimensional finite elements for elliptic problems with multiple scales. *Multiscale Model. Simul.*, 3:168–194, 2005.
- [57] A. Visintin. *Models of Phase Transitions*. Birkhäuser, Boston, 1996.
- [58] S. Volkwein. *Lecture Notes: Proper Orthogonal Decomposition: Theory and Reduced-Order Modelling*. University of Constance, 2013.
- [59] B. Wieland. *Reduced Basis Methods for Partial Differential Equations with Stochastic Influences*. PhD Thesis, Universität Ulm, April 2013.